UNIVERSITÉ DU QUÉBEC À RIMOUSKI

Modélisation, optimisation et surveillance en temps réel du procédé de soudage par résistance par points appliqué aux plaques minces pour l'industrie automobile

Mémoire présenté à l'Université du Québec à Rimouski comme exigence partielle du programme de maîtrise en ingénierie en vue de l'obtention du grade de maître ès sciences appliquées (M.Sc.A.)

Par

© Blériot Vincent Feujofack Kemda

Avril 2020

Composition du jury :

Jean-François Méthot, président du jury, UQAR
Noureddine Barka, directeur de recherche, UQAR
Mohammad Jahazi, codirecteur de recherche, ÉTS
Sasan Sattarpanah Karganroudi, examinateur externe, ITMI

Dépôt initial le 23 Decembre 2019 **Dépôt final le 22 Avril 2020**

UNIVERSITÉ DU QUÉBEC À RIMOUSKI

Service de la bibliothèque

Avertissement

Dédicace

Je dédie ce travail à mes parents : M. KEMDA Mathias & Mme KEMDA Marie

Remerciements

Je tiens à exprimer mes profonds remerciements à toutes les personnes qui, de près ou de loin, m'ont apporté leur soutien, notamment moral, matériel et financier lors de l'exécution de ce travail de recherche. Sans oublier ceux qui m'ont prodigué des conseils, des orientations, des idées et des instructions. Je pense tout particulièrement à :

- Pr. Noureddine Barka, mon superviseur, pour les directives, les connaissances et les conseils qu'il m'a donnés et qu'il m'a transmis afin de produire ce travail de recherche.
- Pr. Mohammad Jahazi, mon co-superviseur pour les directives et les conseils qu'il m'a donnés tout au long de cette période de recherche.
- Tous les professeurs du département de mathématique, d'informatique et de génie de l'UQAR, pour les connaissances et les conseils qu'ils m'ont donnés.
- M. Denis Osmani, le Directeur Général de l'entreprise AMH Canada Ltée, pour nous avoir soutenu tout au long de ce projet en mettent à notre disposition des soudeuses par résistance par points pour nos essais.
- Tous mes camarades de classe et les membres de mon groupe de recherche, pour leur collaboration constante.
- Mes frères et sœurs Joel, Franklin, Olivia, Ange, Manuela et Horlane pour leur soutien.
- Tous ceux qui n'ont pas été mentionnés ci-dessus et qui ont contribué de près ou de loin à la réalisation de ce projet.

Avant-propos

Ce mémoire a été rédigé dans le cadre des travaux de recherche au cycle de maîtrise en ingénierie à l'UQAR. Le projet étudié a été subdivisé en quatre parties et est présenté ici sous forme de mémoire par articles. De prime abord, une brève introduction, donnant l'état de l'art du procédé de soudage par résistance par points (SRP), le problème et les objectifs visés est présentée. S'en suit le corps du travail, subdivisé en quatre parties représentant des articles scientifiques. Une étude exploratoire du procédé de SRP est faite dans la première partie, cette étude met en évidence l'effet des paramètres de procédé sur la qualité des soudures obtenues. Le deuxième chapitre présente un travail d'optimisation des paramètres de procédé du SRP. Dans la troisième partie, une modélisation du procédé de SRP est faite. Le modèle electo-thermo-mecanico-métallurgique développé a permis de mieux comprendre l'évolution de la micro-structure dans le métal lors du soudage et de mettre en évidence l'effet d'un traitement thermique post-soudage sur la micro-structure. La quatrième partie quant à elle présente un travail d'implémentation d'une technique permettant de prédire, en temps réel, la qualité des joints de soudure à l'aide de la signature du signal de résistance dynamique. Après le corps du travail, une conclusion est présentée. Cette dernière met en exergue les différents résultats obtenus et les différentes observations faites lors de la réalisation de ce projet. Des pistes de recherche à considérer sont également présentées afin de garantir la poursuite de ce projet. Les travaux de recherche ont été menés en deux étapes ; d'une part, les opérations de soudage, effectuées dans les locaux de l'entreprise AMH Canada Ltée (unité de production de Rimouski) et d'autre part, les essais et analyses, menés au sein du département de mathématique, d'informatique et de génie de l'UQAR.

Résumé

La présente étude a été menée dans le but d'optimiser et de d'améliorer le procédé de soudage par résistance par points (SRP). En effet, le SRP est un procédé intensivement utilisé dans l'assemblage de tôles minces pour l'industrie automobile. Bien qu'il soit très ancien, le SRP présente toujours des challenges techniques ; tels que : les distorsions thermiques, les temps et énergies de production élevés ou encore l'apparition de fissures après le soudage. L'automatisation du procédé de SRP a vu le jour il y a quelques années. Cette automatisation a notamment permis d'accroître la productivité et la répétabilité du procédé de SRP. Toutefois, l'automatisation a fait naître un nouveau problème ; celui de l'intégrité des soudures effectuées. En effet, en raison d'aléas divers, les conditions de soudage ne sont jamais les mêmes et les soudures qui en résultent sont parfois de mauvaise qualité. Les problèmes cités ci-haut indiquent clairement un besoin d'amélioration du procédé de SRP, d'où la genèse de ce travail intitulé : « Modélisation, optimisation et surveillance en temps réel du procédé de soudage par résistance par points appliqué aux plaques minces pour l'industrie automobile ».

Afin de mener à bien ce travail, l'objectif principal a été subdivisé en quatre objectifs spécifiques, à savoir l'exploration, la modélisation, l'optimisation et la surveillance du procédé de SRP. Un premier travail exploratoire a été effectué afin de déterminer l'effet des paramètres de procédé sur la géométrie et la résistance mécanique des joints soudés. Ce travail a permis d'établir une corrélation entre la dureté, la géométrie et la qualité de la soudure. Ensuite, un travail d'optimisation des paramètres de procédé a été effectué. Afin de parvenir a une optimisation effective et efficiente des paramètres de procédé, un algorithme génétique a été développé et implémenté. Cette optimisation a été basée sur les résultats obtenus dans l'étude exploratoire. Afin de résoudre le problème de fragilité des soudures, un modèle électro-thermo-mécano-métallurgique a été développé. Ce modèle a permis de mieux comprendre et aussi de prédire l'évolution de la micro-structure dans le métal lors du soudage. À l'aide de ce modèle, des pistes de solution ont été proposées pour la résolution du problème de fragilité des soudures. Pour finir, une technique a été

développée et implémentée afin de prédire la qualité des soudures en temps réel au cours du processus de soudage à l'aide de la signature de résistance dynamique.

Les résultats de cette études montrent que le courant de soudage est le paramètre le plus influent dans le SRP et contribue de l'ordre de 70 % à la résistance mécanique des soudures. L'optimisation des paramètres de procédé a entraîné une diminution moyenne du courant de soudage, de la force de pressage des électrodes et du temps de soudage de 10,58 %, 13,59 % et 32,61% respectivement. Le modèle prédictif développé a permis d'établir que l'application du traitement thermique post-soudage (TTPS) mène à augmentation des fractions de bainite et de ferrite et une diminution de la fraction de martensite dans le nœud de soudure ; ce qui signifie une réduction de fragilité au sein des soudures. Une prédiction de la qualité des joints soudés a été rendue possible grâce à l'exploitation des signaux de résistance dynamique. L'application de tous ces résultats mèneront à une augmentation de résistance mécanique des noeuds de soudure et à une réduction des coûts de production.

Mots clés : Soudage par résistance par points ; Dureté ; Diamètre des noeuds ; Analyse de variance ; Surfaces de réponse ; Résistance à la traction-cisaillement ; Optimisation ; Algorithme génétique ; AISI 1010 ; Modélisation ; Traitement thermique post-soudage ; Transformation de phase ; Cinétique ; Conditions de soudage ; Signature de résistance dynamique ; Fuseau de passage ; Intégrité de la soudure

Abstract

This study was conducted to optimize and make the resistance spot welding (RSW) process more viable. Indeed, the RSW is a process intensively used in the assembly of thin sheet metal for the automotive industry. Although it is very old, the RSW still presents technical challenges : thermal distortions, high production times and energy or the appearance of cracks after welding. The automation of the RSW process began a few years ago. This automation has notably increased the productivity and repeatability of the RSW process. However, automation has created a new problem : the integrity of the welds performed. Indeed, due to various hazards, welding conditions are never the same and the resulting welds are sometimes of poor quality. The problems mentioned above clearly indicate a need for improvement in the RSW process, hence the genesis of this work entitled : "Real-time modelling, optimization and monitoring of the resistance spot welding process applied to thin plates for the automotive industry".

In order to carry out this work, the main objective has been subdivided into four specific objectives, namely exploration, modelling, optimisation and monitoring of the RSW process. A first exploratory study was carried out to determine the effect of process parameters on the geometry and mechanical strength of welded joints. This work made it possible to establish a correlation between hardness, geometry and weld quality. Then, work was carried out to optimize the process parameters. This optimization was based on the results obtained in the exploratory study. In order to achieve an effective and efficient optimization of process parameters, a genetic algorithm has been developed and implemented. In order to solve the problem of weld brittleness, an electro-thermo-mechanical-mechanical-metallurgical model was developed. This model has made it possible to better understand and also to predict the evolution of the microstructure in the metal during welding. Using this model, possible solutions were proposed to solve the problem of weld brittleness. Finally, a technique was developed and implemented to predict the quality of the welds in real time during the welding process using the dynamic resistance signature.

The results of this study show that welding current is the most influential parameter in the RSW and contributes up to 70 % to the mechanical strength of the

welds. Optimization of process parameters resulted in an average decrease in welding current, electrode pressing force and welding time of 10.58 %, 13.59 % and 32.61% respectively. The predictive model developed established that the application of post-welding heat treatment (PWHT) leads to an increase in bainite and ferrite fractions and a decrease in martensite fraction in the weld node ; which means a reduction in brittleness within the welds. A prediction of the quality of welded joints was made possible by using dynamic resistance signals. The application of these results will lead to an increase in the viability of the RSW and a reduction in production costs.

Keywords : Resistance spot welding ; Hardness ; Nugget diameter ; Analysis of variance ; Response surface ; Tensile-shear strength ; Optimization ; Genetic algorithm ; AISI 1010 ; Modeling ; Post weld heat treatment ; Phase transformation ; Kinetics ; Welding conditions ; Dynamic resistance signature ; Validation passageway ; Weld integrity

Table des matières

Liste des figures

Liste des tableaux

Liste des abréviations

AISI	American Iron and Steel Institute
ANOVA	Analysis of variance
ASTM	American Society for Testing and Materials
BM	Base metal
CCT	Continuous cooling transformation
DAQ	Data acquisition
DP	Dual-phase
FZ	Fuzion zone
GA	Genetic algorithm
HAZ	Heat affected zone
HSLA	High strength low alloy
HSS	High-strength steel
HV	Hardness in Vickers
JMAK	Johnson-Mehl-Avrami-Kolmogorov
MOGA	Multi-objective genetic algorithm
NI	National Instruments
NSGA	Non-dominated sorting genetic algorithm
PAES	Pareto-archived evolution strategy
PHC	Post heating current
PHT	Post heating time
PWHT	Post weld-heat treatment
RSW	Resistance spot welding

SPEA Strength Pareto evolutionary algorithm

SRP Soudage par résistance par points

TRIP Transformation induced plasticity

TTPS Traitement thermique post-soudage

UQAR Université du Québec à Rimouski

ZAT Zone affectée thermiquement

Introduction générale

Mise en contexte

Le soudage par résistance par points (SRP) est un procédé intensivement utilisé dans l'industrie automobile. Toute carrosserie d'automobile compte en moyenne 4000 points de soudures. Ce procédé ne nécessite pas d'équipements spéciaux et est facilement automatisable, ce qui permet d'atteindre de grandes vitesses de production. Cela explique l'énorme intérêt que les manufacturiers ont envers ce procédé. Inventé en 1877 par Elihu Thomson, breveté par le même en 1886, le soudage par résistance ne se développa réellement qu'à partir de 1925 [1]. Le SRP est un procédé d'assemblage sans métal d'apport et est dit autogène. La fusion du métal, localisée entre les tôles à assembler, est obtenue par effet Joule (courant électrique de quelques kilo ampères) [2]. Ce procédé s'applique généralement à des assemblages de deux ou plusieurs tôles de faibles épaisseurs que l'on cherche à joindre par un point de soudure. Les tôles mises en contact sont soumises à un effort de pression par l'intermédiaire de deux électrodes reliées aux bornes du secondaire d'un transformateur ; elles sont ainsi traversées par un courant alternatif de forte intensité sous une faible tension. Depuis son invention, le procédé de SRP a suivi des évolutions fulgurantes. Toutefois, jusqu'à nos jours, le SRP est toujours le sujet de multiples recherches scientifiques car plusieurs aspects de ce vieux procédé restent encore à améliorer.

Problème

Bien que le SRP soit vieux de plus d'un siècle, son application présente toujours des challenges encore non résolus. Parmi ces challenges, on peut citer l'effet de shunt [3], les distorsions thermiques, les déformations, la formation des pores. Afin de surmonter ces problèmes, les paramètres de soudage sont souvent surestimés, c'est-à-dire que l'énergie de soudage d'entrée est généralement beaucoup plus élevée que celle nécessaire, ce qui entraîne généralement une augmentation des coûts de

production. Parmi les aciers laminés à chaud, l'ASTM A36 est le plus répandu. Il est utilisé dans les parties internes des structures de voitures [4]. L'acier galvanisé, dû à sa bonne résistance à la corrosion, est de plus en plus utilisé dans l'industrie automobile au détriment des aciers laminés à froid afin d'améliorer la résistance à la corrosion des véhicules [5]. Cependant, le soudage en transparence d'aciers recouverts de zinc pose de réels défis techniques et nécessite une grande précision dans la détermination des paramètres de soudage [6]. En effet, l'acier galvanisé nécessite plus de courant, de force et de temps de soudage qu'un acier ordinaire car les couches de zinc créent un effet de shunt [5]. Cette augmentation d'amplitudes des paramètres de procédé entraîne une détérioration prématurée des électrodes, qui sont les principaux consommables du procédé de soudage par résistance par points [7]. De plus, l'application incorrecte de la chaleur conduit très souvent à une mauvaise adhérence entre les plaques. L'excès de courant de soudage cause des éruptions, des fissures et des expulsions pendant le soudage, ce qui conduit à une réduction de résistance mécanique des soudures [8]. L'optimisation des paramètres de procédé semble être une bonne approche pour résoudre les problèmes cités plus haut. En effet, beaucoup de travaux d'optimisation des paramètres de procédé dans le SRP ont été effectués et ont permis de résoudre ces problèmes jusqu'à une certaine ampleur. D'après la littérature, on peut observer que de nombreux chercheurs se sont concentrés sur une optimisation uni-objective des paramètres de procédé du SRP. Généralement, soit la géométrie de la soudure ou la résistance mécanique est prise en compte comme fonction objective dans l'optimisation, mais jamais les deux à la fois, d'où l'expression «uni-objective». Ce type d'approche permet d'optimiser seulement partiellement le procédé car en optimisant une seule sortie, on peut perdre en performance par rapport aux autres variables de sortie. Étant donné que l'industrie est en constante évolution vers l'optimisation de l'ensemble du procédé, il devient essentiel de se concentrer sur plusieurs variables de sortie à la fois. De plus, le SRP étant un procédé dans lequel l'acier est chauffé et refroidi en un laps de temps, le nœud de soudure résultant est généralement entièrement martensitique, en particulier dans le cas des aciers ultrarésistant, à savoir, les aciers biphasés (dual-phase steel), des aciers à transformation induite par plasticité (TRIP steel) et des aciers au

bore (boron steel). Cependant, la martensite qui est une structure cristalline très dure constitue un point faible dans la résistance mécanique des soudures, car elle est extrêmement fragile. Ainsi, une étude profonde et une compréhension des transformations de phases au cours du SRP est nécessaire. Aujourd'hui, ce processus a été entièrement automatisé afin d'augmenter la vitesse de production et la répétabilité. Cette automatisation a porté ses fruits à travers l'augmentation des vitesses de production. Cependant, avec l'automatisation, l'intégrité des soudures effectuées est très souvent remise en question. En effet, en raison des hasards divers, les conditions de soudage ne sont jamais les mêmes et les soudures qui en résultent sont parfois de mauvaise qualité. Ces soudures de mauvaises qualités à leur tour sont rarement décelées ; car tout se fait par des robots incapables d'apprécier la qualité et l'intégrité des soudures. Afin de valider les soudures effectuées, l'industrie fait recours à une inspection humaine post-soudage, une opération fastidieuse qui ralentit l'ensemble du procédé et augmente les coûts de production. Le problème peut ainsi être récapitulé en plusieurs sections comme suit :

- Le temps et le coût de productions élevés pour le SRP
- La formation d'une microstructure défavorable lors du soudage des aciers ultrarésistants
- La non détection des soudures non-intègres due à la robotisation du procédé de SRP

Hypothèses de résolution

Dans le but de résoudre les problèmes rencontrés dans le soudage par résistance par points à nos jours, des hypothèses ont été émises. Ces hypothèses sont les suivantes :

- Une optimisation multi-objective des paramètres de procédés permettra de réduire les temps et coûts de production de manière efficace
- L'application d'un traitement thermique post-soudage permet de contrôler la microstructure dans le nœud de soudure et donc de réduire le taux de martensite dans ce dernier

- Le signal de résistance dynamique d'une soudure permet de déterminer, en temps réel, la qualité des soudures et les conditions physiques dans lesquelles ces dernières sont effectuées.

Objectifs de recherche

L'objectif principal de ce travail est d'améliorer la qualité et la résistance mécanique des soudures par résistance par points tout en réduisant les coûts de production. Cet objectif principal se subdivise en plusieurs objectifs spécifiques, à savoir :

- Déterminer l'effet des paramètres de procédé sur la géométrie et la résistance mécanique des soudures **(exploration)**
- Optimiser les paramètres de procédé **(optimisation)**
- Développer des outils pour la prédiction des cycles de chauffage/refroidissement permettant d'appliquer avec succès le soudage par résistance par points aux aciers ultra-résistants **(modélisation)**
- Développer une technique permettant de prédire la qualité des soudures et les conditions physiques de soudage en temps réel lors du SRP **(surveillance)**

Contribution originale

Ayant pour objectif principal l'optimisation et l'amélioration du SRP de plaques minces pour l'industrie automobile, plusieurs développements ont été faits dans le cadre de ce projet. Ces développements peuvent être présentés en quatre thématiques suivant les objectifs spécifiques comme suit :

1. Détermination de l'effet des paramètres de procédé sur la géométrie et la résistance mécanique des soudures :

   Les effets des paramètres de procédé sur la dureté et le diamètre des joints soudés ont été évalués. Des modèles de surface de réponse combinant la dureté dans la zone de fusion et le diamètre des nœuds ont été tracés en fonction des paramètres de soudage. La méthodologie utilisée ici a permis de mieux comprendre les effets des paramètres de procédé sur la qualité globale des nœuds soudés.

2. Optimisation multi-objective des paramètres de procédé lors du soudage par résistance par points :

   L'approche proposée ici visait l'optimisation des paramètres de procédé dans le SRP avec prise en compte simultanée de plusieurs critères de qualité, à savoir la dureté et la résistance à la traction/ cisaillement, qui sont des propriétés mécaniques ; et le diamètre des nœuds, qui est une variable de sortie géométrique. D'autre part, l'algorithme d'optimisation utilisé (NSGA-II) offre une approche permettant de surmonter le problème de la stagnation à l'optimum local lors du processus d'optimisation et permet de résoudre des problèmes convexes, encore appelés problèmes avec optimums indifférents.

3. Modélisation de la cinétique de phases et application du traitement thermique post-soudage lors du soudage par résistance par points :

   Afin d'obtenir des soudures résistantes, ductiles et durables, il est crucial de comprendre la transformation métallurgique de l'acier pendant le processus de soudage. La résistance mécanique des soudures dépend directement de leur microstructure. Ainsi, en déterminant la microstructure d'une soudure, il est possible de prévoir la résistance mécanique de celle-ci. Il est donc judicieux d'ajuster les paramètres de soudage afin d'obtenir une microstructure souhaitée et donc une résistance souhaitée. Dans ce projet, il est démontré par des outils de simulation que l'application du TTPS permet de réduire la teneur en martensite et d'augmenter la diversité de phase dans les joints soudés par résistance. Comme il est bien connu que la martensite est responsable de la fragilité des soudures, l'application du TTPS implique de ce fait une augmentation de la ductilité des soudures et de leur durée de vie globale en fatigue.

4. Prédiction de la qualité des soudures à travers la signature de résistance dynamique :

   Dans cette partie, une méthode qui permet de mettre en évidence des soudures peu intègres pendant le processus de soudage a été développée. L'approche mise en œuvre est basée sur la signature de résistance dynamique des joints soudés, qui est déterminée à partir de l'acquisition en temps réel des signaux de courant et de tension de soudage. Une série d'expériences de soudage a été réalisée sur de l'acier

doux ASTM A36. À partir d'analyses statistiques et de l'exploitation des résultats expérimentaux, un fuseau de passage de validation de résistance dynamique a été déterminé et permet de contrôler la qualité des soudures. Outre le contrôle de la qualité des joints soudés, l'approche mise en œuvre permet également de déterminer les conditions physiques de soudage des soudures effectuées, telles que l'état de surface des tôles, la présence de limaille de fer sur les tôles, les soudures se chevauchant, le soudage d'une seule tôle, la présence d'un gap entre les tôles à souder et l'absence de tôles pendant le soudage.

Méthodes de recherche

Ce projet de recherche s'intitule « Modélisation, optimisation et surveillance en temps réel du procédé de soudage par résistance par points appliqué aux plaques minces pour l'industrie automobile » et a été réalisé au sein du département de mathématique, informatique et génie de l'UQAR, en partenariat avec la compagnie locale AMH Canada Ltée. Le but ultime était d'améliorer le procédé de SRP dans son ensemble. Pour y parvenir, une approche évolutive a été adoptée.

En premier lieu, un travail exploratoire a été effectué. Purement expérimental, ce travail a permis de mettre en évidence l'effet des paramètres de procédé sur les propriétés geométrico-mécaniques des soudures par résistance. Afin de parvenir à cela, des essais préliminaires furent effectués sur des plaques d'acier doux A36 et d'acier galvanisé A653. Ces essais ont permis de déterminer les fenêtres de soudabilité des métaux utilisés, ensuite une planification d'expériences de soudage a été faite en variant les principaux paramètres du procédé de soudage par résistance par point ; à savoir, le courant de soudage le force de pressage des électrodes et le temps de soudage. S'en est suivi le soudage des éprouvettes, suivant les plans factoriels complets préétablis. Des essais de dureté par micro-indentations ont alors permis d'établir les profils de dureté le long des nœuds de soudure tandis que des analyses micrographiques ont permis de déterminer les compositions microstructurales des joints soudés. Des essais de traction/cisaillement ont permis d'émettre un jugement final sur la résistance mécanique des soudures. Des analyses de variance ont ensuite été effectuées afin de

quantifier et qualifier l'effet de chaque paramètre de procédé sur les propriétés geométrico-mécaniques des joints soudés.

Après avoir déterminé l'effet de chaque paramètre de procédé, une optimisation de ces derniers a été effectuée. Cette optimisation constitue ainsi la deuxième partie de ce mémoire. Les résultats obtenus dans la section précédente ont permis d'effectuer une optimisation multi-objective simultanée des paramètres de procédé. Pour y parvenir, un algorithme multi-objectif par tri de non-dominance a été développé et implémenté. Cet algorithme, écrit en langage C et exécuté sous MATLAB a permis de parvenir à une optimisation effective et efficiente des paramètres de procédé du SRP. Les paramètres optimisés ont ensuite été évalués par des essais de traction-cisaillement des éprouvettes soudées.

Dans la troisième partie de ce mémoire, une approche numérique a été adoptée afin de mieux comprendre l'évolution des phases microstructurales lors du SRP. Dans cette partie, une simulation par éléments finis de l'ensemble du procédé de SRP est effectuée. Un modèle numérique a été développé sous une plateforme hybride Comsol-Matlab. Ce modèle est constitué de quatre principaux modules. Les trois premiers modules, à savoir, les modules électrique, thermique et mécanique, ont été développés sous Comsol, tandis que le module métallurgique a été développé sous Matlab. Des essais expérimentaux ont été effectués afin de confirmer la validité du modèle développé.

Après l'exploration, l'optimisation et la modélisation du procédé de SRP, un travail d'inspection automatisée des soudures a été effectué. Dans cette dernière partie, une technique permettant de prédire en temps réel la qualité des soudures a été développée et implémentée. Le travail effectué dans cette section a été basé sur l'instrumentation, à savoir l'acquisition, le conditionnement, le traitement et l'exploitation des signaux de résistance dynamique des joints soudés. L'acquisition s'est faite à travers des capteurs de courant et de tension, et d'une carte NI MyDAQ. Le conditionnement quant à lui a été effectué à l'aide d'un programme développé sous LabVIEW, tandis que le traitement et l'exploitation des signaux ont été effectuées grâce à un programme développé sous MATLAB.

Structure du mémoire

Ce manuscrit est rédigé sous la forme d'un mémoire et comporte plusieurs parties définies de façon succinctes suivant les objectifs spécifiques afin de faciliter la lecture et la compréhension. Tout commence par une introduction générale dans laquelle l'état de l'art est établi, le problème est posé, des hypothèses de résolution sont proposés, les objectifs sont présentés et le plan de travail, annoncé. Le corps de ce mémoire quant à lui est composé de quatre articles scientifiques. Ces articles répondent aux questions de recherche et sont donc par ce fait liés aux objectifs spécifiques.

- Le premier chapitre fait l'objet d'un article d'exploration expérimentale du procédé de soudage par résistance par points. Dans cet article, les effets des paramètres de procédé sur la géométrie et la résistance mécanique des soudures sont déterminés.
- Le deuxième chapitre quant à lui présente un article qui a pour objectif principal l'optimisation multi-objective des paramètres de procédé lors du soudage par résistance par points.
- Le troisième chapitre présente un article sur la modélisation électro-thermo-mécano-métallurgique du SRP. Le but dans cet article est de déterminer l'effet d'un traitement thermique post-soudage sur la microstructure des soudure par résistance par points.
- Le quatrième et dernier chapitre est un article de conférence. Dans ce chapitre, une technique permettant de prédire en temps réel la qualité des soudures par résistance par points à travers la signature de résistance dynamique est implémentée.

Après le corps du travail, une conclusion générale est présentée. Cette conclusion laisse transparaître les principaux résultats obtenus et les principales remarques effectuées tout au long de ce projet. S'en suit une ouverture de sujet à travers des propositions d'éventuels travaux futurs qui permettront inéluctablement de placer le procédé de soudage par résistance par points en tête de liste, en ce qui concerne les moyens d'assemblage de tôles minces dans l'industrie automobile.

Chapitre 1

Effect of Process Parameters on Hardness and Nugget Geometry of A36 Mild Steel and Hot Dipped Galvanized Steel Resistance Spot Welds

International Journal of Advanced Manufacturing and Technology - Springer

B. V. Feujofack Kemda[ψ,*], **N. Barka**[ψ], **M. Jahazi**[χ] **and D. Osmani**[ζ]

Sommaire

Submitted on August 03rd 2019, Accepted on November 12th 2019

https ://doi.org/10.1007/s00170-019-04707-w

**Corresponding author - E-mail address :*bleriotvincent.feujofackkemda@uqar.ca (B. V. Feujofack Kemda)
[ψ] *University of Quebec in Rimouski, Québec G56 3A1, Canada.*
[χ] *Ecole de Technologie Superieure, Montréal, Québec H3C 1K3, Canada.*
[ζ] *AMH Canada Ltd, Rimouski, Québec G5L 1Z2, Canada.*

Avant-propos

Auteurs et affiliations

Blériot Vincent Feujofack Kemda : Étudiant en maîtrise en ingénierie, Département de mathématiques, d'informatique et de génie, Université du Québec à Rimouski, Rimouski, Québec G56 3A1, Canada.

Noureddine Barka : Professeur, Département de mathématiques, d'informatique et de génie, Université du Québec à Rimouski, Rimouski, Québec G56 3A1, Canada.

Mohammad Jahazi : Département de génie mécanique, École de technologie supérieure, Montréal, Québec H3C 1K3, Canada.

Denis Osmani : AMH Canada Ltée, Rimouski, Québec G5L 1Z2, Canada

Titre en Français

Effet des paramètres de procédé sur la dureté et la géométrie des noeuds de soudure par résistance d'acier doux A36 et d'acier galvanisé à chaud.

État de l'article

Accepté et en cours de publication dans le journal : « International Journal of Advanced Manufacturing and Technology ».

Contribution au mémoire

Cet article constitue la première partie de ce mémoire. Il s'agit d'une étude exploratoire du procédé de soudage par résistance par points. Les effets des paramètres de soudage sur la dureté et le diamètre des noeuds de soudures ont été évalués. Des modèles de surface de réponse combinant la dureté dans la zone de fusion et le diamètre des noeuds ont été tracés en fonction des paramètres de soudage. La méthodologie utilisée ici a permis de mieux comprendre les effets des paramètres du procédé sur la qualité globale des joints soudés.

Résumé en Français

Le soudage par résistance par points (SRP), un procédé très utilisé pour l'assemblage de tôles minces dans l'industrie automobile, ferroviaire et aéronautique, a toujours présenté des défis techniques et économiques. Les déformations thermiques et les difficultés causées par la présence d'un revêtement anticorrosion sur les aciers galvanisés sont parmi les principaux problèmes. Une évaluation des effets des paramètres de soudage sur la qualité globale des joints soudés est ainsi d'une grande importance pour résoudre ces problèmes. Deux nuances d'aciers ont été utilisées dans cette étude : l'acier doux A36 et l'acier galvanisé par immersion à chaud A653. Les expériences de soudage ont été effectuées en configuration de transparence, nuance pour nuance, tout en suivant des plans factoriels complets de trois facteurs à deux niveaux. Des analyses micrographiques ont révélé la microstructure des soudures tandis que des essais de dureté par micro-indentations ont permis d'établir le profil de dureté le long des noeuds de soudure. Des analyses de variance (ANOVA) ont été effectuées afin d'évaluer l'effet de chaque paramètre sur la dureté et le diamètre des noeuds. Des modèles de surface de réponse combinant la dureté dans la zone de fusion et le diamètre des noeuds ont été tracés en fonction des paramètres de soudage. Ces surfaces de réponse ont montré que le courant est le paramètre prédominant et devrait être maximisé afin d'obtenir des soudures solides tandis que la force et le temps devraient être minimisés pour l'acier doux A36 et maximisés pour l'acier galvanisé.

Abstract

Resistance spot welding (RSW), a process intensively used for thin metal sheets assembly in automotive, railway and aeronautical industries, has always presented technical and economic challenges. Thermal distortions and difficulties caused by the presence of anti-corrosive coating on galvanized steels are among the major issues. An evaluation of effects of welding parameters on overall nugget quality will be of great importance in solving these issues. Two grades of steel were used in this study, A36 mild steel and A653 hot dipped galvanized steel. Welding experiments were done in overlap configuration, grade for grade, while following complete factorial plans of three factors at two levels. Micrographic analyses revealed welds microstructure while micro-indentation hardness tests enabled to establish the hardness profile along weld nuggets. Analyses of variance (ANOVA) were done in order to evaluate the effect of each parameter on nugget hardness and diameter. Response surface models combining hardness in the fusion zone and nugget diameter were plotted as function of welding parameters. These response surfaces showed that current is the predominant parameter and should be maximized in order to achieve strong welds while force and time should be minimized for A36 mild steel and maximized for galvanized steel.

Keywords : Resistance spot welding ; Hardness ; Nugget diameter ; ANOVA ; Response surface

1.1 Introduction

Resistance spot welding (RSW) is widely used in the assembly of metal plates. Welding is obtained by a combination of heat, pressure and time [9]. This process offers very high productivity and is easily automated, hence its wide application in the automotive industry [10–12]. Moreover, it is an autogenous process ; its practice thus promotes sustainable development. However, problems are frequently encountered during the RSW of thin sheets, namely, shunt effect [3], thermal distortions, pore formation in welds and early interfacial rupture of welds in the case of coated sheets (galvanized steel). In order to overcome these problems, welding parameters have very

often been overestimated, that is the input welding energy is generally much higher than required, which has generally led to an increase in production costs. Among hot-rolled steels, ASTM A36 is the most widespread. It is used in sectors such as bridges, boats, car and machine structures, railways, and construction [4]. Galvanized steel, due to its good corrosion resistance, is increasingly used in the automotive industry to the detriment of cold-rolled steels in order to improve the corrosion resistance and overall lifespan of vehicles [5]. However, the transparent welding of zinc-coated steels poses real technical challenges and requires high precision in determining welding parameters [6]. Indeed, galvanized steel requires more current, force and welding time than ordinary steels because zinc layers create a shunt effect [5]. This increase in welding parameters leads to the early deterioration of the electrodes, which are the main consumables during resistance welding [7]. In addition, improper application of heat very often leads to poor bonding between the plates. Excess welding current causes blowouts, cracking and expulsions during welding, which leads to a reduction in the mechanical strength of the welds [8]. In view of the difficulties mentioned above, a careful and adequate determination of welding parameters is therefore essential.

1.1.1 Principle of resistance spot welding

In RSW, two or more elements are welded together through the heat generated by the electrical resistance of the elements [13]. Indeed, the electrodes exert a contact force on the parts to be welded while they are traversed by a high electric current (Figure 1.1). By resisting the passage of current, the parts will heat up and the welding will take place once the melting point of the metals has been reached. According to the modified heat balanced theory, it is essential to take into account the heat generated in each part of a weld in order to have a very accurate estimation of the thermal effect. The following gives the heat needed for heating a body :

$$q = m \times C_p \times \Delta T \tag{1.1}$$

Where q is the heat in Joules, Cp is the specific heat of the material, m its mass and ΔT is the change in temperature. Zhang and Senkara [14] proposed a heat calculation

model in which the weld nugget is split in six main parts (Figure 1.2). Each part can be simplified as a small cylinder. Thus, the amount of heat required to create a weld can then be calculated as follows :

$$\because Q = q_1 + q_2 + q_3 + q_4 + q_5 + q_6 \tag{1.2}$$

For instance, the heat required in the upper heat affected zone (part 2) reads :

$$\begin{aligned} q_2 &= m_2 \times C_{P1} \times \Delta T_2 \\ m_2 &= \tfrac{\pi}{4} \cdot d_{e1}^2 \cdot h_2 \cdot \rho_1 \end{aligned} \tag{1.3}$$

Where d_{e1} is assumed to be the overall nugget diameter in the upper sheet, ρ_1 being the density of the upper sheet and h_2 being the thickness of upper heat affected zone (HAZ).

Thus,

$$q_2 = \frac{\pi}{4} d_{e1}^2 h_2 \rho_1 C_{P1} \Delta T_2 \tag{1.4}$$

For the melted nugget (parts 3 and 4), one has to take into account the latent heat, thus for upper nugget for instance (part 3), the required heat include the heat needed before, during and after the melting of steel. It is calculated as follows :

$$q_3 = \frac{\pi}{4} d_{e1}^2 \rho_1 C_{P1} h_3 (T_{melt} - T_{amb}) + \rho_1 L_{f1} + \rho_1 C_{P1} (T_{\max} - T_{melt}) \tag{1.5}$$

Where L_{f1} is the latent heat of the upper sheet. By analogy, Equation 1.4 can be applied to parts 1, 2, 5 and 6 while Equation 1.5 holds for parts 3 and 4. Thus, the required heat for the overall nugget reads :

$$\begin{aligned} \therefore Q = \frac{\pi}{4} d_{e1}^2 \rho_1 C_{P1} h_1 \Delta T_1 + \frac{\pi}{4} d_{e1}^2 \rho_1 C_{P1} h_2 \Delta T_2 + \frac{\pi}{4} d_{e1}^2 \rho_1 C_{P1} h_3 (T_{\text{melt}} - T_{amb}) + \rho_1 L_{f1} \\ + \rho_1 C_{P1} (T_{\max} - T_{\text{melt}}) + \frac{\pi}{4} d_{e2}^2 \rho_2 C_{P2} h_4 (T_{\text{melt}} - T_{amb}) + \rho_2 L_{f2} + \rho_2 C_{P2} (T_{\max} - T_{\text{melt}}) \\ + \frac{\pi}{4} d_{e2}^2 \rho_2 C_{P2} h_5 \Delta T_5 + \frac{\pi}{4} d_{e2}^2 \rho_2 C_{P2} h_6 \Delta T_6 \end{aligned} \tag{1.6}$$

Governed by the Joule's law, the general expression of the heat generated in an electrical circuit is :

$$Q = R \cdot I^2 \cdot t \tag{1.7}$$

Where Q is the amount of heat, I is the electrical current, R is the electrical resistance of the circuit and t is the time during which the current passes through the circuit. The RSW consists of four fundamental steps, namely squeeze cycle, weld cycle, hold cycle and release cycle [15]. The overall welding time includes these four steps.

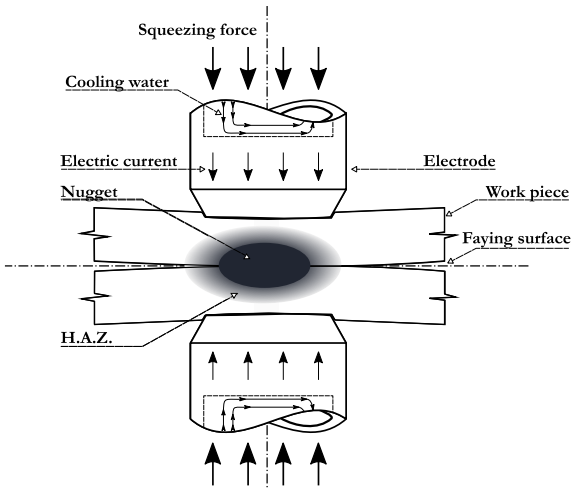

Figure 1.1 – Schematic representation of RSW process

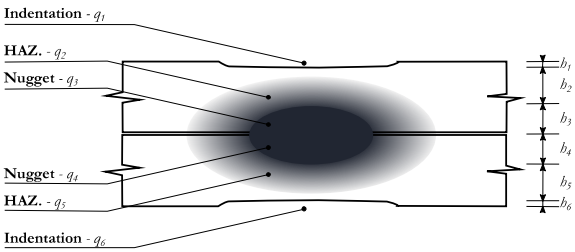

Figure 1.2 – Geometric discretisation of a weld

The main welding parameters are current, welding time and electrodes pressing force, which create contact between the parts to be welded. A combination of Equations 1.6 and 1.7 thus provides a rough estimate of the current and time required to create a

weld. These parameters depend on the nature and thickness of the parts to be assembled.

1.1.2 Effect of process parameters

During RSW, the greater the indentation left by the electrode, the more resistant the weld is. In order to obtain indentations of up to 25% of the plate thickness, Kumar and Vijayajumar [15] optimised the resistance welding parameters of the AISI 304L using the Taguchi method. They then evaluated the effect of the optimised parameters on the fusion nugget diameter and on the mechanical strength of the welded sheets. In their work, the analysis of variance showed that the most influential parameters are welding time and the interaction between current and welding time. Pashazadeh et al. [16] conducted a study on effect of machine parameters during the RSW. They began by designing a complete factorial experiment of three factors at two levels, including current, pressing force and welding time. An analysis of variance (ANOVA) was then carried out to determine the influence of these parameters on the height and diameter of the welding nugget. From this analysis, it emerged that current is the most influential parameter, for both nugget diameter and nugget height, welding time was found to influence nugget diameter but no clear correlation was observed between this factor and nugget height. The pressing force had no obvious influence on the dimensions of nugget. At this level it can be observed that current and time have an influence on nugget geometry. Suresh [17] studied a systematic approach of determining optimum process parameters in order to maximise tensile strength (shear). The tests were conducted on 1 mm thick corrugated mild steel specimens. In his study, the parameters studied were current, time and electrode diameter. An L27 orthogonal matrix was used. The analysis of variance showed that current is the most influential parameter (63.70%), followed by welding time (28.70%) for the tensile strength of welds. Shah et Dhaval [18] have conducted a work on the development and evaluation of neural network-based systems for the search of optimal RSW parameters and for the assessment of weld quality. The analysis of variance showed the contribution of the factors to the weld strength, in particular 49.81 % for current, 37.94 % for thickness and 2.61% for welding time, with

an overall error of 9.61 %. Singh et al. [19] presented an approach to determine the effect of process parameters (current, pressure and time) on the tensile strength of AISI 316L austenitic stainless steel welds using the Taguchi method. The experiments were conducted through an L9 Taguchi orthogonal matrix. Analyses showed that welding current is the most important factor influencing the mechanical strength of welds. Pandey et al. [20] optimised the RSW process parameters using Taguchi's method. The material used in the study was mild steel (AISI 1008/ ASTM A366), for 0.9 mm thick sheets. The quality criterion in their optimisation was mechanical strength. The analysis of variance performed shows a contribution of current, force and time of 61%, 28.7% and 4% respectively. At this point, only nugget geometry and tensile strength have been studied, no previous work have been carried on finding the effect of welding parameters on hardness through ANOVA method. Knowing that tensile strength of steels are related to their hardness [21], studying the effect of welding parameters on weld hardness is a fast, repeatable and reliable mean to foresee the effects of these parameters on weld strength. From literature review carried out [15–18, 20], it was found that many researchers focused on the effect of welding parameters on one quality at a time, namely weld geometry or mechanical strength. This kind of approach can lead to a partial understanding of the process because a welding parameter can have a positive effect on one output variable while having a negative effect on another output variable. As the industry is constantly evolving towards the mastering of the entire process, it becomes essential to focus on several output variables at once. In this work, the effects of welding parameters on nugget hardness and nugget diameter were evaluated. The specimens were welded in accordance with pre-established complete factorial plans. Micrographic analysis and hardness tests enabled to determine the hardness and nugget diameter of welds. Response surface models combining hardness in the fusion zone and nugget diameter were plotted as function of welding parameters. The approach developed in this work can be used to find effects of process parameters on overall nugget quality in RSW of mild steel and galvanized steel sheets for the automotive industry.

1.2 Materials and methods

1.2.1 Materials

ASTM A36 mild steel and ASTM A653 hot dipped galvanized steel, with thicknesses of 0.80 mm and 1.80 mm each, were used in this work. These steels have good tensile strength and ductility. A36 steel consists of ferrite and perlite, and is extensively used in the automotive industry. This steel has high weldability and does not need special heat treatments as preheating techniques as found by Chang and Teng [22] who carried experimental investigations on the residual stresses of the butt-welded joints of A36 mild steel. Galvanized steel, on the other hand, is gaining more and more importance in the automotive industry because of its good corrosion resistance. This resistance is achieved through zinc coating that acts as barrier to inhibit the oxidation of carbon steel [23]. The galvanized steel grade used in this work was coated with a zinc layer at a coating density of $282.6 g/m^2$. The chemical composition of A36 and galvanized steels used are given in Table 1.1. Their mechanical characteristics are given in Table 1.2.

Table 1.1 – ASTM A36 steel and ASTM A653 hot dipped galvanized steel, chemical composition in %*.

Material	C	Mn	P	S	Cu	Si	Ni	Cr	Mo	Cb	V	Ti	Fe
A36	0.27	1.03	0.04	0.05	0.20	0.280	< 0.1	< 0.08	< 0.1	-	-	-	
A653	0.15	0.60	0.03	0.035	0.25	-	0.2	0.15	0.06	0.008	0.008	0.025	

**Typical composition*

Table 1.2 – Mechanical properties of A36 steel and A653 hot dipped galvanized steel

Material	Yield strength (MPa)	Ultimate tensile strength (MPa)	Elongation (%)	Hardness (HV)
A36	441.3	503.3	30	120
A653	277.5	363.8	37.5	121

**Typical composition*

1.2.2 Resistance spot welder

Different types of welding machines are used for different combinations of steel sheets in resistance spot welding experiments [24]. The welding machine used is the

COMUSpot fusion 900 MAX, developed by AMH Canada Ltd. It is an intelligent manual welder due to its ability of providing and proposing welding parameters according to grade and thickness of steels to be welded. It is equipped with two liquid-cooled welding guns. It generates clamping forces up to 6300 N (1.386lbf), a current of 14 kA and allows precise adjustment of welding parameters.

1.2.3 Experimental considerations

In order to carry out the welding operation, an experimental set-up was designed. The latter allows the plates to be firmly fixed, which improves the repeatability of the process (Figure 1.3). The steel plates were welded in overlap configuration, based on the minimum and maximum values of the process parameters (from weldability tests), four full factorial plans of three factors at two level each were established for specimen welding (Table 1.3 and Table 1.4). Full factorial plans were used in this work in order to find the effects of all parameters as well as effects of all interactions for a deep understanding of the process.

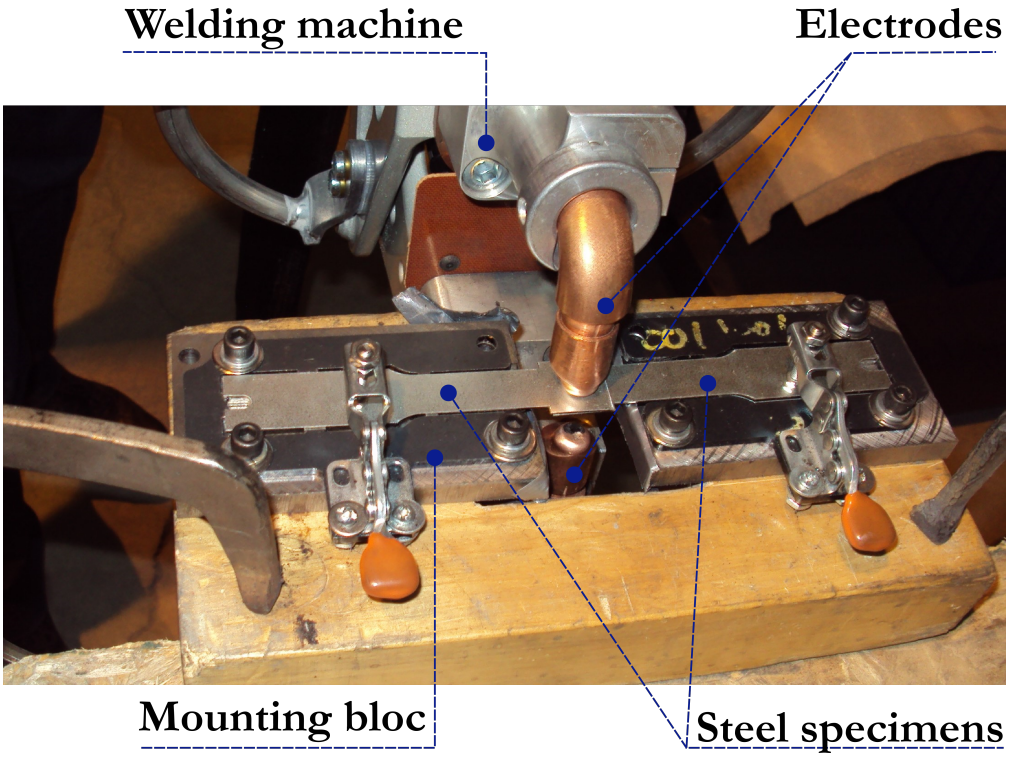

Figure 1.3 – Welding experimental setup

Table 1.3 – Design of experiment for A36 mild steel

Thickness - 0.80 mm				**Thickness - 1.80 mm**			
#	$I(A)$	$F(daN)$	$t(ms)$	#	$I(A)$	$F(daN)$	$t(ms)$
1	5000	100	150	1	7000	250	250
2	5000	100	300	2	7000	250	400
3	5000	200	150	3	7000	350	250
4	5000	200	300	4	7000	350	400
5	7000	100	150	5	8500	250	250
6	7000	100	300	6	8500	250	400
7	7000	200	150	7	8500	350	250
8	7000	200	300	8	8500	350	400

Table 1.4 – Design of experiment for A653 galvanized steel

Thickness - 0.80 mm				**Thickness - 1.80 mm**			
#	$I(A)$	$F(daN)$	$t(ms)$	#	$I(A)$	$F(daN)$	$t(ms)$
1	7500	200	300	1	8000	350	350
2	7500	200	500	2	8000	350	650
3	7500	400	300	3	8000	450	350
4	7500	400	500	4	8000	450	650
5	9500	200	300	5	10000	350	350
6	9500	200	500	6	10000	350	650
7	9500	400	300	7	10000	450	350
8	9500	400	500	8	10000	450	650

1.2.3.1 Welds' nugget diameters

The nugget diameter is until now the best way to determine the mode of weld failure. Sawhill et al. [25] showed that for button pull-out failure mode, the tensile shear strength of high strength steel spot welds was highly correlated to nugget diameter. Mei et al. [5] compared laser and spot welding of galvanized steel, they concluded that for spot welding, weld bearing capacity mainly depended on nugget diameter and depth. Pouranvari et al. [26] investigated on the effects of nugget diameter on failure mode and strength of resistance spot welds. They found that nugget diameter was narrowly linked

to failure mode and on that basis, they developed a numerical model for the prediction of mechanical failure of resistance spot welds. Thus, it was important to take this parameter into account in our study. The diameters of the welding nodes were measured for all performed welds. A quantitative estimate of the diameter of a weld can be made in three ways : (i) from the indentation left by the electrode [27] (Figure 1.4.a), (ii) from a cross-section of the weld [27] (Figure 1.4.b) or (iii) from the weld hardness profile (Figure 1.5). In order to maintain consistency in the measurements and to obtain the most accurate estimate, method (iii) was used to determine the diameters of the welding nodes.

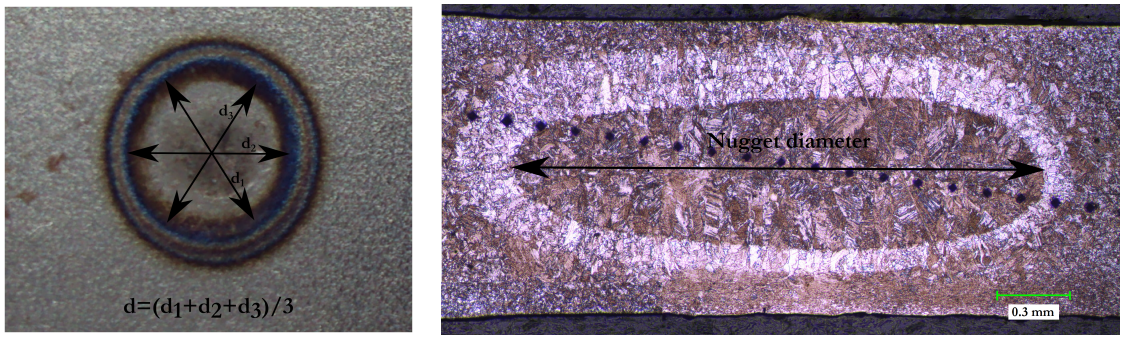

(a) Electrode footprint on the plates

(b) Cross-section of the weld nugget

Figure 1.4 – Weld macroscopy

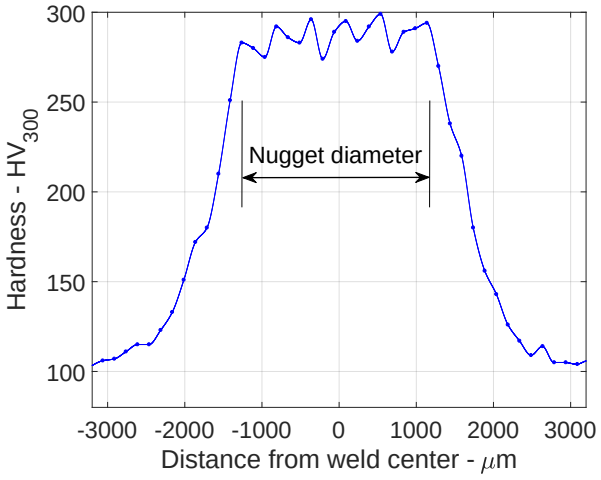

Figure 1.5 – Estimation of the weld nugget diameter with the hardness profile

1.2.3.2 Micro-indentation hardness tests and micrography

In order to carry out micrographic analyses, the specimens were cut in the transverse plane of the welds, then mounted and polished according to best practice. A micro-indentation hardness measurement was then made for all welds according to ASTM E384-17 [28] and in "Z" pattern along the cross-section of the welds (Figure 1.6). The measurements were made on a CLEMEX machine. The microstructure of the welds was detected through chemical etching with Nital (Nitric acid + ethanol), dosed at 5%, according to ASTM E407-07 [29]. Micrographic images were taken using a CANON Optihot-100 optical microscope and analysed with CLEMEX Vision software.

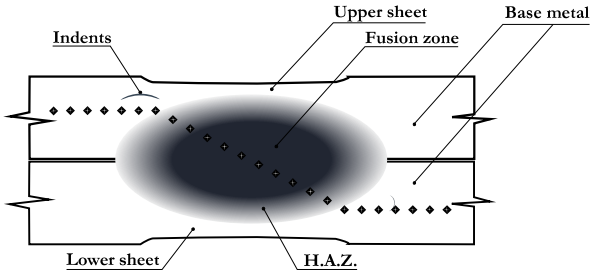

Figure 1.6 – Micro-hardness indentation pattern

1.3 Results and discussions

1.3.1 Weld nuggets appearance (Macrostructures)

Mild steel and galvanized steel plates were assembled using the resistance spot welding machine. Figure 1.4 shows overall macroscopic view of a weld. An external view of the weld is given in Figure 1.4.a, while Figure 1.4.b represents a cross-section of the weld nugget. The upper and lower electrodes were remarkably well aligned during welding operations, allowing a good symmetrical distribution of heat in the weld nuggets. We can observe the absence of defects such as cracks in Figure 1.7. However, for A36 steel, in the high thickness (1.80 mm), carbonisation of the surface layer of the plates can be observed (Figure 1.7.a), with the increase in welding current, molten particles are ejected around the welding node (Figure 1.7.b). Galvanized steel welds have a higher electrode impact, indentations are deeper and the zinc layer at the

electrodes definitely evaporates during welding. Among other things, we can see the accumulation of molten zinc around the welding nodes (Figure 1.7.c).

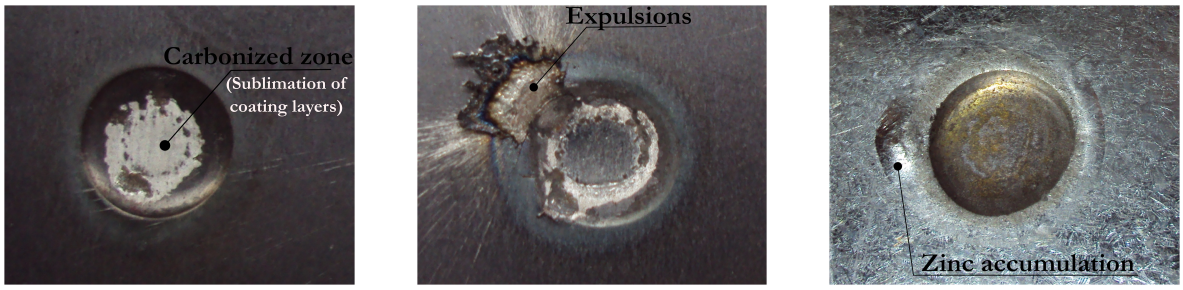

(a) Carbonisation of the coating **(b)** Expulsions **(c)** Accumulation of molten zinc

Figure 1.7 – Miscellaneous defects encountered

1.3.2 Welds microstructure

A weld nugget consists of three main parts, namely the base metal (BM), the HAZ and the fusion zone (FZ). These areas are easily identifiable on a nugget cross-section, which has been polished and etched. Typical microscopy analyses of A36 and galvanized steels weld nuggets are shown in Figures 1.8 and 1.9 respectively. For galvanized steel welds, pores are found in the melting zone, this is attributed to the expansion of sublimated zinc during welding. Figure 1.10 shows the microstructure gradient in the heat-affected zone of A36 steel. It should be noted that very often, the HAZ has a higher heterogeneity than the fusion zone [30]. This can be seen on the hardness profile of a weld. This heterogeneity is attributed to the fact that the HAZ receives a large quantity of heat and is subjected to slow cooling, on one side of the HAZ is the molten metal, very hot, and on the other side is the base metal, having a very low temperature. Zone A (Figure 1.10.a) is the closest to the base metal, generally called sub-critical HAZ, there is ferrite and some pearlite. Zone B (Figure 1.10.b), which is an intermediate zone (inter-critical HAZ), is composed of lath martensite while in zone C (super-critical HAZ) is mainly composed of lath martensite and upper bainite (Figure 1.10.c). The presence of upper bainite is attributed to relatively larger welding time (300 ms) and is in agreement with the findings of Feujofack et al. [31] who showed by simulation tool that increasing welding time lead to the reduction of martensite an increase of bainite in the nugget. Figure 1.11 shows the microstructural gradient of the HAZ for galvanized steel

welds. It can be seen that the HAZ in this case is less heterogeneous. Thus, in zones A and B (Figure 1.11.a and 1.11.b), there is a presence of martensite, ferrite and fine perlite, while zone C (Figure 1.11.c) consists of martensite and upper bainite.

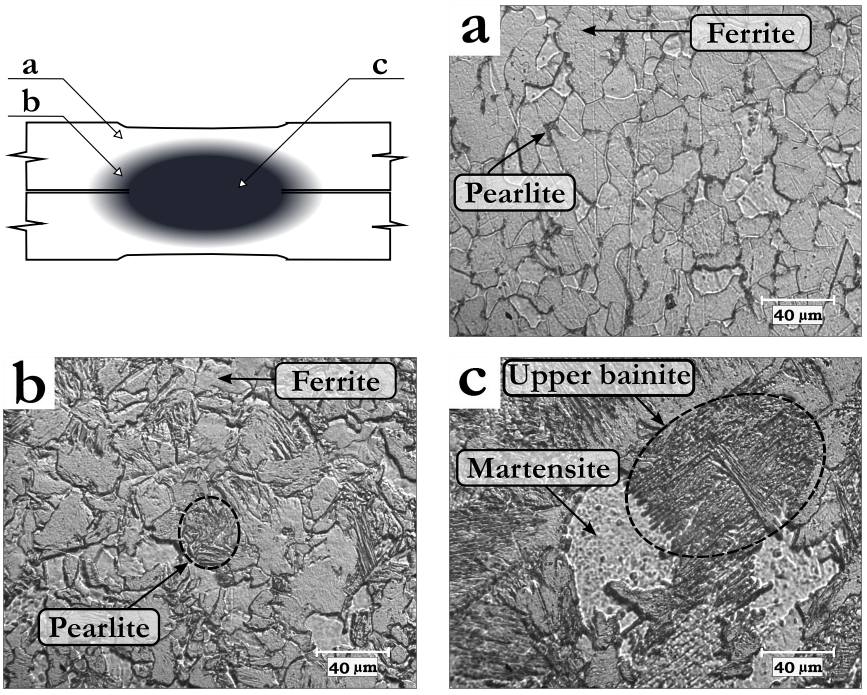

Figure 1.8 – Typical microstructure of A36 steel welds, (a) base metal, (b) HAZ, and (c) fusion zone. (×500)

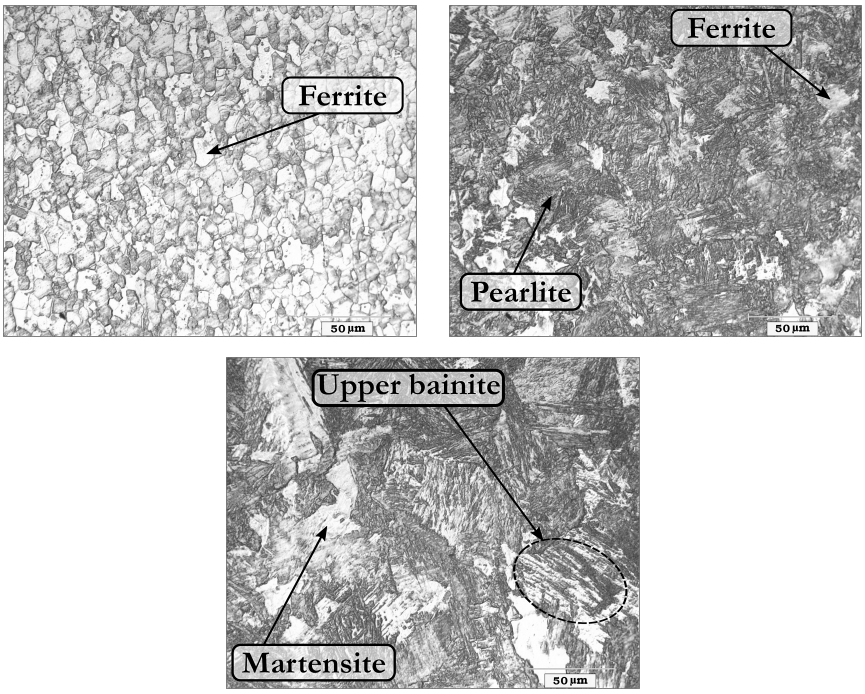

Figure 1.9 – Typical microstructure of galvanized steel welds, (a) base metal, (b) HAZ, and (c) fusion zone. (×500)

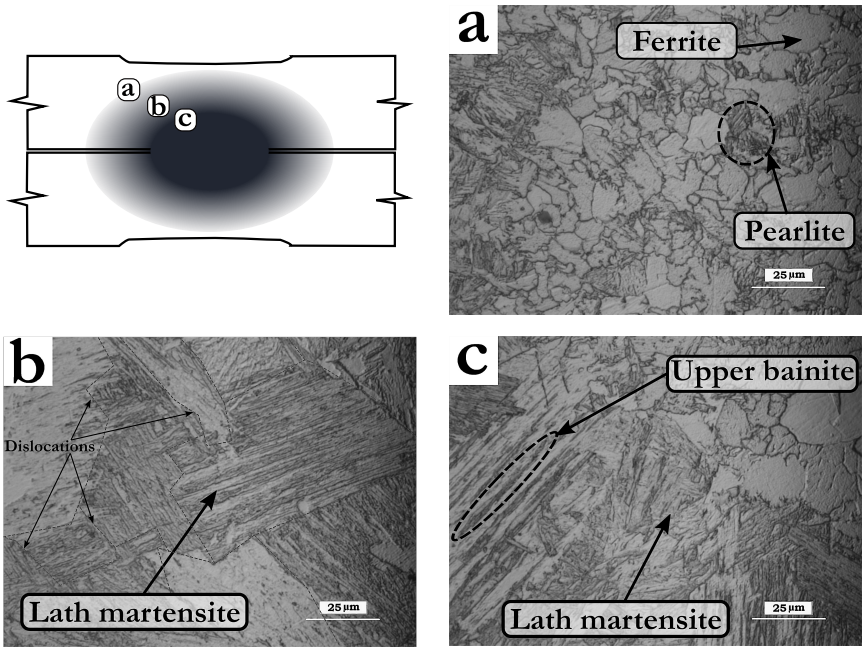

Figure 1.10 – Microstructural evolution in the HAZ of A36 steel welds, (a) close to the base metal (Sub-critical HAZ), (b) centre of the HAZ (Inter-critical HAZ), and (c) close to the fusion zone (Super-critical HAZ). (×1000)

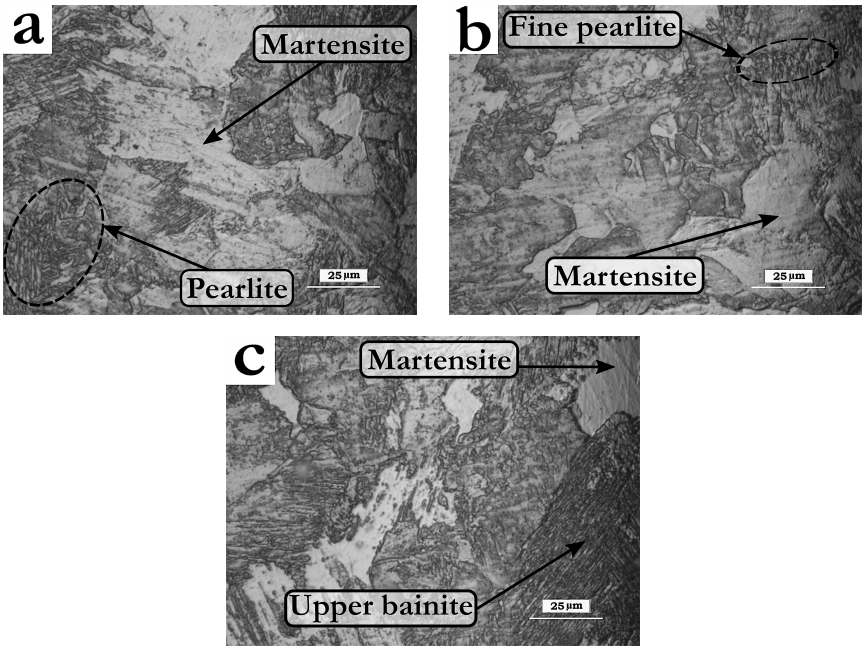

Figure 1.11 – Microstructural evolution in the HAZ of galvanized steel welds, (a) close to the base metal (Sub-critical HAZ), (b) centre of the HAZ (Inter-critical HAZ), and (c) close to the fusion zone (Super-critical HAZ). (×1000)

1.3.3 Welds hardness

Following the hardness tests, convincing results have been obtained and will be presented in graphic-digital form. An analysis of the hardness profile of well nuggets will be presented, followed by an analysis of the variance of hardness in the fusion zone.

1.3.3.1 Analysis of hardness profile

A36 and galvanized steel welds were found to have similar hardness profiles. For steel A36, the hardness in the base metal is about $110HV_{300}$. There is an increase in hardness in the HAZ with a gradient of about $15.55 \times 10^{-2} HV_{300}/\mu m$. In the melting zone, the hardness value stabilises. Galvanized steel has a hardness of $108HV_{300}$ in the base metal, in the HAZ, the hardness increases with a gradient of $12.50 \times 10^{-2} HV_{300}/\mu m$. A graphical comparison was made to highlight the effect of process parameters on the hardness profiles. This comparison was made only on A36 steel plates with a thickness of 0.8 mm. In Figure 1.12.a, the effect of welding current on the hardness profile is highlighted. It can be observed at first sight that an increase in current leads to a larger weld width. However, this increase in current has an opposite

effect on the hardness in the melting zone. Figure 1.12.b shows the effect of the electrodes pressing force on the hardness profile of welds. It is clear that an increase in pressing force leads to an increase of hardness in the metal over the entire welded area. Figure 1.12.c shows the effect of welding time on the hardness profile of welds ; it can be observed that increasing welding time has a positive effect on hardness but creates instabilities in the weld through the formation of a larger and more critical HAZ. That wide HAZ is characterized by relatively low local hardness, hence the appearance of the two low points on Figure 1.12.c.

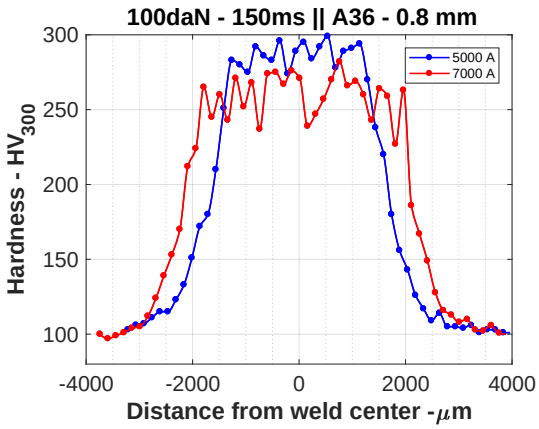

(a) Effect of current

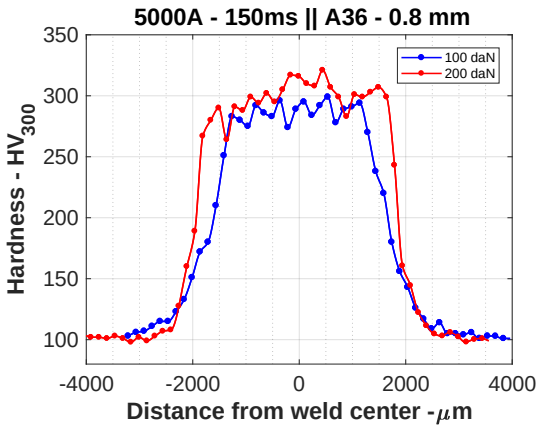

(b) Effect of pressing force

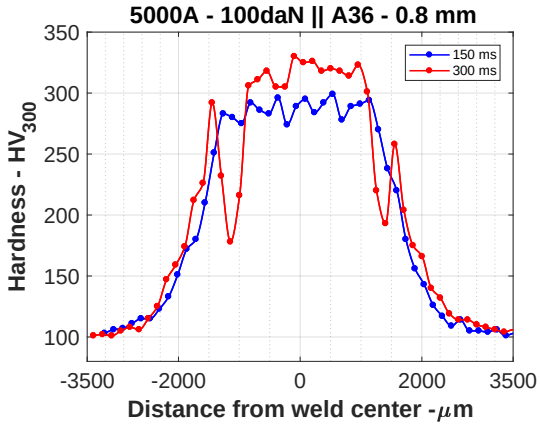

(c) Effect of welding time

Figure 1.12 – Effects of welding parameters on the weld hardness profiles

1.3.3.2 Analysis of variance of weld hardness

In order to obtain a quantitative estimate of the effect of process parameters on weld hardness, analysis of variances was performed using Minitab 17. Hardness

prediction models have also been designed using the same tool. The analysis of variance for hardness was done for A36 steel welds. The summaries of the analysis are presented in Table 1.5 and Table 1.6 . The effects of process parameters are presented in Figures 1.13.a and 1.13.b.

For thin sheets (0.8 mm), it can be seen that there is an interaction between the current and force on one hand and between current and time on the other hand. The linear regression equation that led to this hardness modelling as a function of welding parameters is as follows :

$$HV_{300} = 286.25 - 0.011625I + 0.0900F + 0.4367t + 63 \cdot 10^{-6} I \cdot F - 22 \cdot 10^{-6} I \cdot t - 0.001233F \cdot t \tag{1.8}$$

Where, HV_{300} is the hardness, I the current, F the electrodes pressing force, and t, the welding time.

For thick plates, the pressing force is the most influential parameter and has a positive effect on hardness, followed by the current, which in turn has a negative effect on hardness. Welding time remains the least influential parameter. The regression equation of the established predictive model is as follows :

$$HV_{300} = 1221 - 0.1909I - 1.669F + 443 \cdot 10^{-6} I \cdot F + 153 \cdot 10^{-6} I \cdot t - 3905 \cdot 10^{-6} F \cdot t \tag{1.9}$$

Galvanized steel has a special feature about electrical resistance. Indeed, zinc coating layers have a low resistance compared to the coated metal, this leads to heat losses during welding and results in lower quality of welds. An analysis was carried out to evaluate the influence of welding parameters on the hardness obtained. The summaries of this analysis are presented in Table 1.7 and Table 1.8. For small thickness sheets, current is the most influential factor with a negative effect, followed by welding time, which has a positive effect on hardness. The pressing force has a negligible effect. The hardness model regression equation is as follows :

$$HV_{300} = 167.3 - 2.830F + 2.726t + 333 \cdot 10^{-6} I \cdot F - 304 \cdot 10^{-6} I \cdot t \tag{1.10}$$

For thick plates, the welding time is the most influential parameter, followed by the current and pressing force. The regression equation is as follows :

$$HV_{300} = 352 - 0.0114I - 0.800F + 0.340t + 85 \cdot 10^{-6} I \cdot F - 32 \cdot 10^{-6} I \cdot t \qquad (1.11)$$

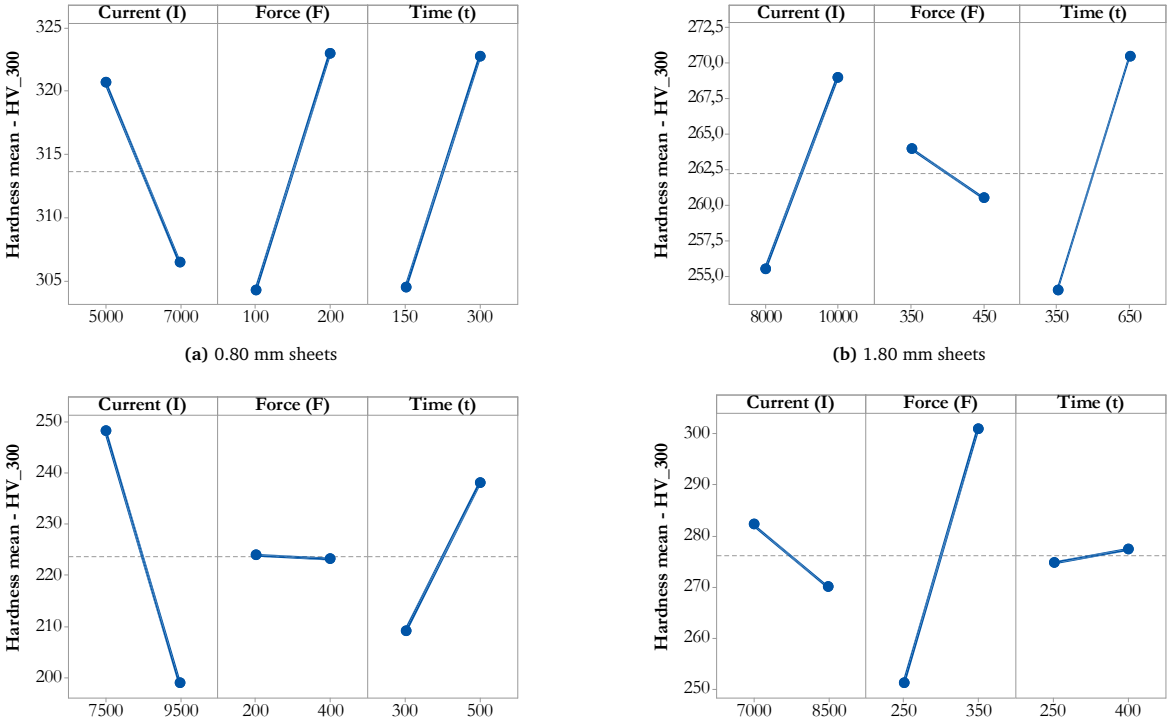

(a) 0.80 mm sheets

(b) 1.80 mm sheets

(c) 0.80 mm sheets

(d) 1.80 mm sheets

Figure 1.13 – Effect parameters on hardness for, (a) and (b) A36 steel, (c) and (d) galvanized steel

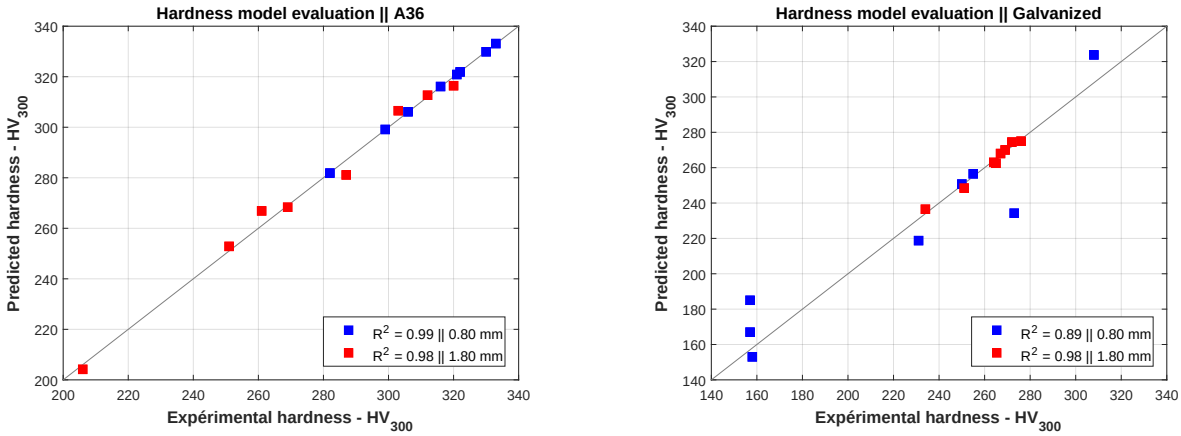

Figure 1.14 – Evaluation of predictive models for hardness, (a) A36 steel and (b) galvanized steel

1.3.4 Weld nugget diameters

A measurement of the nugget diameters of all welds was made. In order to evaluate the influence of process parameters on the diameter obtained, an analyses of variance were performed. The summaries of the results of these analyses are presented from Table 1.9 to Table 1.12. For A36 steel, welding current is the most influential parameter, followed by welding time. The pressing force has a negligible effect on the diameter of the weld nugget (Figures 14.a and 14.b). Equations 1.13 and 1.14 are the equations of predictive models of nugget diameters for small and large thickness for mild steel respectively. In the case of galvanized steel, current and time contribute positively to the size of the weld nugget, while the contribution of the pressing force remains negligible (Figures 14.c and 14.d). Equations 1.15 and 1.16 are predictive models of nugget diameters for small and large thickness of galvanized steel.

$$\emptyset_{\text{weld}} = 1.076 + 2\cdot 10^{-6} I\cdot F + 2\cdot 10^{-6} I\cdot t - 62\cdot 10^{-6} F\cdot t \tag{1.12}$$

$$\emptyset_{\text{weld}} = 37.27 - 0.004900 I - 0.07875 F - 0.02600 t + 13\cdot 10^{-6} I\cdot F + 6\cdot 10^{-6} I\cdot t - 70\cdot 10^{-6} F\cdot t \tag{1.13}$$

$$\emptyset_{\text{weld}} = 26.212 - 0.002175 I - 0.089062 F - 0.01200 t + 9.375\cdot 10^{-6} I\cdot F + 48.75\cdot 10^{-6} F\cdot t \tag{1.14}$$

$$\emptyset_{\text{weld}} = 10.23 - 575 \cdot 10^{-6} I - 0.0185 t + 2.5 \cdot 10^{-6} I \cdot t \tag{1.15}$$

Where, $\emptyset_{\text{weld}}$ is the nugget diameter of the welds.

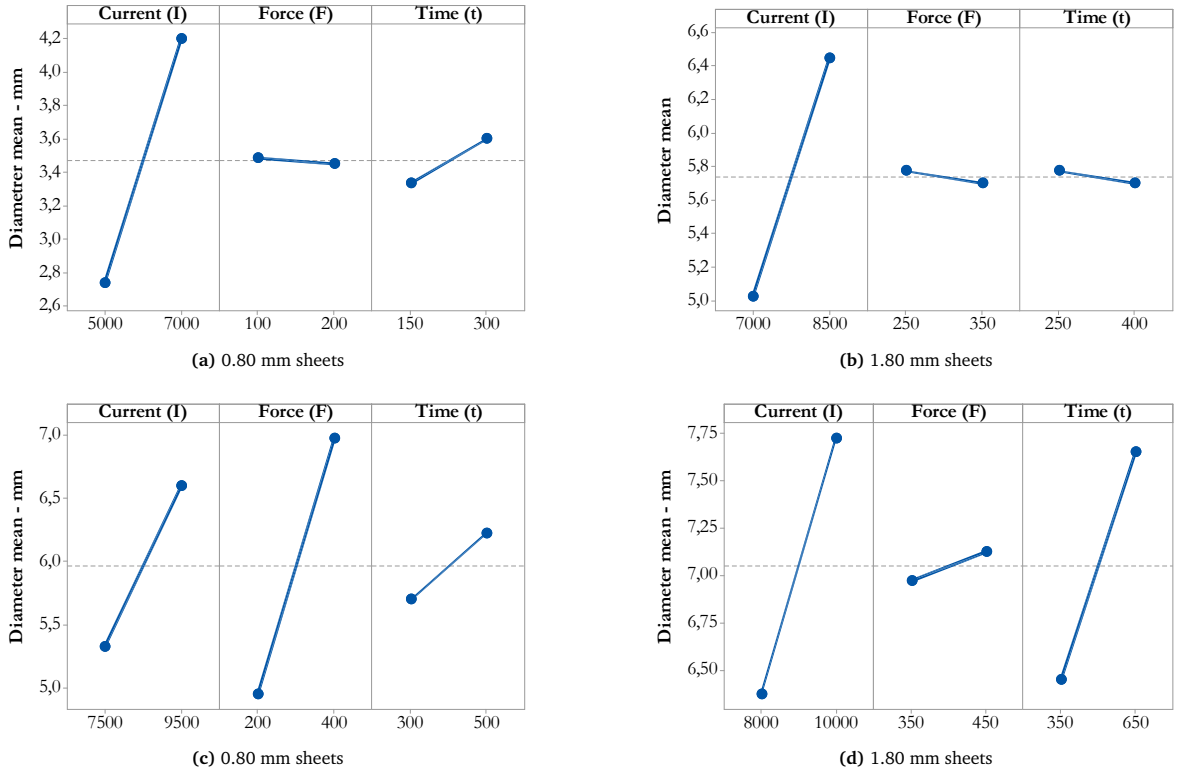

(a) 0.80 mm sheets **(b)** 1.80 mm sheets **(c)** 0.80 mm sheets **(d)** 1.80 mm sheets

Figure 1.15 – Effect of process parameters on nugget diameters for, (a) A36 steel - 0.80 mm thick, (b) A36 steel - 1.80 mm thick, (c) galvanized steel - 0.80 mm thick, and (d) galvanized steel - 1.80 mm thick

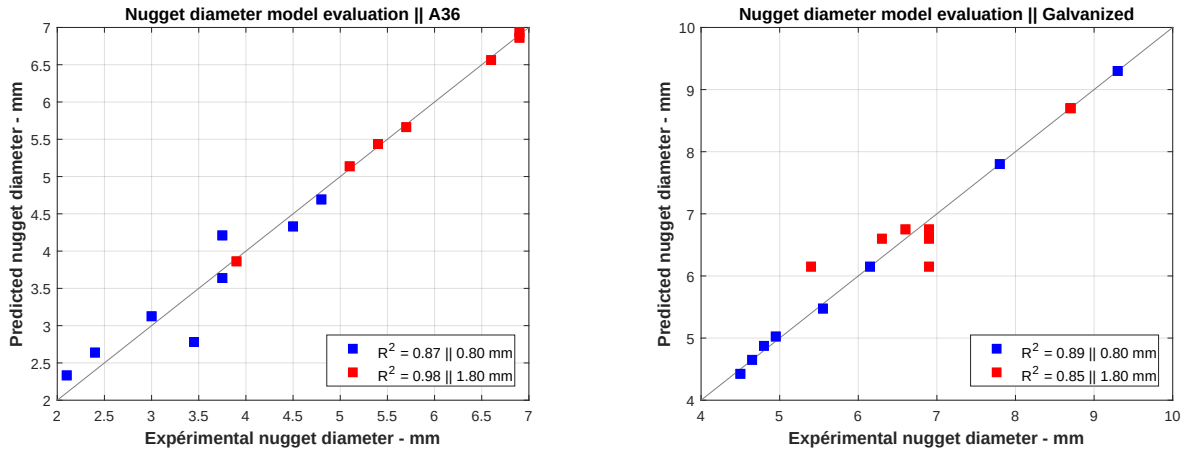

(a) **(b)**

Figure 1.16 – Evaluation of predictive models for nugget diameter, (a) A36 steel and (b) galvanized steel

Table 1.5 – ANOVA table for the hardness model, A36 steel, thickness 0.8 mm

Source	DF	Seq SS	Contribution	Adj SS	Adj MS	F-Value	P-Value
I	1	406.12	19.85%	56.901	56.901	455.21	0.030
F	1	703.13	34.37%	3.522	3.522	28.17	0.119
t	1	666.12	32.56%	186.533	186.533	1492.26	0.016
I×F	1	78.12	3.82%	78.125	78.125	625.00	0.025
I×t	1	21.13	1.03%	21.125	21.125	169.00	0.049
F×t	1	171.13	8.36%	171.125	171.125	1369.00	0.017
Error	1	0.13	0.01%	0.125	0.125		
Total	7	2045.87	100.00%				
$R^2 = 0.9999$, adjusted $R^2 = 0.9996$, predicted $R^2 = 0.9961$, prediction error $SS = 8$							

Table 1.6 – ANOVA table for the hardness model, A36 steel, thickness 1.8mm

Source	DF	Seq SS	Contribution	Adj SS	Adj MS	F-Value	P-Value
I	1	300.12	3.04%	3920.2	3920.22	76.90	0.013
F	1	4950.13	50.10%	457.3	457.34	8.97	0.096
I×F	1	2211.13	22.38%	2211.1	2211.12	43.38	0.022
I×t	1	29.20	0.30%	2303.3	2303.27	45.18	0.021
F×t	1	2288.35	23.16%	2288.3	2288.35	44.89	0.022
Error	2	101.95	1.03%	102.0	50.98		
Total	7	9880.88	100.00%				
$R^2 = 0.9897$, adjusted $R^2 = 0.9639$, predicted $R^2 = 0.8879$, prediction error $SS = 1107.33$							

1.3.5 Response surfaces of nugget hardness to diameter ratios (HV/d)

A relationship between nugget hardness, nugget diameter and overall weld quality can be established. Further analysis of the reported data was undertaken on each output variable at time :

1.3.5.1 Impact of hardness (HV) on weld quality and strength

The hardness of nugget mainly depends on the microstructural composition of the weld metal. Gould et al. [32] developed a model for the prediction of microstructure during RSW. From their model, they showed that 2 mm steel sheet could exhibit a cooling

Table 1.7 – ANOVA table for the hardness model, galvanized steel, thickness 0.8mm

Source	DF	Seq SS	Contribution	Adj SS	Adj MS	F-Value	P-Value
I	1	19190.9	78.41%	19191	19190.9	20.48	0.020
F	1	1.1	0.00%	13282	13281.7	14.17	0.033
t	1	1653.1	6.75%	20644	20644.5	22.03	0.018
I×F	1	819.2	3.35%	13527	13526.9	14.43	0.032
Error	3	2811.5	11.49%	2812	937.2		
Total	7	24475.9	100.00%				

$R^2 = 0.8851$, adjusted $R^2 = 0.7320$, predicted $R^2 = 0.4298$, prediction error $SS = 13955.9$

Table 1.8 – ANOVA table for the hardness model, galvanized steel, thickness 1.8mm

Source	DF	Seq SS	Contribution	Adj SS	Adj MS	F-Value	P-Value
I	1	364.50	28.31%	13.70	13.70	0.94	0.434
F	1	24.50	1.90%	156.10	156.10	10.77	0.082
t	1	544.50	42.29%	253.76	253.76	17.50	0.053
I×F	1	144.50	11.22%	144.50	144.50	9.97	0.087
I×t	1	180.50	14.02%	180.50	180.50	12.45	0.072
Error	2	29.00	2.25%	29.00	14.50		
Total	7	1287.50	100.00%				

$R^2 = 0.9775$, adjusted $R^2 = 0.9212$, predicted $R^2 = 0.6396$, prediction error $SS = 464$

Table 1.9 – ANOVA table for the nugget diameter model, A36 steel thickness 0.8mm

Source	DF	Seq SS	Contribution	Adj SS	Adj MS	F-Value	P-Value
I×F	1	0.7132	11.45%	2.4757	2.4757	11.80	0.026
I×t	1	1.5248	24.48%	4.3145	4.3145	20.56	0.011
F×t	1	3.1523	50.60%	3.1523	3.1523	15.02	0.018
Error	4	0.8394	13.47%	0.8394	0.2099		
Total	7	6.2297	100.00%				

$R^2 = 0.8653$, adjusted $R^2 = 0.7642$, predicted $R^2 = 0.3753$, prediction error $SS = 3.8915$

Table 1.10 – ANOVA table for the nugget diameter model, A36 steel thickness 1.8mm

Source	DF	Seq SS	Contribution	Adj SS	Adj MS	F-Value	P-Value
I	1	4.06125	54.45%	1.93706	1.93706	172.18	0.048
F	1	0.01125	0.15%	0.98005	0.98005	87.12	0.068
t	1	0.01125	0.15%	0.21158	0.21158	18.81	0.144
I×F	1	1.90125	25.49%	1.90125	1.90125	169.00	0.049
I×t	1	0.91125	12.22%	0.91125	0.91125	81.00	0.070
F×t	1	0.55125	7.39%	0.55125	0.55125	49.00	0.090
Error	1	0.01125	0.15%	0.01125	0.01125		
Total	7	7.45875	100.00%				

$R^2 = 0.9985$, adjusted $R^2 = 0.9894$, predicted $R^2 = 0.9035$, prediction error SS $= 0.72$

Table 1.11 – ANOVA table for the nugget diameter model, galvanized steel thickness 0.8mm

Source	DF	Seq SS	Contribution	Adj SS	Adj MS	F-Value	P-Value
I	1	3.2513	15.51%	3.78450	3.78450	336.40	0.003
F	1	8.2012	39.13%	7.11003	7.11003	632.00	0.002
t	1	0.5513	2.63%	1.15200	1.15200	102.40	0.010
I×F	1	7.0313	33.55%	7.03125	7.03125	625.00	0.002
F×t	1	1.9013	9.07%	1.90125	1.90125	169.00	0.006
Error	2	0.0225	0.11%	0.02250	0.01125	-	-
Total	7	20.9588	100.00%	-	-	-	-

$R^2 = 0.9989$, adjusted $R^2 = 0.9962$, predicted $R^2 = 0.9828$, prediction error $SS = 0.3600$

Table 1.12 – ANOVA table for the nugget diameter model, galvanized steel thickness 1.8mm

Source	DF	Seq SS	Contribution	Adj SS	Adj MS	F-Value	P-Value
I	1	3.645	40.50	0.2184	0.2184	0.65	0.466
t	1	2.880	32.00%	0.7513	0.7513	2.23	0.210
I×t	1	1.125	12.50%	1.1250	1.1250	3.33	0.142
Error	4	1.350	15.00%	1.3500	0.3375		
Total	7	9.000	100.00%				

$R^2 = 0.8500$, adjusted $R^2 = 0.7375$, predicted $R^2 = 0.4000$, prediction error $SS = 5.4000$

rate of $2000°C \cdot s^{-1}$. Such high cooling speed is due to the presence of a cooling liquid in the electrodes and the short welding times. Martensitic microstructure is generally observed in the nugget due to those high cooling speeds. This observation is in good agreement with the work Goodarzi et al. [33], who found that the microstructure of resistance spot welds of galvanized low carbon steel was nearly fully martensitic. Thus, when the hardness of a resistance spot weld is very high, it generally means that the metal has been hardened, heat has dissipated quite quickly, which leaded to the formation of martensite. However, it is well known that to obtain good quality welds, martensite formation must be avoided as much as possible [22]. Thus, in a good weld, metals should have time to melt and join in the presence of necessary heat, cooling should be relatively slow and metal should have time to reconsolidate, which should lead to a much lower and homogeneous hardness.

1.3.5.2 Impact of nugget diameter (d) on weld quality and strength

An increase in the nugget diameter leads to an increase in the contact surface area between welded sheets and consequently to an increase in the mechanical strength of the welds. Thus, HV/d ratio is a good way to control the quality and strength of welds. Indeed, it can be drawn from the previous points that the weld is all the more resistant when this ratio decreases and vice versa. In order to practically see the effects of each welding parameter on HV/d ratio, response surfaces have been plotted (Figure 1.17 and 1.18).

Thus, HV/d ratio is a good way to control the quality and strength of welds. Indeed, it can be drawn from the previous points that the weld is all the more resistant when this ratio decreases and vice versa. In order to practically see the effects of each welding parameter on HV/d ratio, response surfaces have been plotted (Figure 1.17 and 1.18).

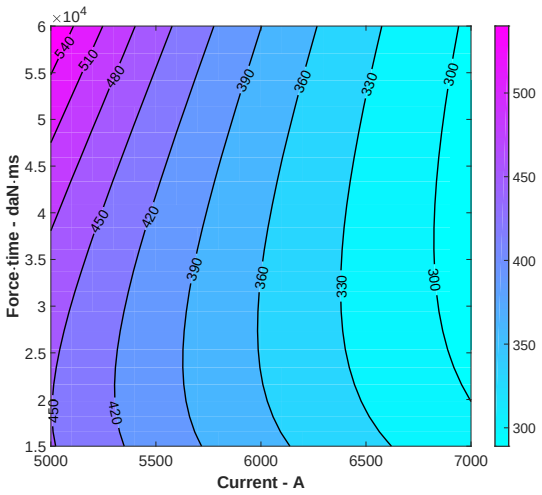

(a) (a) 0.80 mm sheets

(b) (a) 1.80 mm sheets

Figure 1.17 – Response surface of HV/d ***versus*** $F \cdot t$ and I for A36 mild steel with HV/d in $\left[\mathrm{HV}_{300} \cdot \mathrm{mm}^{-1}\right]$

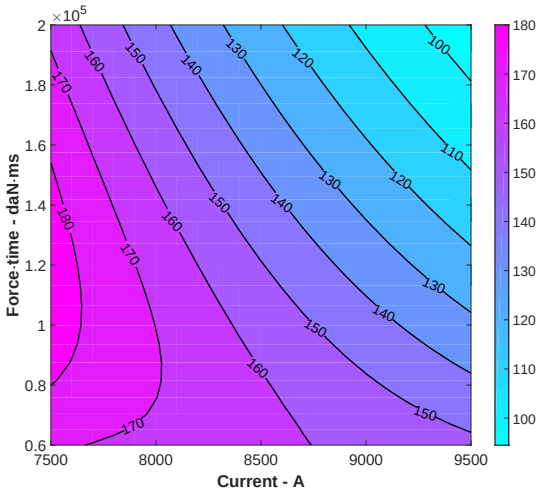

(a) (a) 0.80 mm sheets

(b) (a) 1.80 mm sheets

Figure 1.18 – Response surface of HV/d ***versus*** $F \cdot t$ and I for galvanized steel with HV/d in $\left[\mathrm{HV}_{300} \cdot \mathrm{mm}^{-1}\right]$

It can be seen on Figure 1.17.a that in order to minimize the HV/d ratio, it is ineluctable to increase welding current. Even though force and time have less effect on HV/d ratio, they should be minimized in order to reduce the ratio. For 1.8mm A36 sheets (Figure 1.17.b), it is seen that current should be maximized and both force and time should be minimized in order to reach lowest value of HV/d ratios. For galvanized steel (Figure 1.18), it is clearly seen that to achieve lowest value of HV/d ratio, all welding parameters must be maximized. This is due to the presence of zinc coating on sheets

faying surface. Heat is generated in steel through resistance to current flowing, as zinc is a good electrical conductor, it's a way for heat losses and thus, more current, force and time are needed to overcome these losses and successfully weld galvanized steel.

1.4 Conclusion

In this work, effects of process parameters in resistance spot welding were evaluated. The study was carried out on two steel grades, ASTM A36 mild steel and ASTM A653 hot dipped galvanized steel. Steel specimens were welded according to predefined factorial plans. Micrographic analysis and micro-indentation hardness tests revealed welds quality. Based on the results of these tests, ANOVAs were conducted to determine the influence of welding parameters on the geometry and hardness of welds and to establish predictive models. Response surface methodology was then used to simultaneously relate nugget hardness and nugget diameter to process parameters. The main conclusions of this work are as follows :

- There is an increase in hardness of 168% and 127% in the melting zone as compared to the base metal for A36 mild and galvanized steel respectively.
- Welding current is the most influential parameter and averagely contributes for 32.18% and 30% to the nugget hardness and diameter respectively.
- Welding time averagely contributes for 20.40% and 21.34% to the nugget hardness and diameter respectively.
- Welding force averagely contributes for 21.60% and 9.82% to the nugget hardness and diameter respectively.
- The hardness to nugget diameter ratio (HV/d) can be used to foresee the overall weld quality and strength, the smaller the HV/d ratio, the stronger the weld is.
- For A36 mild steel sheets, current should be maximized while force and time should be minimized in order to achieve good quality welds.
- For galvanized steel sheets, current, force, and time should be maximized in order to achieve good quality welds. That is due to the presence of zinc coating in the faying surface of sheets.

Chapitre 2

Multi-Objective Optimization of Process Parameters in Resistance Spot Welding of A36 Mild Steel and Hot Dipped Galvanized Steel Sheets Using Non-dominated Sorting Genetic Algorithm

Science and Technology of Welding and Joining - Taylor & Francis

B. V. Feujofack Kemda[ψ,*], N. Barka[ψ], M. Jahazi[χ] and D. Osmani[ζ]

Sommaire

Submitted on November 03rd 2019

**Corresponding author - E-mail address :*bleriotvincent.feujofackkemda@uqar.ca (B. V. Feujofack K.)
[ψ] *University of Quebec in Rimouski, Québec G56 3A1, Canada.*
[χ] *Ecole de Technologie Superieure, Montréal, Québec H3C 1K3, Canada.*
[ζ] *AMH Canada Ltd, Rimouski, Québec G5L 1Z2, Canada.*

Avant-propos

Auteurs et affiliations

Blériot Vincent Feujofack Kemda : Étudiant en maîtrise en ingénierie, Département de mathématiques, d'informatique et de génie, Université du Québec à Rimouski, Rimouski, Québec G56 3A1, Canada.

Noureddine Barka : Professeur, Département de mathématiques, d'informatique et de génie, Université du Québec à Rimouski, Rimouski, Québec G56 3A1, Canada.

Mohammad Jahazi : Département de génie mécanique, École de technologie supérieure, Montréal, Québec H3C 1K3, Canada.

Denis Osmani : AMH Canada Ltée, Rimouski, Québec G5L 1Z2, Canada

Titre en Français

Optimisation multi-objective des paramètres de procédé dans le soudage par résistance par points de tôles d'acier doux A36 et d'acier galvanisé à chaud en utilisant un algorithme génétique à tri de non-dominance.

État de l'article

Soumis pour publication au journal : « Science and Technology of Welding and Joining ».

Contribution au mémoire

Cet article constitue la deuxième partie de ce mémoire ; il est basé sur les résultats expérimentaux obtenus dans le premier article. L'approche proposée ici visait l'optimisation des paramètres de procédé dans le SRP avec prise en compte simultanée de plusieurs critères de qualité, à savoir la dureté et la résistance à la traction/cisaillement, qui sont des propriétés mécaniques ; et le diamètre des noeuds, qui est une variable de sortie géométrique. D'autre part, l'algorithme d'optimisation utilisé (NSGA-II) offre une approche permettant de surmonter le problème de la

stagnation à l'optimum local lors du processus d'optimisation et permet de résoudre des problèmes convexes encore appelés problèmes avec optimums indifférents.

Résumé en Français

L'industrie évolue constamment vers une augmentation de la vitesse de production tout en minimisant les coûts. Cet article présente une méthode efficace pour minimiser les temps de production et les énergies grâce à l'optimisation des paramètres du procédé de soudage par résistance par points. Deux nuances d'acier ont été utilisées dans cette étude : l'acier ASTM A36 et l'acier galvanisé par immersion à chaud A653. L'analyse micrographique a révélé la microstructure des soudures tandis que les essais de dureté par micro-indentations ont permis d'établir des profils de dureté le long des noeuds de soudure. Des essais de traction-cisaillement ont été réalisés afin de quantifier la résistance mécanique des soudures. Une analyse de variance a montré que le courant de soudage est le paramètre le plus important et contribue pour environ 70% à la résistance mécanique des soudures. Le rapport de la dureté dans la zone de fusion à la surface du noeud de soudure etait corrélé avec le mode de rupture des échantillons soudés. Sur cette base, une optimisation multi-objective des paramètres de procédé, à travers l'algorithme génétique par tri de non dominance (NSGA-II), a été réalisée. Cette optimisation s'est traduite par une réduction du courant, de la force de pressage des électrodes et du temps de soudage de 10.58%, 13.59% et 32.61% respectivement. Les paramètres optimisés ont ensuite été évalués par des essais de traction-cisaillement des éprouvettes soudées, toutes les éprouvettes ont réussi les essais de validation en subissant une rupture dans le métal de base.

Abstract

Industry is constantly moving towards an increasing of production speed while minimizing production costs. This paper presents an efficient method for minimizing production times and energies through optimization of process parameters in resistance spot welding (RSW). Two grades of steel were used in this study, ASTM A36 steel and A653 hot dipped galvanized steel. Welding was done in overlap configuration, grade for grade, while following complete factorial plans. Micrographic analysis revealed welds microstructure while micro-indentation hardness tests enabled to establish hardness profiles along weld nuggets. Tensile-shear tests have been carried out in order to quantify the mechanical strength of welds. Analysis of variance showed that welding current is the most significant parameter and contributes for about 70% to welds mechanical strength. The ratio of hardness in the fusion zone to nugget surface area was found to be correlated with the failure mode of welded specimens. On that basis, a multi-objective optimization of the process parameters, through the non-dominated sorting genetic algorithm was performed. This optimization resulted in a reduction of current, electrode pressing force and welding time of 10.58%, 13.59% and 32.61% respectively. Optimized parameters were then assessed trough tensile-shear testing of welded specimens, all specimens passed the validation tests by experiencing failure in the base metal.

Keywords : Resistance spot welding ; Hardness ; Nugget diameter ; Tensile-shear strength ; Optimization ; Genetic algorithm

2.1 Introduction

Resistance spot welding (RSW) is intensively used in thin sheet assembly. Welds are obtained by a transient combination of heat, pressure and time [9, 26]. It's a fast welding technique and due to its facility to be automated, it's widely used in automotive industry [34, 35]. To meet challenges of automotive industry regarding emissions, strength and sustainability, many aspects of this manufacturing process need to be improved [31, 36]. Among issues to be solved, one can cite high production cost due energy consumption

during welding. Optimization of process parameters will enable to achieve strong welds while using less energy and time.

2.1.1 Optimization of process parameters

During RSW, the greater the indentation left by the electrode, the more resistant the weld is. In order to obtain indentations of up to 25% of the plate thickness, Kumar and Vijayajumar [15] optimized resistance welding parameters of AISI 304L using Taguchi method, their optimization was done on the basis of only one quality criterion which was nugget indentation. Pashazadeh et al. [16] conducted a study to optimize machine parameters during the RSW in order to obtain better weld nuggets geometry. They began by designing a complete factorial experiment of three factors at two levels, including current, pressing force and welding time. They proceeded to the actual optimization through a hybrid combination of artificial neural networks and the multi-objective genetic algorithm. The optimized parameters were validated with prediction errors of 1.28% and 6.98% on nuggets diameter and height respectively.

Some works were also carried out on the optimization of process parameters with mechanical strength as quality criterion. It is the case of Suresh [17] who worked on a systematic approach for determining optimum process parameters in order to maximize tensile strength (shear). The tests were conducted on 1 mm thick corrugated mild steel specimens. In their study, studied parameters were current, time and electrode diameter. A L27 orthogonal matrix was used. The weld that exhibited the highest tensile strength was obtained with a current of 17.5 kA, a welding time of 15 s and an electrode diameter of 3 mm. The analysis of variance (ANOVA) showed that current is the most influential parameter (63.70%), followed by welding time (28.70%) for the tensile strength of welds. Pandey et al. [20] optimized the RSW process parameters using Taguchi's method. The material used in the study was mild steel sheets (AISI 1008/ ASTM A366), sheets were 0.9 mm thick. The quality criterion in their optimization was mechanical strength. The optimization made indicates that with a current of 6.8 kA, a pressure of 0.79 kPa and a time of 5 s, welding of very good resistance could be achieved.

At this level, it can be observed that many researchers focused on optimizing one quality at a time, namely, weld geometry or weld strength. This kind of approach can lead to a partial optimization of the process because by optimizing a single output, one can lose in performance with respect to the other output variables. As the industry is constantly evolving towards the optimization of the entire process, it becomes essential to focus on several output variables at once. Muhammad et al. [37], in particular, carried out a work to optimize process parameters in RSW with simultaneous consideration of multiple responses using Taguchi's multi-objective method for experimental design and the response surface method for final optimization. The main quality criteria taken into account during the optimization process were nugget diameter and width of the heat-affected zone (HAZ). The ANOVA method enabled them to determine the contributions and confidence levels of each factor. The predictive model developed using response surfaces enabled them to obtain optimal parameters. These parameters were validated with an error of 0.34% and 1.89% for node diameter and HAZ width respectively. Even though they performed a multi-objective optimization, both of the two quality criteria were geometry-based. A multi-objective optimization of process parameters based on both geometrical and mechanical strength criteria will be of great importance and will lead to a better understanding of the process. Up to this date, no such work has been carried out, hence the interest of the authors in such investigations. Furthermore, optimization of process parameters in RSW have always been done through Taguchi method. Stochastic techniques such as genetic algorithms (GA) are well known for overcoming local optimum problems and for handling multi-objective problems. GAs can be successfully used to get effective optimum welding parameters in RSW.

2.1.2 Non-dominated sorting genetic algorithm (NSGA)

Metaheuristic methods are widely used in optimization problems. Interest in research algorithms inspired by nature and physical processes began in the early 1970s, with Holland [38], who was the first to propose genetic algorithms [39]. Genetic algorithms (GAs) are based on biological evolution, and are part of the field of computer

simulation of evolution which offer an approach to overcome the problem of stagnation at the local optimum during optimization process [40]. The main difference between genetic algorithms and evolutionary strategies is that GAs are based on crossover, a mechanism for exchanging probabilistic and important information between solutions to locate the best solutions, while evolutionary strategies use mutation as the main research mechanism [39]. Another advantage, not the least is that genetic algorithms make it possible to solve convex problems still called problems with indifferent optimums [41]. In short, GAs are a robust and effective way to solve optimization problems in real life where heuristic methods often offer unsatisfactory solutions. Problems with more than one objective function require a multi-objective technique for their resolution. There are currently several multi-objective optimization techniques that are the improvement of single objective optimization by GA, they include the Multi objective genetic algorithm (MOGA), Non-dominated sorting genetic algorithm II (NSGA-II), Strength Pareto evolutionary algorithm (SPEA), Micro genetic algorithm (Micro-GA), Pareto-archived evolution strategy (PAES). Of all the multi-objective genetic algorithm optimization techniques (MoGA), NSGA-II has been the most widely used for process parameter optimization [42–44]. With its fast non-dominated sorting property, an elitist strategy and a parameterless approach, the NSGA-II proposed by Deb et al [45] is one of the most effective methods of optimization in engineering problems. This algorithm allows convincing results to be achieved in a minimum of time. The main functions of this algorithm are randomization, classification (elitist selection), crossover and mutation. Figure 2.1 shows the operating diagram of this algorithm.

As a general rule, NSGA-II can be roughly detailed as follows : initially, a random parent population (P_0) is created. The population is sorted according to non-dominance. Each solution is assigned a fitness level (or rank) equal to its non-dominance level (1 is the best level, 2 is the second best level, etc.) [45]. Thereafter, the algorithm enters its main loop (Figure 2.2), crossover and mutation are applied to a parents population P_t of size n to generate a children population Q_t of size n as well. The combination of parent and child populations ($P_t \cup Q_t$) forms a new population (R_t) of size $2n$. This new population is sorted according to non-dominance. Since all individuals of the previous

and current population are found in R_t, elitism is assured. Now, solutions belonging to the best non-dominated set (F_1) are the best solutions in the combined population (R_t) and should be highlighted more than any other solution in the combined population. If the size of (F_1) is smaller than n, all the members of the set (F_1) are definitely chosen for the new parents population (P_{t+1}) . The remaining members of the population (P_{t+1}) are chosen from the next non-dominated fronts in the order of their ranking. Thus, the solutions of set (F_2) are chosen next, followed by the solutions of set (F_3) , and so on. This procedure is continued until there is no more space available in the population (P_{t+1}) . To choose exactly n members for the population (P_{t+1}) , solutions of the last front are sorted using the crowded comparison operator ($<_n$) in descending order by choosing the best solutions to fill all the cells of the population (P_{t+1}) . Every optimization problem solved by the NSGA II is generally defined as follows :

$$\text{Minimize } : f(x) = (f_1(x), f_2(x), \ldots, f_n(x)) \tag{2.1}$$

$$\text{Subject to : } g_j(x) \leq 0, j = 1, 2, \ldots, q \tag{2.2}$$

$$x = (x_1, x_2, \ldots, x_n) \tag{2.3}$$

$$x_i^{\min} \leq x_i \leq x_i^{\max}, i = 1, 2, \ldots, n \tag{2.4}$$

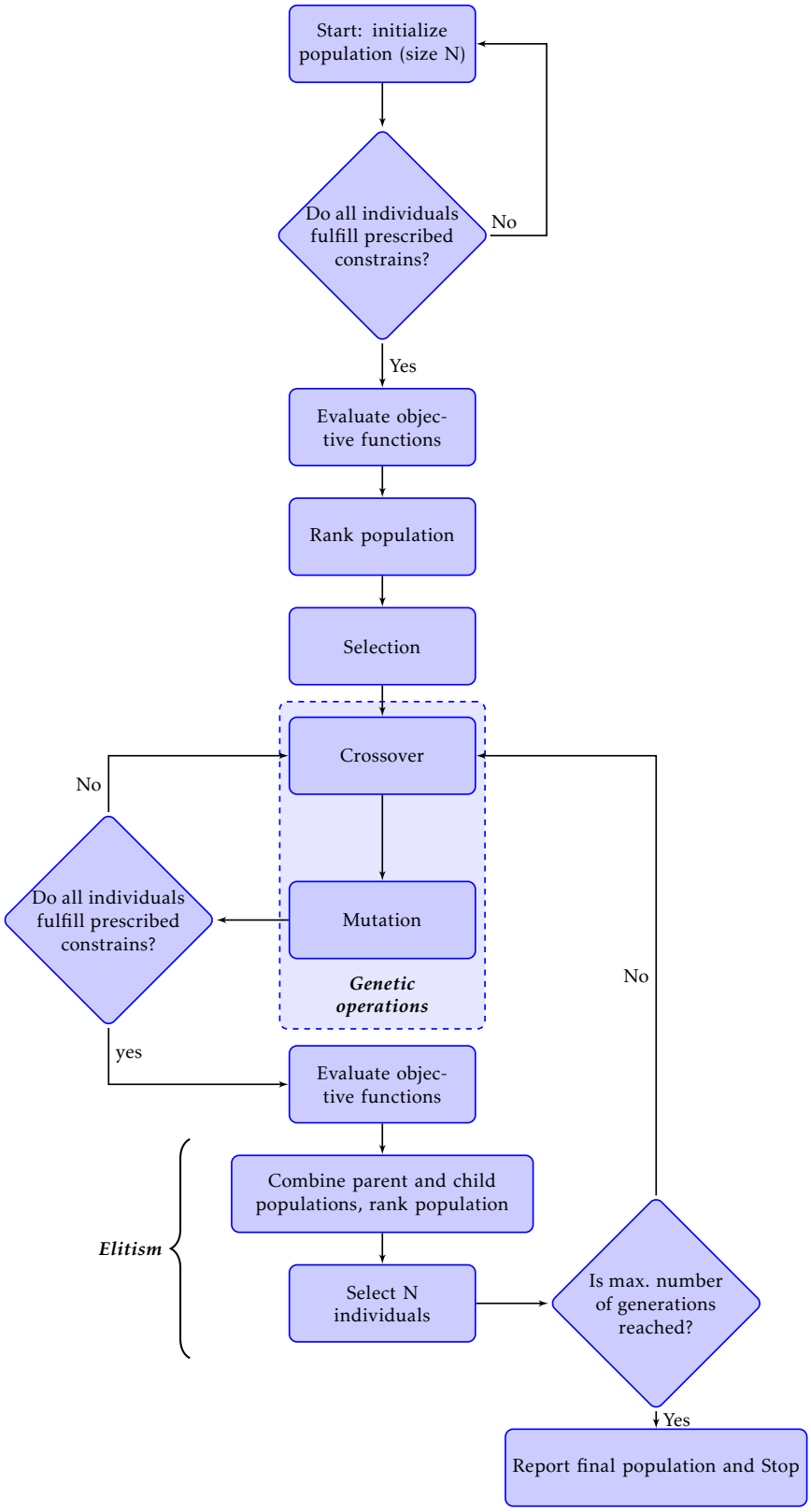

Figure 2.1 – Organization chart of NSGA-II based program

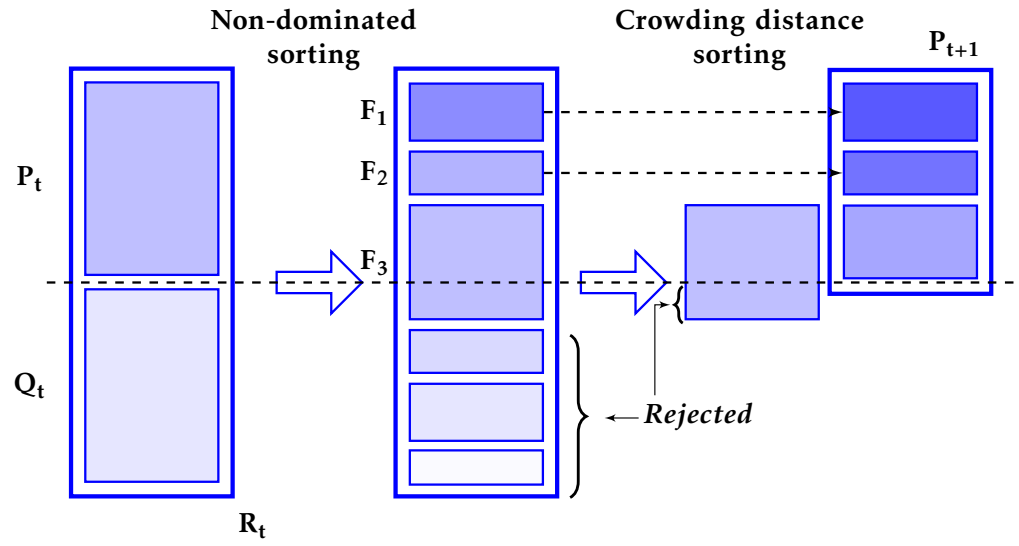

Figure 2.2 – NSGA-II procedure

In this work, the effect of welding parameters on the hardness and diameter of weld nuggets was evaluated. A multi-objective optimization using the NSGA-II, taking as quality criteria both nugget geometry and nugget mechanical strength has made it possible to determine the optimal welding parameters leading to good quality welds. The approach developed in this work can be used in RSW of thin steel sheets for the automotive industry, it leads to a reduction in production times and energies while extending the overall service life of welding machines.

2.2 Materials and methods

2.2.1 Materials

ASTM A36 mild steel and ASTM A653 hot dipped galvanized steel with thicknesses of 0.80 mm and 1.80 mm each were used in this work. Their chemical compositions are given in Table 2.1 and their mechanical characteristics in Table 2.2.

Table 2.1 – ASTM A36 steel and ASTM A653 hot dipped galvanized steel, chemical composition in %*.

Material	C	Mn	P	S	Cu	Si	Ni	Cr	Mo	Cb	V	Ti	Fe
A36	0.27	1.03	0.04	0.05	0.20	0.280	< 0.1	< 0.08	< 0.1	-	-	-	
A653	0.15	0.60	0.03	0.035	0.25	-	0.2	0.15	0.06	0.008	0.008	0.025	

**Typical composition*

Table 2.2 – Mechanical properties of A36 steel and A653 hot dipped galvanized steel

Material	Yield strength (MPa)	Ultimate tensile strength (MPa)	Elongation (%)	Hardness (HV)
A36	441.3	503.3	30	120
A653	277.5	363.8	37.5	121

**Typical composition*

2.2.2 Experimental considerations

Steel plates were welded in overlap configuration, grade for grade and thickness for thickness similar (Figure 2.3). Prior to final welding tests, weldability experiments were carried out in order to find out extreme values of process parameters. These values were used to design complete factorial plans of three factors at two level for specimen welding (Tables 2.3 and 2.4).

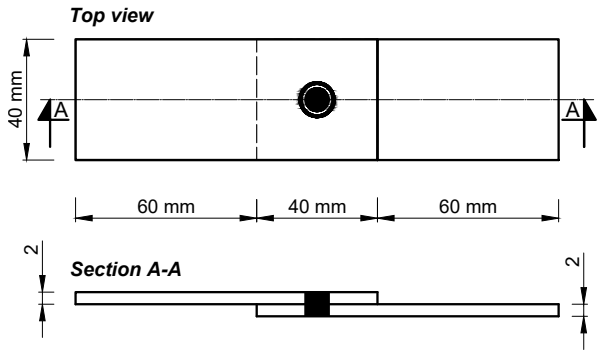

Figure 2.3 – Arrangement of steel sheets

Table 2.3 – Design of experiment for A36 mild steel

Thickness - 0.80 mm				Thickness - 1.80 mm			
#	$I(A)$	$F(daN)$	$t(ms)$	#	$I(A)$	$F(daN)$	$t(ms)$
1	5000	100	150	1	7000	250	250
2	5000	100	300	2	7000	250	400
3	5000	200	150	3	7000	350	250
4	5000	200	300	4	7000	350	400
5	7000	100	150	5	8500	250	250
6	7000	100	300	6	8500	250	400
7	7000	200	150	7	8500	350	250
8	7000	200	300	8	8500	350	400

Table 2.4 – Design of experiment for A653 galvanized steel

Thickness - 0.80 mm				Thickness - 1.80 mm			
#	$I(A)$	$F(daN)$	$t(ms)$	#	$I(A)$	$F(daN)$	$t(ms)$
1	7500	200	300	1	8000	350	350
2	7500	200	500	2	8000	350	650
3	7500	400	300	3	8000	450	350
4	7500	400	500	4	8000	450	650
5	9500	200	300	5	10000	350	350
6	9500	200	500	6	10000	350	650
7	9500	400	300	7	10000	450	350
8	9500	400	500	8	10000	450	650

Following each combination of parameters, three welded specimens were made for tensile tests while one specimen was prepared for micrographic analysis and micro-indentation hardness test.

2.2.2.1 Micro-indentation hardness tests and micrography

Micro-indentation hardness measurements were made for all weldments according to ASTM E384-17 [28] and in “Z” pattern along the cross-section of the welds (Figure 2.4).

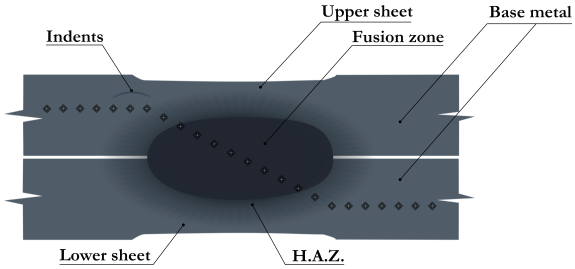

Figure 2.4 – Micro-hardness indentation pattern

2.2.2.2 Tensile test

In order to characterize the mechanical behavior of welds, static loading tensile tests were carried out on all welded specimens. Specimens were prepared in advance to meet the geometric standards of ASTM E8-M [46]. These tests were conducted on the MTS 810 machine in the RD/Project laboratory of the Mechanical Engineering Department of the University of Quebec at Rimouski. Specimens were tested with initial and secondary loading speeds of 1 and 5 mm/s, in order to comply with the deformation rate indicated by the ASTM E8-M standard. Tensile tests made it possible to make a final judgment on the quality of each weld. During tensile tests, a phenomenon of weld rotation was found to be omnipresent. This can be explained as follows : at the beginning of the test, the specimen is initially subjected to two opposite forces, thus subjecting the weld interface to shear (Figure 2.5.a). Since the forces applied by the machine are slightly eccentric, a moment is created (Figure 2.5.b). That moment slowly rotates the specimen around the transversal axis of the weld until the two forces get aligned (Figure 2.5.c). This phenomenon has been called : primary deformation of the weld. However, ruptures can occur before these forces get aligned, as in the case of interfacial failure mode.

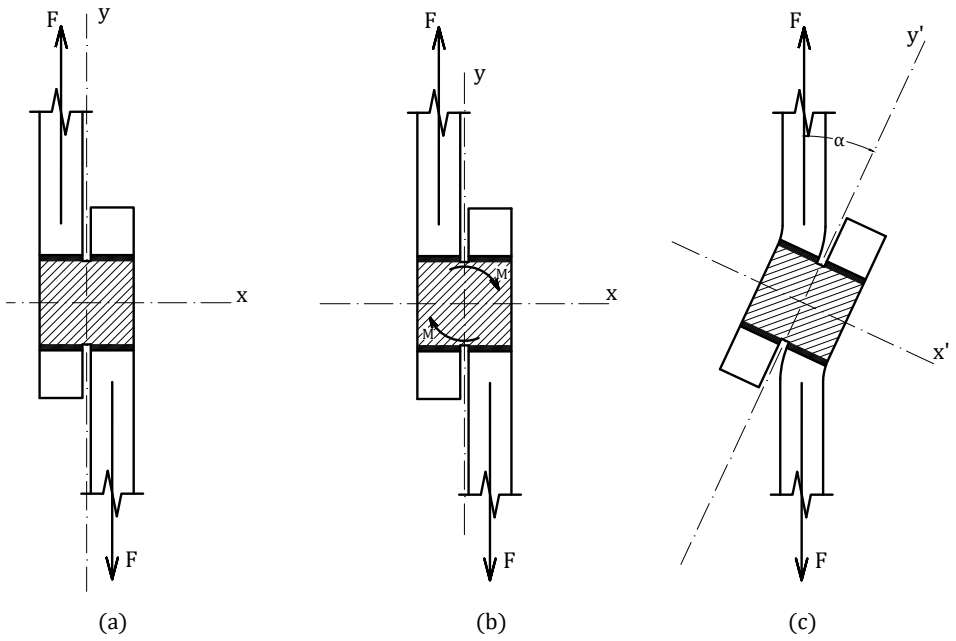

Figure 2.5 – Principle of primary deformation of the weld

2.3 Results and discussions

2.3.1 Welds hardness

Following micro-indentation hardness tests, convincing results have been obtained and will be presented. Analyses of variance (ANOVA) of hardness in the fusion zone and nugget diameter were carried out. Table 2.5 gives a summary of predictive models obtained from analyses.

Table 2.5 – Predictive models for hardness and nugget diameters (obtained from ANOVA)

Output variable	Sheet specifications	Equation
Nugget hardness $[HV_{300}]$	0.8 mm A36 sheets	$\mathrm{H\,V_{300}} = 286.25 - 0.011625I + 0.0900F + 0.4367t + 63\cdot10^{-6}I\cdot F - 22\cdot10^{-6}I\cdot t - 0.001233F\cdot t$ (2.5)
	1.8 mm A36 sheets	$\mathrm{H\,V_{300}} = 1221 - 0.1909I - 1.669F + 443\cdot10^{-6}I\cdot F + 153\cdot10^{-6}I\cdot t - 3905\cdot10^{-6}F\cdot t$ (2.6)
	0.8 mm galvanized sheets	$\mathrm{H\,V_{300}} = 167.3 - 2.830F + 2.726t + 333\cdot10^{-6}I\cdot F - 304\cdot10^{-6}I\cdot t$ (2.7)
	1.8 mm galvanized sheets	$\mathrm{H\,V_{300}} = 352 - 0.0114I - 0.800F + 0.340t + 85\cdot10^{-6}I\cdot F - 32\cdot10^{-6}I\cdot t$ (2.8)
Nugget diameter [mm]	0.8 mm A36 sheets	$\emptyset_{soud} = 1.076 + 2\cdot10^{-6}\mathrm{I}\cdot F + 2\cdot10^{-6}\mathrm{I}\cdot\mathrm{Ft} - 62\cdot10^{-6}\mathrm{F}\cdot t$ (2.9)
	1.8 mm A36 sheets	$\emptyset_{soud} = 37.27 - 0.004900I - 0.07875F - 0.02600t + 13\cdot10^{-6}I\cdot F + 6\cdot10^{-6}I\cdot t - 70\cdot10^{-6}F\cdot t$ (2.10)
	0.8 mm galvanized sheets	$\emptyset_{soud} = 26.212 - 0.002175I - 0.089062F - 0.01200t + 9.375\cdot10^{-6}I\cdot F + 48.75\cdot10^{-6}F\cdot t$ (2.11)
	1.8 mm galvanized sheets	$\emptyset_{soud} = 10.23 - 575\cdot10^{-6}I - 0.0185t + 2.5\cdot10^{-6}I\cdot t$ (2.12)

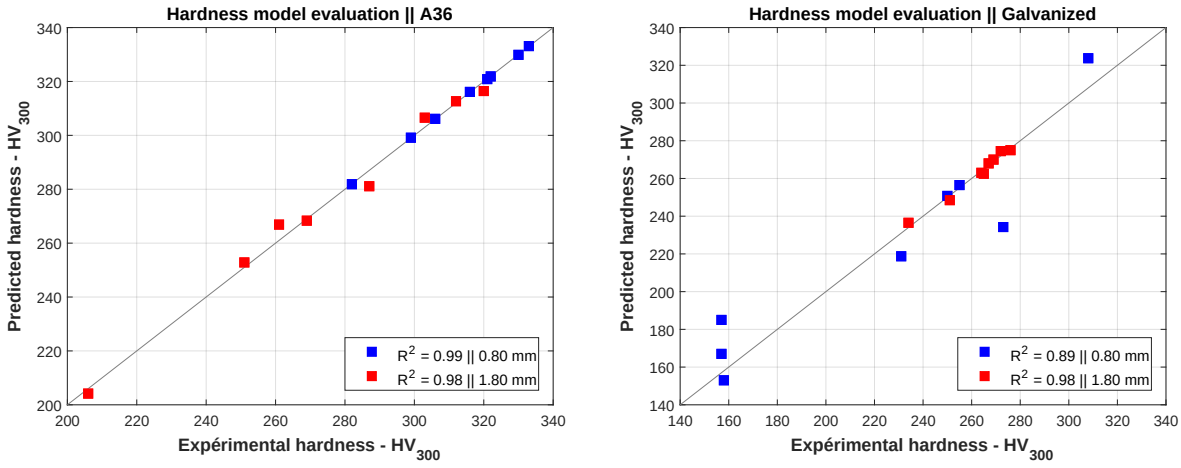

(a) A36 steel **(b)** Galvanized steel

Figure 2.6 – Evaluation of weld hardness predictive models

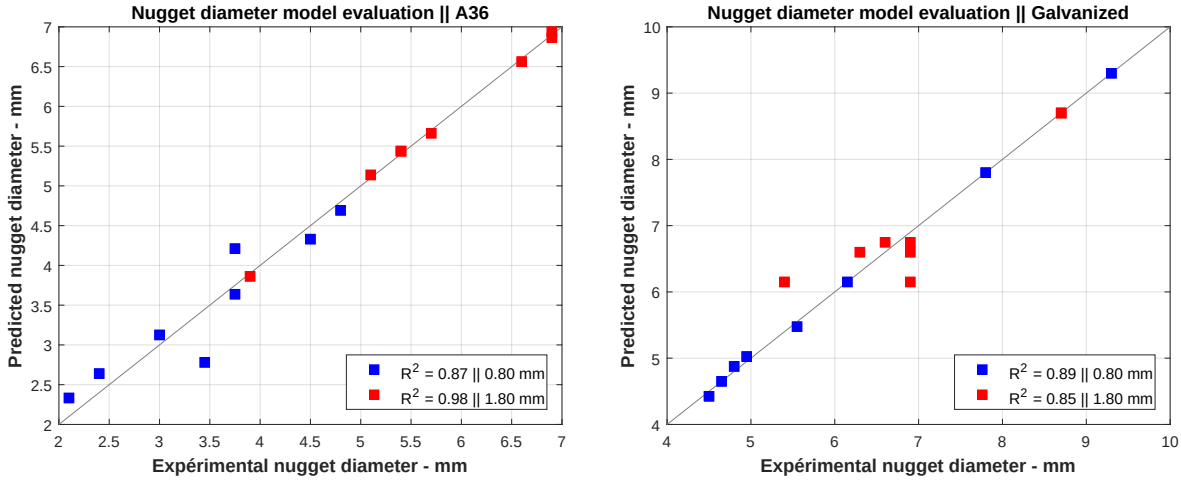

(a) A36 steel **(b)** Galvanized steel

Figure 2.7 – Evaluation of predictive models of nugget diameters

2.3.2 Mechanical strength of welds

Mechanical tests, namely static loading tensile tests, made it possible to make a final judgement on weld performances. Tested specimens failed in various ways. A definition of the failure modes was made in order to successfully complete the study.

2.3.2.1 Failure modes

Failures were classified into two major modes according to their position and the nature of stresses in the weld.

2.3.2.1.1 Interfacial failure mode (IF mode)

Here, the rupture occurs in the sheet faying surfaces. This failure mode generally indicates the lack of energy during welding.

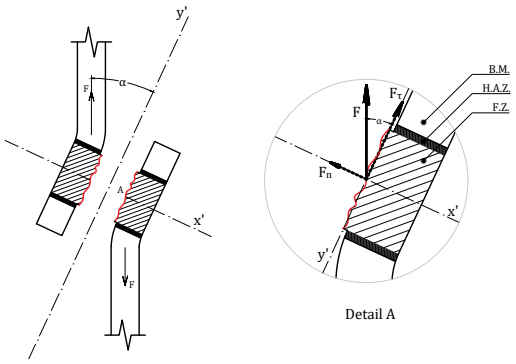

(a) Illustration

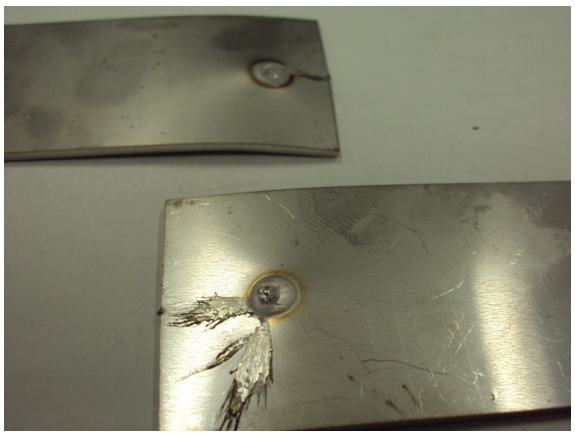

(b) Failure

Figure 2.8 – Interfacial failure

In this case, nugget faying surface undergoes both shear and cross tension solicitations. Failure stresses can be calculated as follows :

$$\tau_{ZF} = \frac{4F \cdot \cos\alpha}{\pi d^2} \tag{2.13}$$

$$\sigma_{ZF} = \frac{4F \cdot \sin\alpha}{\pi d^2} \tag{2.14}$$

Where τ_{ZF} and σ_{ZF} are respectively failure shear stress and normal stress, F the failure tensile force and d the weld nugget diameter.

2.3.2.1.2 Button pullout mode (BP mode)

A failure by nugget pullout signifies the high strength of the weld. The more the weld is, the more the probability to get a button pullout failure mode.

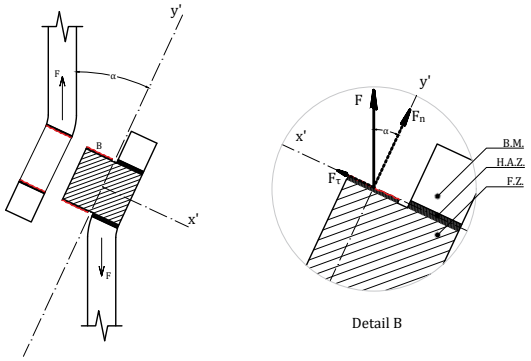

(a) Illustration

(b) Failure

Figure 2.9 – Button pullout

For button pullout failure mode, nugget is solicited on it circumference (Figure 2.10). Stresses are assumed to have a harmonic distribution around the nugget, thus :

$$\sigma(\varphi) = \sigma_{\max} \cos\varphi \tag{2.15}$$

If a tensile load F is applied to welded sheets, the following equilibrium equations can be obtained :

$$F = \int_{-\pi/2}^{\pi/2} t \cdot \sigma(\varphi) \cdot \frac{d}{2} \cdot \cos\varphi \quad d\varphi \tag{2.16}$$

Inserting Equation 2.11 in Equation 2.12, the following can be written :

$$F = \int_{-\pi/2}^{\pi/2} t \cdot \sigma_{\max} \cdot \frac{d}{2} \cdot \cos^2\varphi \quad d\varphi = \frac{\pi \cdot t \cdot d \cdot \sigma_{\max}}{4} \tag{2.17}$$

Therefore for a given failure load F_{max}, the maximum local stress φ_{max} experienced by the material at the vicinity of the weld nugget is given as :

$$\sigma_{\max} = \frac{4F_{\max}}{\pi \cdot t \cdot d} \tag{2.18}$$

Where t is the thickness of fractured sheet and d the nugget diameter.

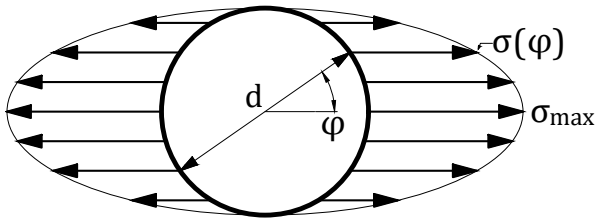

Figure 2.10 – Stress distribution around nugget for a button pullout failure mode

A robust weld results in specimen failure in button pullout mode during tensile test. Figure 2.11 shows failure load and corresponding failure modes for all specimens. For 0.8 mm mild steels specimens, half of specimens failed in interfacial mode and the other half, in button pullout mode. Similar results have been observed for 0.8 mm galvanized steel sheets. As concerning 1.8 mm mild steel, all specimens failed in button pullout mode. 1.8 mm galvanized steel sheets mainly failed in interfacial mode. From a general overview of tensile test results, it is clearly seen that an optimization of process parameters is crucially needed. Tables 2.7 and 2.8 provide a summary of the failure modes for all performed welds.

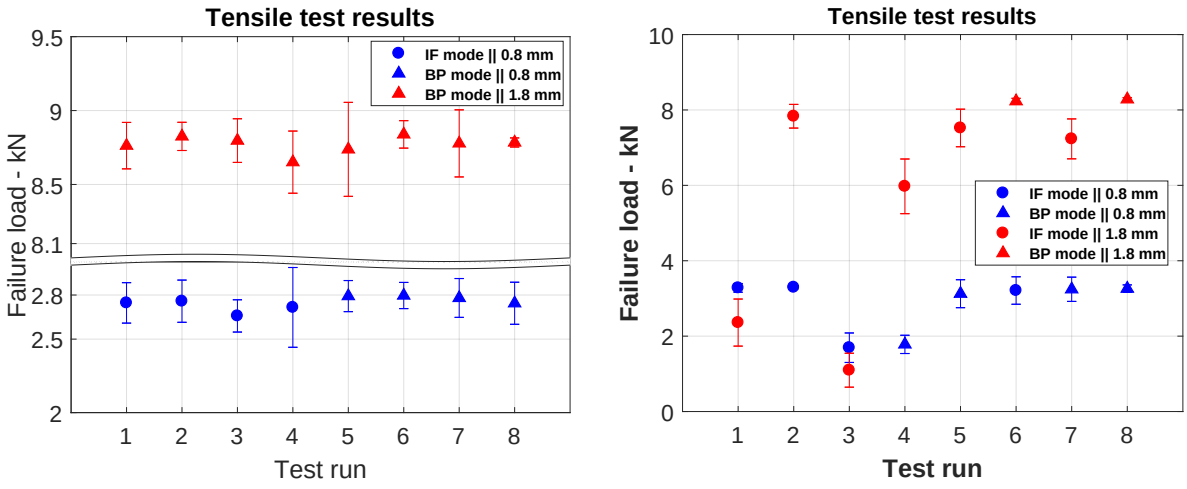

(a) A36 steel

(b) Galvanized steel

Figure 2.11 – Tensile-shear test results

2.3.3 Simultaneous multi-objective optimization of process parameters

The ultimate aim of this work is to optimize welding parameters. In short, this is about looking for parameter values that enable to achieve welds of good quality and

strength with a minimum welding energy. A weld is said to have good mechanical strength if during tensile test, failure occurs at the nugget vicinity (button pullout mode). This sine qua non condition enabled to choose optimization criteria. After analyzing various test results, a relationship between hardness to nugget area ratios and failure modes was observed. The following equations can be posed :

$$r = \frac{HV}{S} \tag{2.19}$$

$$S = \frac{\pi d^2}{4} \tag{2.20}$$

Where r is hardness to nugget surface ratio, HV is the nugget hardness in Vickers, S is the nugget surface area in mm^2, and d is the nugget diameter in mm. The following provide a brief explanation of the relationship between hardness, nugget surface and weld strength :

- Impact of hardness (HV) on weld mechanical strength : Indeed, when the hardness of the weld is very high, it means that metal has been hardened due to fast dissipation of heat. It is well known that to obtain good quality welds, martensite formation must be avoided as much as possible [47]. Therefore, in this case, welds are of lower strength because heat was not maintained during the entire welding cycle, this fact led to the formation of a large fraction of martensite in the nugget. However for a good weld, the metals have time to melt and join in the presence of necessary heat, cooling is slow and the metal has time to reconsolidate, which leads to a much lower hardness.
- Impact of nugget diameter (d) on weld mechanical strength : An increase in the nugget diameter leads to an increase in the contact surface area between sheets (S) and consequently to an increase in the mechanical strength of the welds.

Thus, the ratio of hardness to nugget surface (HV/S) is a good way to control the quality of welds. Indeed, it can be drawn that weld is all the more resistant when this ratio decreases and vice versa. Performed welds allowed to define maximum values of HV/S for which failure occurs in button pullout mode (HV/S upper limit). Thus, for each steel grade and thickness, we related hardness regression equations to nugget

surface area equations. By varying welding parameters, different HV/S values are obtained. Optimization is therefore made when minimum welding parameters lead to an HV/S ratio lower than the experimental HV/S upper limit.

2.3.3.1 Study and prediction of failure modes of specimens

2.3.3.1.1 A36 steel

Table 2.6 – Hardness to weld surface ratios and failure modes, A36 steel

	Thickness 1 – 0.80 mm				**Thickness 2 – 1.80 mm**			
	HV_{300}	$S\left(mm^2\right)$	HV/S	Failure mode	HV_{300}	$S\left(mm^2\right)$	HV/S	Failure mode
1	299	4.522	66.13	IF	261	25.505	10.23	BP
2	330	7.065	46.71	IF	287	22.891	12.54	BP
3	321	9.343	34.36	IF	312	20.418	15.28	BP
4	333	3.462	96.19	IF	269	11.940	22.53	BP
5	282	11.039	25.55	BP	206	22.891	9.00	BP
6	306	18.086	16.92	BP	251	34.195	7.34	BP
7	316	11.039	28.63	BP	320	37.374	8.56	BP
8	322	15.896	20.26	BP	303	37.374	8.11	BP

Table 2.6 makes it possible to predict failure mode according to hardness to nugget surface ratio. Translating this into a graph (Figure 2.12), it can be seen that for welds with low HV/S ratios, the corresponding failure mode is button pullout (good quality weld). The same observation is true for galvanized steel welds.

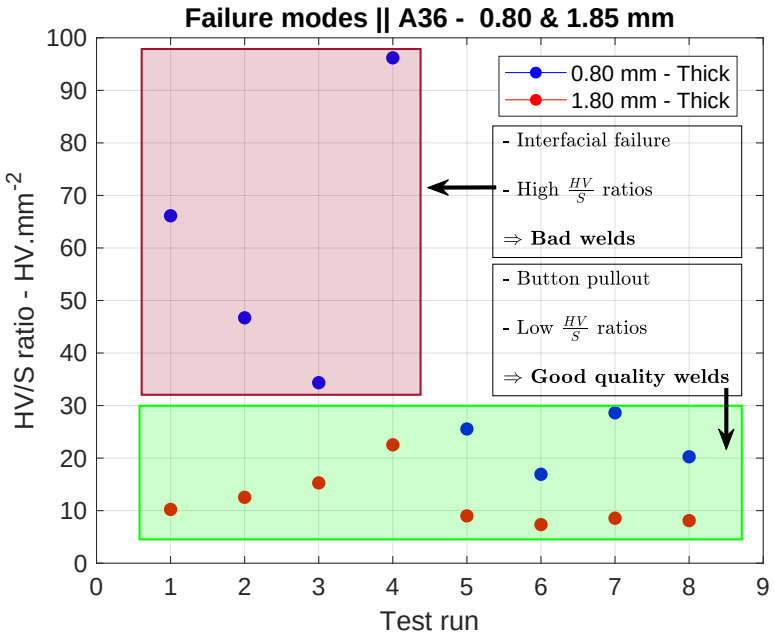

Figure 2.12 – HV/S ratios versus failure modes for A36 steel

In Figure 12, welds falling in red box experienced interfacial failure while welds in green box experienced button pullout mode. Thus, intervals that have been taken into account for the optimization of welds are as follows :

$$\text{For 0.8mm sheets,} \quad \frac{HV_{300}}{s} \leq 28.63 \tag{2.21}$$

$$\text{For 1.8mm sheets,} \quad \frac{HV_{300}}{S} \leq 22.53 \tag{2.22}$$

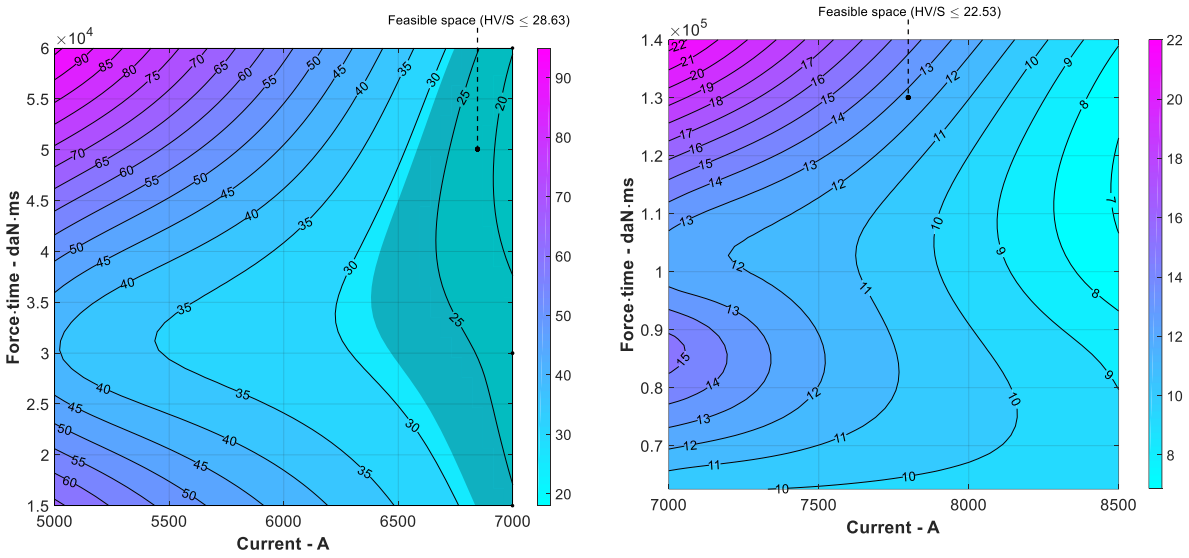

(a) 0.8 mm specimens

(b) 1.8 mm specimens

Figure 2.13 – Response surfaces I, Ft versus HV/S for A36 steel

2.3.3.1.2 Galvanized steel

For galvanized steel welds, the same study was done and obtained results were quite dissimilar to those of A36 steel. Table 2.7 enable to predict failure mode basing on hardness to nugget surface area. By translating this into a graph, we obtain failure zones.

Table 2.7 – Hardness to weld surface ratios and failure modes, galvanized steel

	Thickness 1 – 0.80 mm				**Thickness 2 – 1.80 mm**			
	HV_{300}	$S\left(mm^2\right)$	HV/S	Failure mode	HV_{300}	$S\left(mm^2\right)$	HV/S	Failure mode
1	273	24.180	11.29	IF	251	22.891	10.97	IF
2	308	19.234	16.01	IF	272	37.374	7.28	IF
3	157	16.974	9.25	IF	234	37.374	6.26	IF
4	255	29.691	8.59	BP	265	31.157	8.51	IF
5	157	18.086	8.68	BP	264	37.374	7.06	IF
6	158	15.896	9.94	IF	269	59.417	4.53	BP
7	150	47.759	5.23	BP	267	34.195	7.81	IF
8	231	67.895	3.40	BP	276	59.417	4.65	BP

The intervals that have been taken into account for the optimization of welds are as follows :

$$\text{For 0.8mm sheets,} \quad \frac{HV_{300}}{s} \leq 8.68 \tag{2.23}$$

$$\text{For 1.8mm sheets,} \quad \frac{HV_{300}}{S} \leq 4.65 \tag{2.24}$$

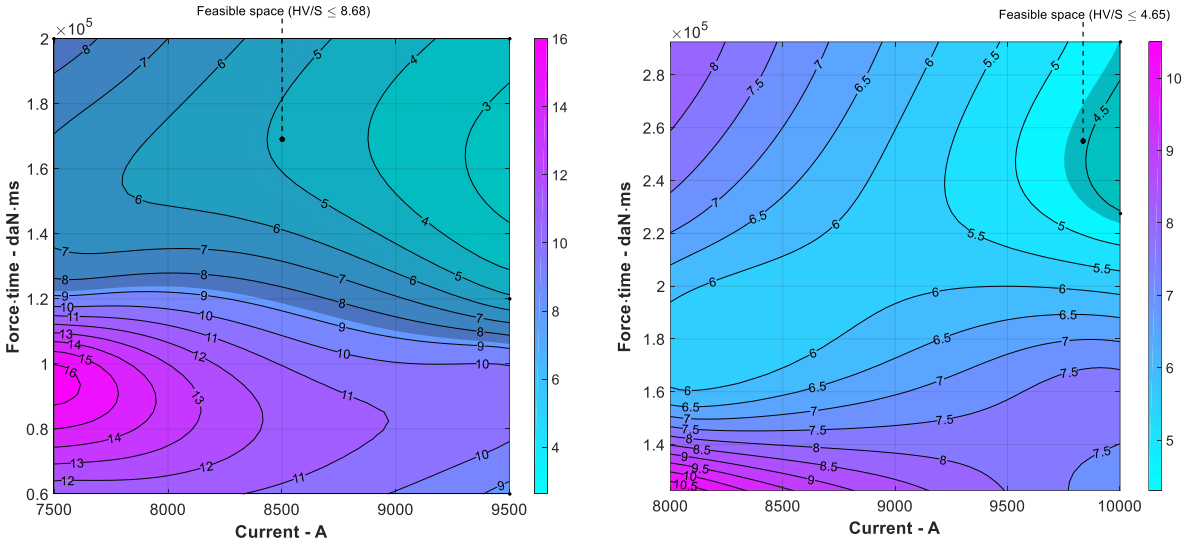

(a) 0.8 mm specimens

(b) 1.8 mm specimens

Figure 2.14 – Response surfaces I, Ft versus HV/S for galvanized steel

2.3.3.2 Setting of the algorithm

The algorithm takes into account several parameters in order to carry out the optimization with a given precision and in a reasonable time. These parameters are given in Table 2.8.

Table 2.8 – Parameter setting of the optimization algorithm

Item	Value	Observation
Population	1000	Number of solutions to be generated after each iteration (n)
Crossover probability	0.9	Crossover probability of solutions for next generations
Mutation probability	0.1	Probability of mutation for next generations
Max. number of generations	100	Regeneration limit, the algorithm stops when this number is reached
Functions to be optimized	$f_1 = I^2t$	Minimisation of welding energy
(minimisation)	$f_2 = F$	Minimisation of electrode pressing force
Constraint	$\frac{HV(I,F,t)}{S(I,F,t)} \leq R$	Condition to satisfy in order to have a good quality weld

2.3.3.3 Optimization results

The optimization application was coded on the Matlab platform according to the NSGA-II algorithm described above. Figure 2.15 shows the evolution of the optimization

according to the number of generations (case of galvanized steel, 0.8mm thick). It can be seen that the solutions to generation 1 are quite spread out, then, with the evolution of the number of generations, the solutions converge towards the optimal Pareto effective front. There is always a number of generations N_g from which the population practically no longer improves, so genetic operations no longer have a significant effect on improvement of solutions. The results obtained from this generation can thus be considered as the optimal solution. This number N_g of generation generally depends on the complexity of the objective functions, the constraints to be respected, the number of individuals in the population, and the probabilities of crossover and mutation. In the case of this work, genetic operations were found to be ineffective as from the 50th generation onwards (Figure 2.16).

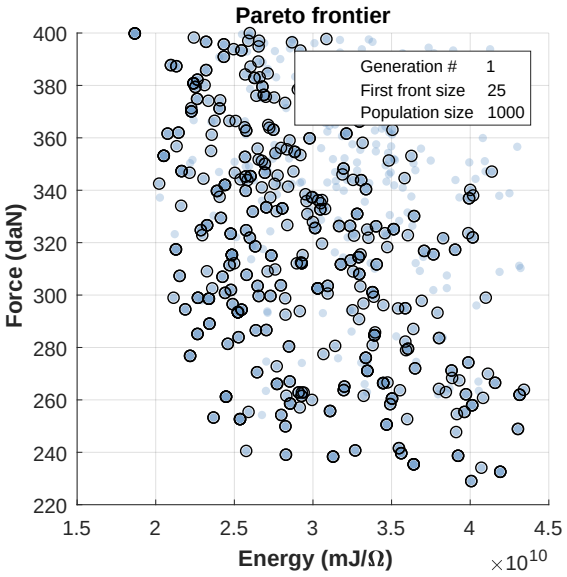

(a) 1st generation

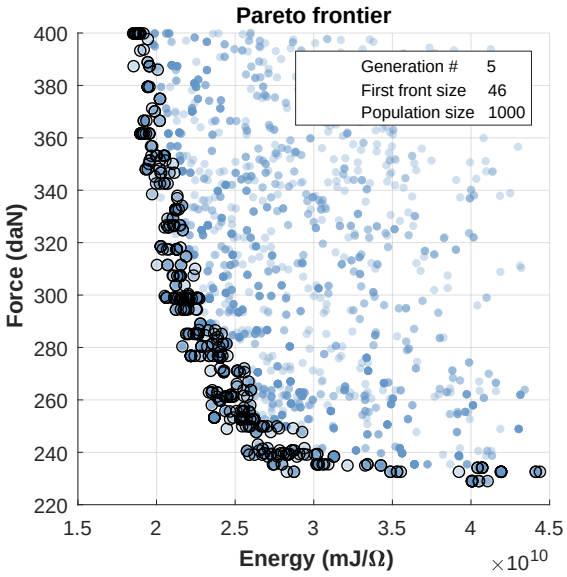

(b) 5th generation

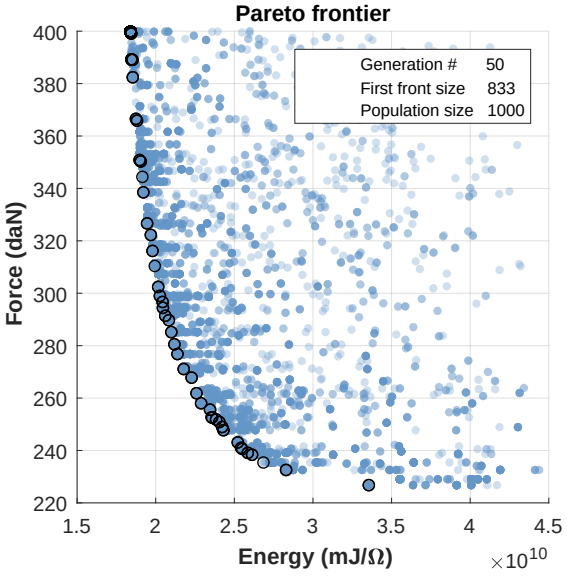

(c) 50th generation

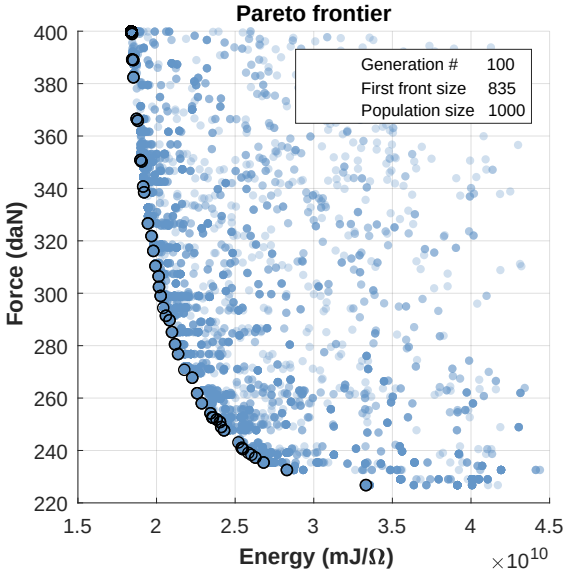

(d) 100th generation

Figure 2.15 – Evolution of solutions

Table 2.9 – Recapitulation of optimized parameters and comparison between optimized and usual parameters*

Steel grade	Thickness (mm)	Characteristics	Current (A)	Force (daN)	Time (ms)
A36 steel	0.80	Usual parameters	7000	200	300
		Optimized parameters	6507.48	193.07	150.03
		Gain	7.04%	3.46%	49.99%
	1.80	Usual parameters	8500	350	400
		Optimized parameters	7000.03	250.00	250.08
		Gain	17.65%	28.57%	37.48%
Galvanized steel	0.80	Usual parameters	9500	400	500
		Optimized parameters	7824.72	399.54	301.19
		Gain	17.63%	0.12%	39.76%
	1.80	Usual parameters	10000	450	650
		Optimized parameters	9998.55	350.00	629.10
		Gain	0.01%	22.22%	3.22%

**Usual parameters are parameters that are commonly used by companies for welding. They varies according to steel grade and gauge.*

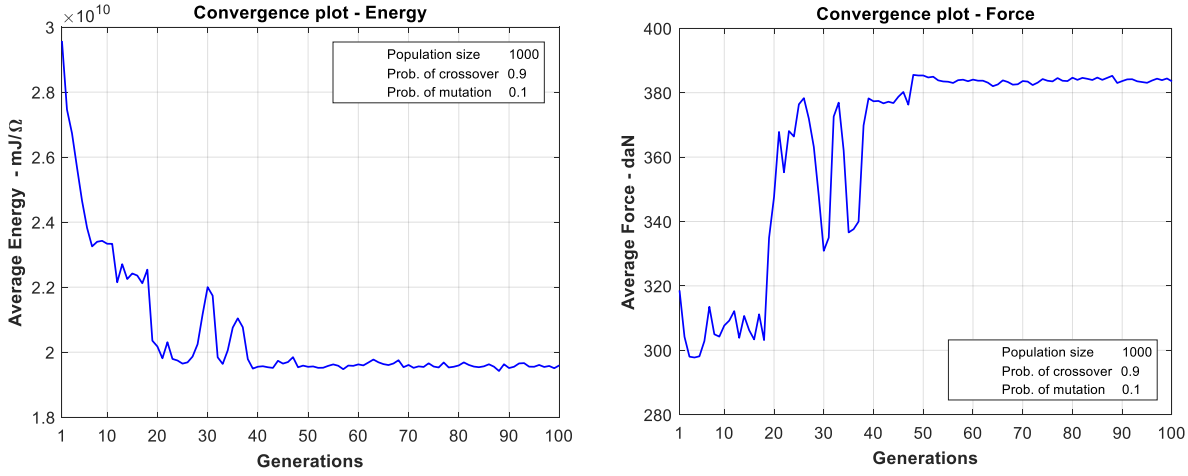

(a) Energy **(b)** Force

Figure 2.16 – Convergence graph of objective functions, case of galvanized steel, thickness 0.80 mm

Following the optimization carried out with the NSGA-II, the ideal welding parameters have been determined and are summarized in Table 2.9.

2.3.3.4 Gain due to optimization and validation of optimized parameters

In order to assess the validity of optimized parameters, tensile-shear tests were carried on both optimized and generally used parameters.

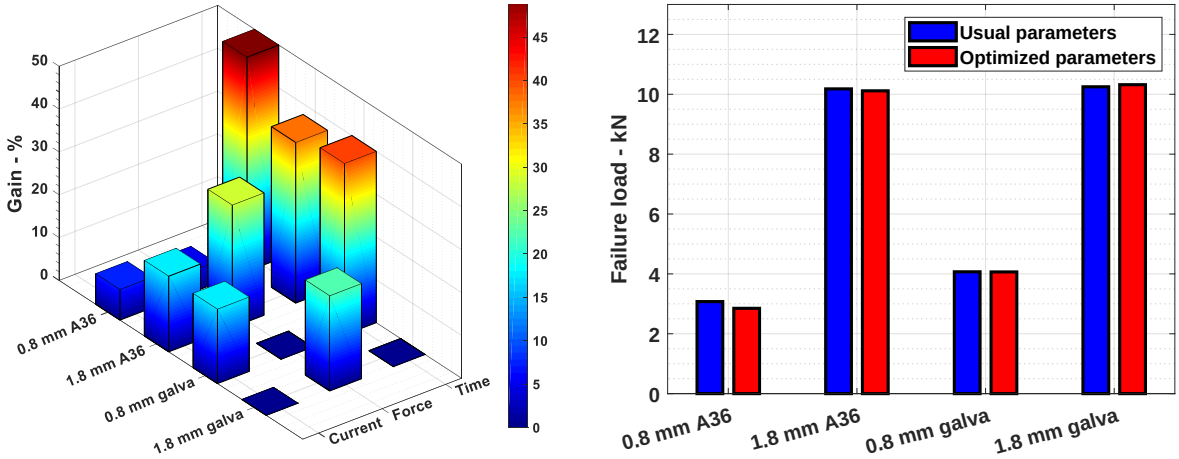

(a) Gain due to optimization

(b) Validation of optimized parameters

Figure 2.17 – Visualization of the gain in process parameters and validation of optimized process parameters

Figure 2.17.a illustrates the gain in current, force and time due to the performed optimization for both mild and galvanized steel. Current could be reduced by up to 17.65% for 1.8 mm A36 mild steel, for 1.8 mm galvanized steel, no reduction of current could be achieved, this is due to the presence of a thicker zinc layer in the faying surface of sheets. That observation is in agreement with the remark of Gedeon and Eagar [48]. As concerning the reduction in electrode pressing force, it can be observed from the same figure that it was possible to achieve important gain only for 1.8 mm sheets (both A36 mild and galvanized steel). Welding time was the parameters in which the highest gain has been exhibited, for both grades and both thicknesses, the gain in welding time was at least 37.48% at the exception of 1.8 mm galvanized steel sheets. Yet, this is because 1.8 mm galvanized steel sheets need more current and time due to the presence of a thicker zinc layer at the faying surface, a similar observation was made by Lin et al. [49]. Optimized parameters where used for welding and resulted welds where assessed through tensile tests. All these specimens passed validation tests by experiencing rupture in the base metal. Figure 2.17.b provides a comparison between tensile strength of welds obtained from usual parameters and weld obtained from optimized parameters. As failure occurred in the base metal in all cases, failure loads are very closed each other as same materials where used for both usual and optimized parameters.

2.4 Conclusion

In this work, an approach to optimize process parameters for resistance spot welding was developed. It makes it possible to obtain optimum welding parameters that lead to a minimization of production energy while ensuring the good mechanical strength of welds. The study was carried out on two steel grades, ASTM A36 mild steel and ASTM A653 hot dipped galvanized steel. The steel specimens were welded according to predefined factorial plans. Micro-indentation hardness tests revealed welds quality. Static tensile tests were done to determine the mechanical performances of welds. Based on the results of these tests, ANOVAs were conducted to determine the influence of welding parameters on the geometry and hardness of welds and to establish predictive models. The optimization of the process parameters through the NSGA-II was then carried out for both steel grades. Purely stochastic and based on genetic evolution, the proposed optimization approach is more practical than deterministic approaches because it overcomes the local optimum problem and requires less execution time. The main conclusions of this work are as follows :

- A36 mild steel showed a wider welding lobe as compared to galvanized steel.
- The welding current is the most influential parameter and contributes for about 70% to the mechanical strength of the welds.
- The optimization of process parameters results in an average decrease in welding current, electrode pressing force and welding time of 10.58%, 13.59% and 32.61% respectively.
- The use of optimized parameters leads not only to a reduction in welding energy, but also to an increase in the overall service life of the electrodes welding machines.

Chapitre 3

Modeling of Phase Transformation Kinetics in Resistance Spot Welding and Investigation of Effect of Post Weld Heat Treatment on Weld Microstructure

Metals and Materials International (Online ISSN : 2005-4149) - Springer

B. V. Feujofack Kemda[ψ,*], **N. Barka**[ψ], **M. Jahazi**[χ] **and D. Osmani**[ζ]

Sommaire

Submitted on August 03rd 2019, Accepted on September 26th 2019

https ://doi.org/10.1007/s12540-019-00486-x

**Corresponding author - E-mail address :*bleriotvincent.feujofackkemda@uqar.ca (B. V. Feujofack K.)
[ψ] *University of Quebec in Rimouski, Québec G56 3A1, Canada.*
[χ] *Ecole de Technologie Superieure, Montréal, Québec H3C 1K3, Canada.*
[ζ] *AMH Canada Ltd, Rimouski, Québec G5L 1Z2, Canada.*

Avant-propos

Auteurs et affiliations

Blériot Vincent Feujofack Kemda : Étudiant en maîtrise en ingénierie, Département de mathématiques, d'informatique et de génie, Université du Québec à Rimouski, Rimouski, Québec G56 3A1, Canada.

Noureddine Barka : Professeur, Département de mathématiques, d'informatique et de génie, Université du Québec à Rimouski, Rimouski, Québec G56 3A1, Canada.

Mohammad Jahazi : Département de génie mécanique, École de technologie supérieure, Montréal, Québec H3C 1K3, Canada.

Denis Osmani : AMH Canada Ltée, Rimouski, Québec G5L 1Z2, Canada

Titre en Français

Modélisation de la cinétique de transformation de phases lors du soudage par résistance par points et étude de l'effet du traitement thermique post-soudage sur la microstructure de la soudure.

État de l'article

Accepté et en cours de publication dans le journal : « Metals and Materials International ».
https ://doi.org/10.1007/s12540-019-00486-x

Contribution au mémoire

Cet article constitue la troisième partie de ce mémoire. Afin d'obtenir des soudures résistantes, ductiles et durables, il est crucial de comprendre le phénomène métallurgique que subit l'acier pendant le processus de soudage. La résistance mécanique d'une soudure dépend directement de sa microstructure. Ainsi, en déterminant la microstructure d'une soudure, il est possible de prévoir la résistance mécanique de celle-ci. Il est donc judicieux d'ajuster les paramètres de soudage afin d'obtenir une microstructure souhaitée et donc

une résistance souhaitée. Dans cet article, il est démontré par des outils de simulation que l'application du TTPS permet de réduire la teneur en martensite et d'augmenter la diversité de phase dans les joints soudés par résistance. Comme il est bien connu que la martensite est responsable de la fragilité des soudures, l'application du TTPS implique de ce fait une augmentation de la ductilité des soudures et de leur durée de vie globale en fatigue.

Résumé en Français

Ces dernières années, l'utilisation d'aciers biphasés (DP), d'aciers à transformation induite par plasticité (TRIP) et d'aciers au bore pour certaines parties des carrosseries automobiles est devenue une nécessité en raison de leur résistance et de leur poids léger. Le soudage par résistance par points étant un procédé dans lequel l'acier est chauffé et refroidi en très peu de temps, le noeud de soudure résultant est généralement entièrement martensitique, en particulier dans le cas des aciers DP, TRIP et au bore mais cela est également valable pour les aciers ordinaires au carbone comme l'AISI 1010, qui est largement utilisé pour les parties internes des carrosseries automobiles. La martensite à son tour doit être évitée autant que possible lors du soudage de l'acier, car elle est la principale source de fragilité. Ainsi, ce travail vise à trouver un moyen de réduire la fraction de martensite et d'augmenter la diversité des phases dans le noeud de soudure. La prédiction de la transformation de phase pendant SRP a été faite. Des simulations ont été réalisées sur des feuilles de 2 mm d'AISI 1010 et les résultats montrent que l'application d'un traitement thermique post-soudage permet de réduire la fraction de martensite et conduit à la formation de ferrite et de bainite dans le joint soudé. Des expériences de soudage ont été effectuées en parallèle et la géométrie expérimentale des noeuds de soudure est en accord avec les résultats de la simulation.

Abstract

In recent years, the usage of dual phase (DP) steels, transformation induced plasticity (TRIP) steels and boron steels in some auto body parts has become a necessity because of their strength and lightweight. Resistance spot welding (RSW) being a process were steel is heated and cooled in a very short period of time, the resulting weld nugget is generally fully martensitic, especially in the case of DP, TRIP and boron steels but that also holds for plain carbon steels as AISI 1010 grade which is extensively use in auto body inner parts. Martensite in is turn must be avoided as much as possible when welding steel because it is the principal source of brittleness. Thus, this work aims in finding a mean to reduce martensite fraction and increase phase diversity in weld nugget. The prediction of phase transformation during RSW has been done. Simulations have been performed for 2 mm AISI 1010 sheets and results show that the application of post weld heat treatment leads to the reduction of martensite fraction, and formation of ferrite and bainite in the nugget. Welding experiments have been done in parallel and experimental weld nugget geometry is in good agreement with simulation results.

Keywords : Resistance spot welding ; AISI 1010 ; Modeling ; Post weld heat treatment ; Phase transformation ; Kinetics

3.1 Introduction

Resistance spot welding (RSW) is one of the predominant sheets joining process in automotive industry [50, 51]. A typical modern car body has about 5000 spot welds [52, 53] and can have up to 12000 spots according to the size of the car [54]. This joining process is very fast and highly adaptable to automation for high rate productions [55, 56], what can explain the great interest of factories to it. The principle of RSW is to firmly hold two or more steel sheets and send a high rate current through them. Due to high electrical resistance of steel sheets, these lasts will heat up and melt . The RSW process it usually consisted of four stages [57, 58], the first step is the squeeze time, this is the time through which force is applied to metal sheets. It's followed by welding cycle, here the welding current is applied. After the current has been applied, there is what we call the holding step, in this step, no more current is passing through the system but the pressure of electrodes is still present to enable the melted metal to settle. Once the weld is consolidated, electrodes are released. AISI 1010 is a low-carbon alloy appropriate in sheet and strips for deep drawing, carburized and structural applications. AISI 1010 is ideal for the automobile industry, where it is frequently used for interior auto body parts, fenders, and smaller parts including pans and transmission covers, where the interest of this steel grade for the present study. The overall process of a spot weld usually last for around 300 ms, which implies fast cooling rates. In RSW, the cooling rate is particularly very high, due to the transient phenomena and the flowing of cooling water inside electrodes [59] . To effectively understand the microstructure evolution and the mechanical behavior of welds, it is primordial to master the heat process of welding [60, 61]. Gould and al. [32] predicted the microstructures evolution when welding automotive advanced high-strength steels, the included several welding processes in their studies, among which, laser beam welding (LBW) and RSW. The observed from their calculation that RSW is the one that leads to highest cooling rates, these rates ranged from 100000°C/s for sheets less than 0.5 mm thick to roughly 2000°C/s for sheets of 2 mm thick. While LBW exhibited cooling rates ranging from 200 to 5000°C/s. Such cooling rates generally lead to the formation of martensite in both fusion zones

and HAZ. It is well known that in order to obtain mechanically strong welds, it is imperative to prevent at the extent of possible, the martensite formation during welding [47, 62]. Taking a loop on continuous cooling transformation (CCT) diagram of AISI 1010, it is obvious that a spot welding will lead to martensite formation in the overall weld zone. Untempered martensite resulting from welding process is generally hard and brittle, in opposite to the base metal which is generally soft and ductile. That duality leads to a fracture in base metal during static loading tensile tests, and to a fracture in the weld nugget, which is brittle during fatigue tensile tests. Cars are generally solicited in fatigue loading, that fact makes engineers to put in place methods and procedures to avoid martensite formation during welding. In order to reduce residual stresses and to improve resistance to brittle fracture, a wise technique called post weld-heat treatment (PWHT) is generally used [63]. From literature, it appears that only few works have been done regarding post heat treatment in spot welding. Jahandideh et al. [64] studied the effects of post heating time (PHT) and post heating current (PHC) on weld quality of SAPH440 in RSW. They come into conclusion that the application of Post heating time and post heating current highly contribute to the elimination of interfacial failure mode of welds. They further observed that there are optimum values of PHT and PHC to achieve good results, below these optimum values, there is no effect, and above these values, the heat is high enough to generate a quench of steel after the post heating treatment. Chuko and Gould [65] developed an appropriate resistance spot welding practice for transformation-hardened steels. They found that applying in-situ tempering in RSW resulted in a decrease of hardness of the weld zone. They then designed tempering diagram of high-strength steel (HSS) during spot welding, these diagrams aim in helping manufacturers to choose right tempering parameters in order to achieve a certain desired hardness. Khan et al. [66] studied the effect of varying the current of the second pulse of a RSW schedule on the microstructure and mechanical properties of DP600 advanced high strength steel sheets. They used both simulation and laboratory experiments in their work. They found that varying the second pulse current could alter heat cycle and thus cooling time. They further recommended the use of numerical simulation to optimize current schedule in RSW in order to achieve best thermal cycles.

Lane et al. [67] analyzed the effect of pre-weld and post-weld current modification on nugget quality in RSW of galvanized steel sheets. They mainly found that preheat current enable to achieve uniform nugget initiation while post weld current helps to suppress expulsions. Arabi et al. [68] used the effect of in-situ controlling of thermal cycle during resistance spot welding as a tool for weld microstructure modification, in order to improve the phase balance in the fusion zone of the 2304 duplex stainless steel resistance spot welds. They found that it was possible to achieve a homogeneous microstructure with an improved phase balance via in-situ post weld heat treatment. Hernandez et al. [69] found that the fusion zone (FZ) microstructure and the mechanical behavior of resistance spot welded TRIP steel could be successfully modified by applying local post-weld heat treatments by second pulse currents. From their experiments, the concluded that medium post heat currents (7kA) mainly lead to an increase of lap shear-tensile strength of welds, low post heat currents (5 kA) mainly lead to the tempering of martensite in the fusion zone while high post heat currents (9kA) lead to the re-melting and further, to the quenching fusion zone.

With recent advances in computer science, phase transformation kinetics during heating and cooling processes have been made possible. To model phase transformation kinetics in RSW, it is essential to model the physical phenomenon of welding itself. Many works have been done in the field of modelling RSW process. Huh and Kang [54] were among the pioneers in modelling this welding process. They did an electro thermal analysis of RSW process by a 3-D finite element method, the analysis they did was based on electrical and thermal phenomena. The aim of their simulation was to find the effect of electrodes ellipticities on nugget size. They found that circular-shaped electrodes could produce larger nuggets as compared to elliptical-shaped ones but were unfavorable in the case of stress concentration. Nielsen et al. [70] took into account the mechanical phenomenon in 3-D simulations of resistance spot welding. They found the effect of electrode misalignment of nugget geometry; shunt effect was also put into evidence. They ended by simulation of tensile-shear tests and got results that were very closed to experimental values, showing the reliability of their model. Jafari et al. [71] simulated the shunting effect in RSW of Al2219 sheets, their results highlighted the

effect of shunting distance on nugget diameter and segregation of alloying elements. As regarding simulation of phase transformation kinetics, Venkatraman et al. [72] modeled transformation kinetics in HSLA 100 steel during continuous cooling through CCT approximation of Avrami's isothermal model. Though their model predicted a delayed transformation of austenite, final transformed fraction was found to be in good agreement with experimental value they obtained. Scheil's additivity rule is usually adopted to describe a non-isothermal transformation behavior [73] and is the basis of a lot of works in the field of phase transformation modelling. Oliveira et al [74] phase transformation during quenching of steel using a constitutive model with diffusional and no-diffusional phase transformation. Their simulated results highlighted the effect of water and air-cooling on phase distribution and these results were in good agreement with experimental data. Piekarska et al. [75] modeled phase transformation in welded joints using CCT diagrams, in their analyses, they highlighted and evaluated the effect of heating rates on the austenization temperature and further, on the phase transformation kinetics. Some works have been done on the modelling of cooling curves, it is the case of Trzaska and Dobrzanski [76] who modelled CCT diagrams for engineering and constructional steels using neural networks and regression method for the relationship between chemical composition and austenizing temperature during continuous cooling.

In the present work, an electro-thermo-mechanical model for simulation of RSW is implemented. From temperature evolution, a phase transformation model based on Avrami equation and Scheil's additivity rule is used to determine phase constitution in the weld nugget throughout the welding process. In a second step, the PWHT technique is used in the model in order to reduce cooling rate in the metal and subsequently, to attenuate martensite formation in the weld nugget.

3.2 Materials and methods

3.2.1 Finite elements modeling and analysis

3.2.1.1 Mathematical definition of electro-thermo-mechanical phenomenon

3.2.1.1.1 Electrical module

At a macroscopic level, the electromagnetic analysis in RSW can be done through the solving of Maxwell's equations for time varying fields [77]. The part of Maxwell's equations involved in Joule heating can be written as follows [78] :

$$\nabla \times H = J + \frac{\partial D}{\partial t} \tag{3.1}$$

$$\nabla \cdot D = \rho_v \tag{3.2}$$

Where H is the magnetic field intensity, J is the current density, D is the electric flux density, and ρ_v is the electric charge density. The first equation refers to Maxwell-Ampère's law and the second refers to Gauss' law in electric form. The divergence of both sides of Equation 3.1 leads to :

$$\nabla \cdot (\nabla \times H) = \nabla \cdot J + \frac{\partial (\nabla \cdot D)}{\partial t} \tag{3.3}$$

As the divergence of the curl is identically zero, Equation 3.3 reduces to the following, also known as continuity equation [78] :

$$\nabla \cdot J = -\frac{\partial \rho_v}{\partial t} \tag{3.4}$$

In order to obtain a closed system, the equations must include constitutive relations that describe the macroscopic properties of the medium. There exists a proportionality between D and E for linear isotropic materials. The constant of proportionality in this case is the permittivity ε. If the material is nondispersive, the consecutive relation takes the following form [79] :

$$D = \varepsilon E \tag{3.5}$$

Generally, the permittivity is referenced to the permittivity of free space and the constitutive relation then reduces to :

$$D = \varepsilon_r \varepsilon_0 E \tag{3.6}$$

ε_γ and ε_0 being respectively the relative permittivity and the permittivity of free space. In a stationary coordinate system, a more general form of Ohm's law reads [77] :

$$J = \sigma E + J_e \tag{3.7}$$

Where Je is an externally generated current density. However, in the case of RSW that value is often null. In any conducting material, the electric field is governed by the Maxwell's equation of conservation of charge. For steady state current, that equation reduces to :

$$\int_A -J \cdot n dA = I \tag{3.8}$$

Where A is the cross-sectional area passed by electric current and n is the outward normal vector to A. A consequence in Maxwell equation is that the changes of the fields are always delayed relative to the changes of the sources, reflecting the finite speed of propagation of electromagnetic waves. Assuming that this effect can be ignored, it is then possible to obtain electromagnetic fields by considering stationary currents at every instant. This is the so used "Quasi-static approximation." This approximation remains valid as long as the variations in time are small and the studied geometry is substantially smaller than the wavelength [80]. The quasi-static assumption implies that the electric flux density vector can be ignored and thus, $\frac{\partial D}{\partial t} = 0$ [81]. Considering all the assumptions made previously, the governing equations that describe the electromagnetic phenomenon in RSW can be written as follows :

$$\nabla \times H = J \tag{3.9}$$

$$J = \sigma E = -\sigma \cdot \nabla \varphi \tag{3.10}$$

$$\nabla \cdot J = 0 \tag{3.11}$$

Combining Equations 3.10 and 3.11, the following Quasi-Laplace equation governing the voltage potential, can be written in the rectangular coordinates as is obtained :

$$\frac{\partial}{\partial x}\left[\sigma \cdot \frac{\partial \varphi}{\partial x}\right] + \frac{\partial}{\partial y}\left[\sigma \cdot \frac{\partial \varphi}{\partial y}\right] + \frac{\partial}{\partial z}\left[\sigma \cdot \frac{\partial \varphi}{\partial z}\right] = 0 \tag{3.12}$$

With σ being the temperature dependent electrical conductivity, φ is the electrical potential.

Table 3.1 – Electrical boundary conditions

Item	**Boundary condition expression**
Electrode sheet interface [82]	$\frac{1}{\rho} \cdot \frac{\partial \varphi}{\partial z} = \frac{1}{\rho_{ES}} (\varphi_E - \varphi) *$ (3.13)
Faying surface [82]	$\frac{1}{\rho} \cdot \frac{\partial \varphi}{\partial z} = \frac{1}{\rho_{SS}} (\Delta\varphi_{SS}) **$ (3.14)
Surface exposed to ambient	$\frac{1}{\rho} \cdot \frac{\partial \varphi}{\partial z} = 0$ (3.15)

* Where ρ is the bulk temperature dependent electrical resistivity, ρ_{ES} is the electrical contact resistivity between electrode and sheet, and φ_E is the voltage applied to the electrodes.

** ρ_{SS} is the electrical contact resistivity at the sheets faying surface and $\Delta\varphi_{SS}$ is the voltage drop between sheets.

In RSW, electrical contact resistivity depends on several parameters such as electrode force, mechanical, electrical and thermal properties of metals [83]. The following equation is generally used to calculate electrical contact resistivity [84, 85]

$$\rho_c(T) = R_c(20°C) \frac{A_c}{L_c} \sqrt{\frac{\sigma_{e,ave}(T)}{\sigma_{e,ave}(20°C)}} \tag{3.16}$$

$$L_c = 2 \times 10^{-5} \tag{3.17}$$

Where $R_c(20°C)$ is the measured electrical contact resistance of sheet-electrode interface at 20°C under constant mechanical stress.

3.2.1.1.2 Thermal module

In RSW, heating power per unit of volume due to Joule effect can be calculated as follows [86] :

$$Q = JE = \sigma |E|^2 \tag{3.18}$$

$$Q = \sigma |\nabla \varphi|^2 \tag{3.19}$$

The governing equation of heat transfer is stated as follows :

$$\frac{\partial}{\partial x_i}\left(k_{ij}\frac{\partial T}{\partial x_j}\right) + Q = D \cdot c \cdot \frac{\partial T}{\partial t} \tag{3.20}$$

Combining Equations 3.19 and 3.20, heat transfer equation written in rectangular coordinates is reduced to the following :

$$D \cdot c \cdot \frac{\partial T}{\partial t} = \frac{\partial}{\partial x}\left[k \cdot \frac{\partial T}{\partial x}\right] + \frac{\partial}{\partial y}\left[k \cdot \frac{\partial T}{\partial y}\right] + \frac{\partial}{\partial z}\left[k \cdot \frac{\partial T}{\partial z}\right] + \sigma \nabla \varphi \cdot \nabla \varphi \tag{3.21}$$

Where D is mass density, c is specific heat capacity, k is thermal conductivity coefficient, and T is temperature. Specific heat capacity at melting temperature is given by [14] :

$$\bar{C} = C + \frac{L}{T_L - T_S} \tag{3.22}$$

Where C is the solid-state specific heat capacity, L is latent heat, T_S is solidus temperature, and T_L is liquidus temperature.

Table 3.2 – Thermal boundary conditions

Item	Boundary condition expression
Contact surface of electrode and sheet [82]	$-k_{ES}\frac{\partial T}{\partial z} = \frac{1}{\rho_{ES}}(\varphi - \varphi_e)^2 * (3.23)$
Faying surface [82]	$-k_{SS}\frac{\partial T}{\partial z} = \frac{1}{\rho_{SS}}(\Delta\varphi)^2 * (3.24)$
Inner electrode surface [71]	$-k_E\frac{\partial T}{\partial z} = h_W(T - T_W) * (3.25)$
Sheet exposed to ambient [71]	$-k\frac{\partial T}{\partial z} = h_A(T - T_A) * (3.26)$
Unspecified surfaces [71]	$\frac{\partial T}{\partial n} = 0 * (3.27)$

* k_{ES} is the temperature thermal coefficient at sheet-electrode interface, k_{SS} is the temperature thermal coefficient at sheets faying surface, k_E is the electrode thermal conductivity coefficient. T_W and T_A are water and air ambient temperatures, h_W and h are water and air thermal convection coefficients, and n is the considered surface normal vector. The thermal contact conductivity between two faying surfaces is given by the following :

$$k_c = \frac{1}{3}\left(\frac{\sigma}{\sigma_e}\right)\left(\frac{k_1 + k_2}{2}\right) \tag{3.28}$$

Where σ is the average normal stress, σ_e is the average yield stress, k_1 and k_2 are temperature thermal coefficients of contacting parts.

3.2.1.1.3 Solid mechanics module

The mechanical module enables to consider interface contacts and to calculate strain of steel during the welding process. This module takes uses temperature-dependent properties of materials. The governing equations for a general continuum are the linear momentum equations, constitutive equation that relates stress to strain, and kinematic equation relating strain to displacement.

Linear momentum equations : Newton's second law is used for the balance of

linear momentum, which in direct tensor form reads [87] :

$$\nabla \cdot \sigma + F_V = D\frac{\partial^2 u}{\partial t^2} \tag{3.29}$$

Where σ is the Cauchy stress tensor, F_V is the body load as force per unit volume, D is the material density, u is the displacement vector and the time is denoted by t.

Stress-Strain Relationship : For large strains and hyper-elastic materials, there are several stress scales, the stresses are related to each other as [88] :

$$S = F^{-1}P \tag{3.30}$$

$$\sigma = J^{-1}PF^T = J^{-1}FSF^T \tag{3.31}$$

Where is the Cauchy stress, defined as the force divided by deformed area in fixed directions. P is the first Piola-Kirchhoff stress tensor, which is asymmetric and is used only for hyperelastic material models. S is the second Piola-Kirchhoff stress, which is same as Cauchy stress but following the body. The constitutive equation relating the stress to strain is the Hooke's law [89],

$$\sigma = C \cdot \varepsilon \tag{3.32}$$

Where C is the elasticity tensor, and ε the strain. In COMSOL, this relation is defined as follows :

$$S - S_0 = C : (\varepsilon - \varepsilon_0 - \varepsilon_{\text{inel}}) \tag{3.33}$$

Where S_0 and ε_0 are respectively initial stress and strain in the material, : denotes double dot tensor product and ε_{inel} is the inelastic strain.

Plasticity : In RSW, weld zone is generally highly solicited, over the steel yield stress, which results in strain hardening due to dislocations in the metal. There are several ways to model strain hardening of metals, including kinematic and isotropic ways. The isotropic models are mostly used in industrial metal working application as they are able to predict the hardening behavior of a wide range of materials [90]. Isotropic hardening was taken

into account in this study through the following the Hollomon model [91] :

$$\sigma_p = K\left(\varepsilon_p\right)^n \tag{3.34}$$

Where σ_p and ε_p are respectivelely strain and strain in the plastic region. K is the strength coefficient and n is the strain-hardening (or work-hardening) exponent, they both vary from alloy to alloy. For mild steels, $K = 530MPa$ and $n = 0.26$ while for annealed copper, $K = 315MPa$ and $n = 0.54$ [92].

Strain-Displacement Relationship : Let F being the strain gradient, F contains all information about local straining and rotation of the material. In terms of displacement gradient, F can be written as :

$$F = \nabla u + I \tag{3.35}$$

The ratio between the initial and the final volume reads,

$$\frac{dV}{dV_0} = \frac{\rho_0}{\rho} = \det(F) = J \tag{3.36}$$

The right Cauchy-Green strain tensor reads [93] :

$$C = F^T F = (\nabla u)^T + \nabla u + (\nabla u)^T \nabla u + I \tag{3.37}$$

Then, the Green-Lagrange strain tensor reads [88] :

$$\varepsilon = \frac{1}{2}(C - I) = \frac{1}{2}\left((\nabla u)^T + \nabla u + (\nabla u)^T \nabla u\right) \tag{3.38}$$

3.2.1.2 Mathematical definition of metallurgical phenomenon

3.2.1.2.1 Phase transformation kinetics of austenite into ferrite, pearlite and bainite

Under isothermal transformations, phase kinetics in steel can be modelled by the well-known Johnson-Mehl-Avrami-Kolmogorov (JMAK) equation [74, 94],

$$f_k = f_{k,\max}\left[1 - \exp\left(-b_k t^{n_k}\right)\right] \tag{3.39}$$

Where f_k is the volume fraction of the k phase at constant temperature T and at the time t , $f_{(k,max)}$ is the maximum volume fraction of the phase k, n_k is the Avrami exponent and b_k is a factor that characterizes nucleation and growth processes [74] . Assuming that transformation to $k-phase$ is started when $f_{k_{start}} = 0.01$ and is finished when $f_{k_{finish}} = 0.99$, factors n_k and b_k can be calculated as follows [95] :

$$b_k(T) = -\frac{\ln\left(f_{k_{\text{start}}}\right)}{(t_s)^{n_k(T)}} \tag{3.40}$$

$$n_k(T) = -\frac{\ln\left(\ln\left(f_{k_{\text{start}}}\right)/\ln\left(f_{k_{\text{finish}}}\right)\right)}{\ln\left(t_s/t_f\right)} \tag{3.41}$$

At this level, Equation 3.39 remains valid only for isothermal transformations. The prediction of non-isothermal transformation phase kinetics can be inferred by using several techniques inline with the previous JMAK equation. These techniques include additivity rules, rate model, etc. [96] Up to now, it appears that Scheil's additivity rule is the best technique for calculating the incubation period for continuous cooling from TTT so far [96]. According to the additivity rule, the total time needed to reach a certain fraction under continuous cooling can be obtained by adding the fractions of time required to reach the same fraction in an isothermal increment until the sum becomes unity. The previous stated Scheil's additivity reads [97] :

$$\int_0^t \frac{dt}{\tau[T(t), F(t)]} = 1 \tag{3.42}$$

Where $\tau(\mathrm{T},\mathrm{F})$ is the time required for the fraction F to transform isothermally, it is commonly named virtual time. Figure 3.1.a shows the discretization of continuous transformation in a sequence of isothermal transformation. In order to consider temperature variation from step T to step $T+DT$ during the transformation of t to $t+dt$, a notion of fictitious time is introduced. The fictitious time t^* is the time for the formation of the fraction f_k at temperature T, considering an isothermal transformation at temperature $T+DT$ (Figure 3.1.b).

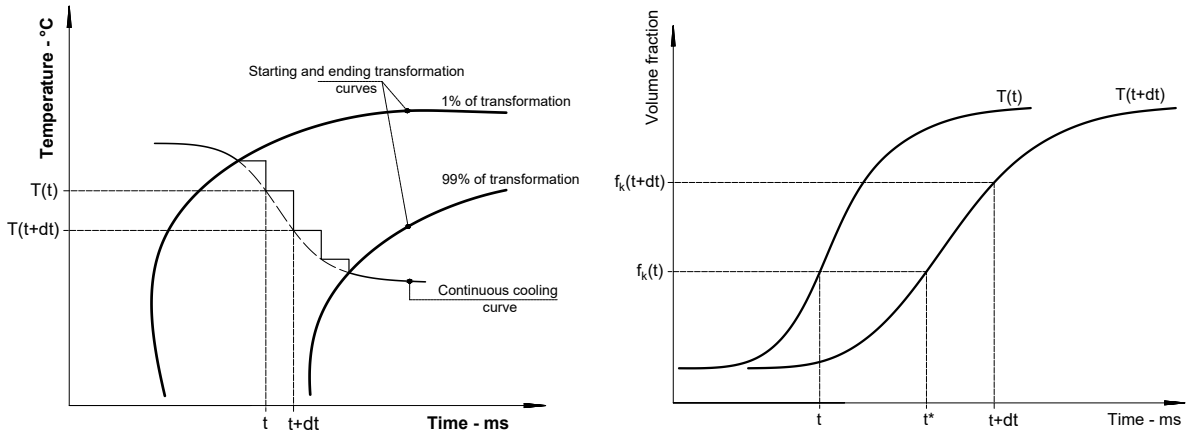

(a) Discretization of a continuous cooling curve

(b) Fictitious time

Figure 3.1 – Principle of additivity

Considering the notion of fictitious time and applying JMAK equation to an isothermal transformation from t to $t+dt$, one can write :

$$f_k(T) = f_{k,\max}(T+\Delta T)\cdot\left[1-\exp\left[-b_k(T+\Delta T)\cdot[t^*]^{n_k(T+\Delta T)}\right]\right] \tag{3.43}$$

$$\Rightarrow t^* = \left[-\frac{1}{b_k(T+\Delta T)}\ln\left(1-\frac{f_m(T)}{f_m(T+\Delta T)}\right)\right]^{\frac{1}{n_k(T+\Delta T)}} \tag{3.44}$$

In an isothermal time step dt, the volume of transformed phase at temperature $T+DT$ can be calculated using the fictitious time t^* as the starting point :

$$f_k(T+\Delta T) = f_{k,\max}(T+\Delta T)\cdot\left[1-\exp\left[-b_k(T+\Delta T)\cdot[t^*+\Delta t]^{n_k(T+\Delta T)}\right]\right] \tag{3.45}$$

Phase transformation kinetics of austenite into martensite By taking into account the thermodynamic driving force for steels, martensite fraction can be obtained through the Koistinen-Marburger model [98, 99] :

$$f_m = f_a\left(1-\exp^{-k(M_s-T)}\right) \tag{3.46}$$

Where f_a is the initial austenite fraction, M_s is the temperature at which martensite transformation starts. Assuming that martensite fraction is 99% at M_f (martensite finish

temperature), the factor k reads [74] :

$$k = \frac{\ln(0.01)}{M_s - M_f} \tag{3.47}$$

In this study, a diagram-based approach has been used for phase kinetics prediction. The CCT diagram of AISI 1010 steel was carefully drawn using the data from literature, namely the ASM Atlas of time-temperature diagrams for irons and steels [100]. With the CCT diagram, it becomes more evident to get maximum phase fraction of ferrite, pearlite and bainite in function of the cooling rate. Cooling curves where obtained from the electro-thermo-mechanical solver and were introduced in the phase kinetics transformation solver in order to get the various phase fractions as function of time.

3.2.1.3 Material properties

Several material properties vary significantly, as temperature in the material varies, in order to consider these variations, several properties have been defined as functions of temperature. The following gives enough detail on analytic expression of AISI 1010 mild steel and CuZr-C15000 zirconium copper electrode.

Table 3.3 – Electro-thermal properties of AISI 1010

Item	**Boundary condition expression**	**Temperature range** [°K]
Av. Coef. of lin. thermal exp. $(1/K)$ [101]	$\alpha(T) = \left(-4.2763 \times 10^{-6} T^2 + 9.1909 \times 10^{-3} T + 9.8890\right) \times 10^{-6}$(3.48)	273.15 ≤ T ≤ 1273.15
Specific heat capacity $(J/kg \cdot K)$ [101]	c(T)=-6.9644 $\times 10^{-7} T^3 + 5.1860 \times 10^{-4} T^2 + 1.0268T + 110.3634$(3.49)	273.15 ≤ T ≤ 1273.15
Electrical resistivity $(\Omega \cdot m)$ [101]	$\rho(T) = \left(\frac{1102}{159.4140 e^{-6.1076 \times 10^{-3} T} + 1} + 142\right) \times 10^{-9}$(3.50)	T ≥ 273.15
Thermal conductivity $(W/m \cdot K)$ [101]	k(T)=$1.8420^{-4.2805 \times 10^{-3}(T - 1617.3909)} + 30$(3.51)	T ≥ 273.15

3.2.1.3.1 Physico-mechanical properties of AISI 1010

Density of steel $\left(kg/m^3\right)$

The density of steel can be modelled with the following formulae : [102, 103]

$$\begin{aligned} D(T) = & \rho_{0^\circ} c \left(1 - \beta_V \cdot T\right) \\ & (\mathrm{T} \geq 273.15^\circ\mathrm{K}) \end{aligned} \tag{3.52}$$

With β_V being the volume expansion coefficient and ${\rho_0}^\circ C$ being the material density at 273.15°K. β_V can be calculated as follows [102] :

$$\beta_V = \alpha_1 + \alpha_2 + \alpha_3 \tag{3.53}$$

With $\alpha_{1,2,3}$ being the coefficients of linear expansion along the main axes. As the material studied is a cubic metal, the volume expansion coefficient is $\beta_V = 3\alpha_1$.

Elasticity modulus (GPa) [104]

$$E(T) = \left(-3.6946 \times 10^{-8} T^3 + 2.4662 \times 10^{-5} T^2 - 0.0189T + 100.8840\right) \frac{E\,(20^\circ C)}{100} \tag{3.54}$$

With $E\,(20^\circ C) \approx 205GPa$ [105] being the yield strength of mild steels at room temperature. We can therefore write :

$$E(T) = -7.5739 \times 10^{-8} T^3 + 5.0558 \times 10^{-5} T^2 - 0.0387T + 206.8122 \tag{3.55}$$

$$(273.15^\circ \text{K} \leq \text{T} \leq 1273.15^\circ \text{K})$$

Yield strength of steel (MPa) [106]

$$\sigma_e(T) = \left(-4.3998 \times 10^{-8} T^3 + 2.8860 \times 10^{-5} T^2 - 0.0411T + 105.1162\right) \frac{\sigma_e\,(20^\circ C)}{100} \tag{3.56}$$

$\sigma_e\,(20^\circ C) = 210MPa$ [101], being the yield strength of AISI 1010 at room temperature. We can therefore write :

$$\sigma_e(T) = -9.2396 \times 10^{-8} T^3 + 6.0605 \times 10^{-5} T^2 - 8.6226 \times 10^{-2} T + 220.7441 \tag{3.57}$$

$$(273.15^\circ \text{K} \leq \text{T} \leq 1273.15^\circ \text{K})$$

Table 3.4 – Properties of welding electrodes (CuZr-C15000)

Item	Boundary condition expression	Temperature range [°K]
Av. Coef. of lin. thermal exp. $(1/K)$ [71]	$\alpha_{El}(T) = \left(-3 \times 10^{-6} T^2 + 0.0013T + 15.934\right) \times 10^{-6}$(3.58)	273.15 ≤ T ≤ 1273.15
Specific heat capacity $(J/kg \cdot K)$ [71]	$c_{El}(T) = 8 \times 10^{-5} T^2 + 0.0726T + 369.7$(3.59)	273.15 ≤ T ≤ 1273.15
Electrical resistivity $(\Omega \cdot m)$ [71]	$k_{El}(T) = -2 \times 10^{-5} T^2 - 0.1147t + 424.89$(3.60)	T ≥ 273.15
Thermal conductivity $(W/m \cdot K)$ [71]	$k_{El}(T) = -2 \times 10^{-5} T^2 - 0.1147t + 424.89$(3.61)	273.15 ≤ T ≤ 1773.15
Elasticity modulus (GPa) [71]	$E_{El}(T) = 10^{-7} T^3 - 0.0002T^2 - 0.0516T + 150.81$(3.62)	273.15 ≤ T ≤ 1273.15
Yield strength (MPa) [71]	$\sigma_{e\_El}(T) = 385$(3.63)	T ≥ 273.15

Table 3.5 – AISI 1010 steel and UNS C15000 zirconium copper electrode, chemical composition in %*.

Material	C	Mn	P	S	Cu	Zr	Fe
AISI 1010	0.08 - 0.13	0.3 - 0.6	0 - 0.04	0 - 0.05	-	-	99.18 - 99.62
UNS C15000	-	-	-	-	99.8 - 99.9	0.1 - 0.2	-

**Typical composition*

3.2.1.3.2 Model configuration

A three-dimensional model has been used in this work. The model includes two truncated zirconium copper welding electrodes [107]. Figure 3.2 gives details on electrodes shape and dimensions.

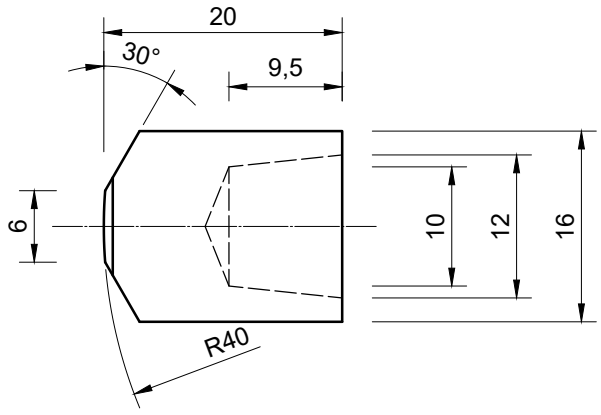

Figure 3.2 – Welding electrode geometry, dimensions in $[mm]$

In this model, welding electrodes are considered moving only vertically. Convective cooling is applied on the internal faces of electrodes in order to reflect the movement of

water in the electrodes during welding. Air convective cooling is applied on all external boundaries. Figure 3.3 shows the transversal section of the welding electrodes along with plates to be welded.

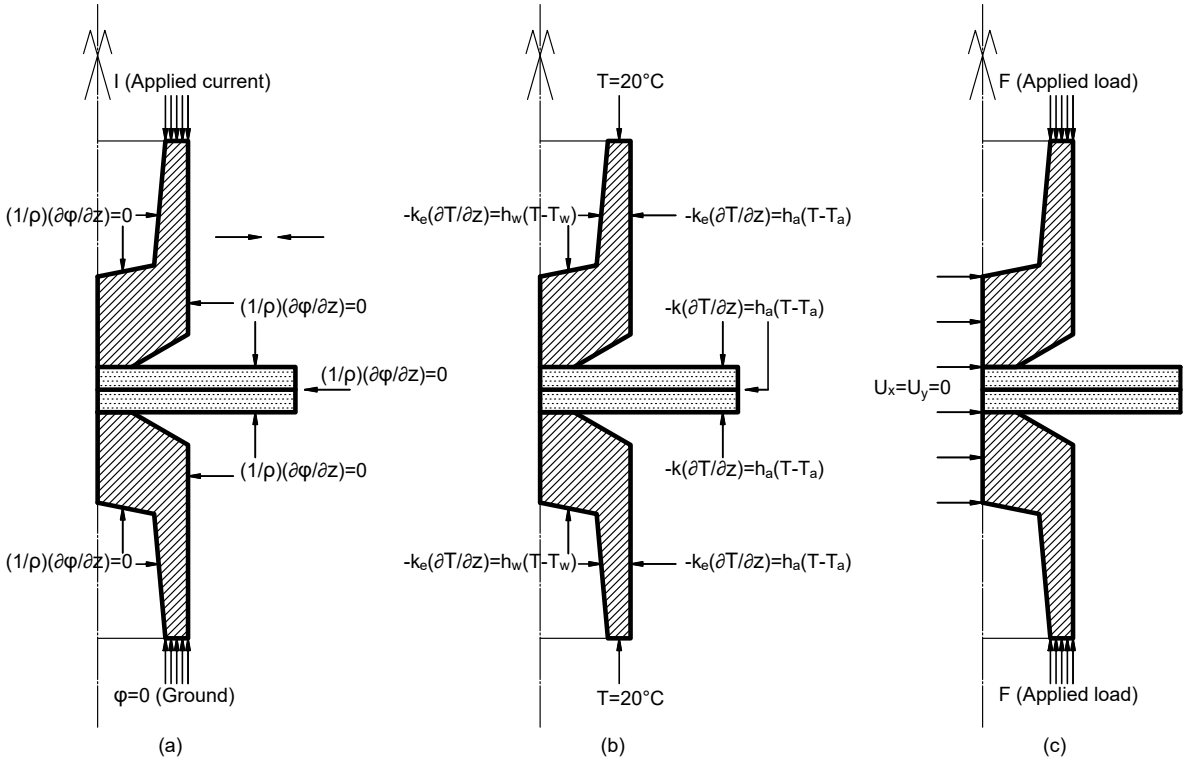

Figure 3.3 – Welding configuration along with graphical boundary conditions (BC). (a) electrical BC, (b) thermal BC and (c) Solid mechanics BC

For the coherence and validity of the model, the following solving algorithm has been designed and implemented for the simulation of the whole RSW process (Figure 3.4). In order to evaluate the meshing level, a convergence study has been made prior to the full utilization of the model (Figure 3.5). Several meshing levels have been used and it has been observed that as the average element size become less than 5.90 mm, the temperature profile of the weld center becomes more reliable and does no more change when refining meshing.

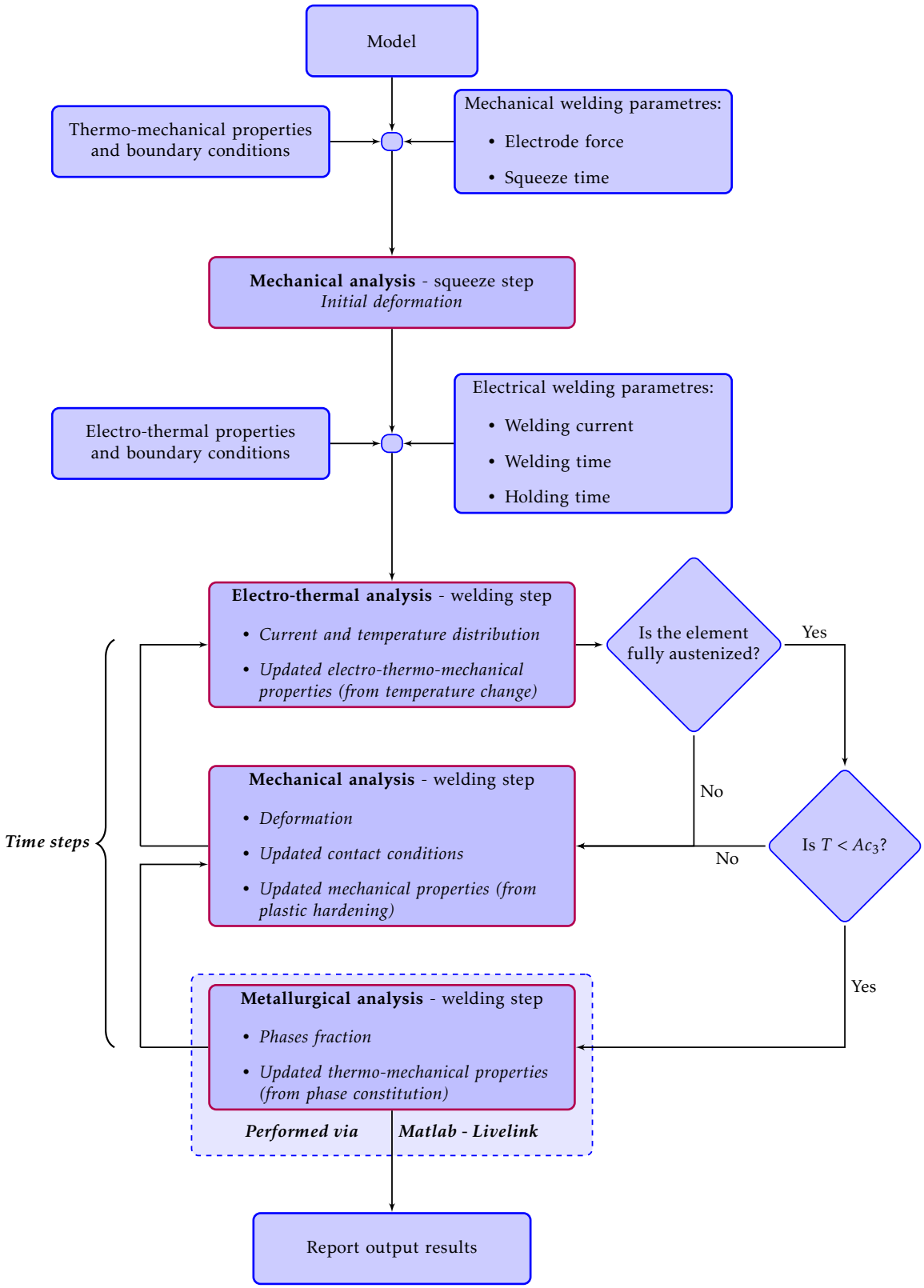

Figure 3.4 – Proposed finite element solving algorithm for simulation of RSW process

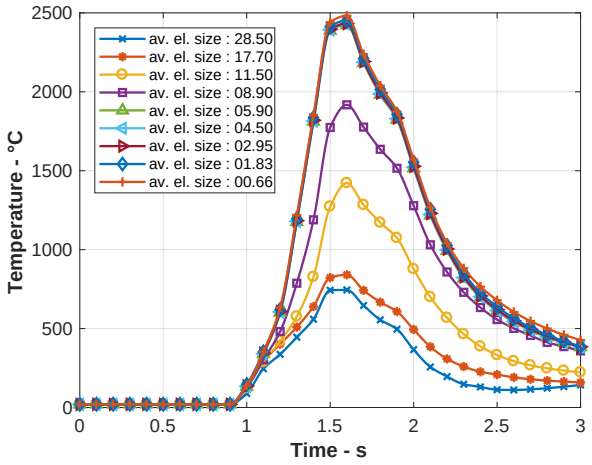

Figure 3.5 – Convergence study

3.2.2 Experimental configuration

In order to estimate the significance of simulation results, real welding experiments have been carried out. Welding have been done on 2 mm AISI 1010 steel sheets, following the simulation parameters. Tests have been done on a COMPUSpot Fusion 900 spot welder. Figure 3.6 gives details on welding configuration (arrangement of steel sheets). The weld geometry was the principal source of comparison between simulated and experimental processes.

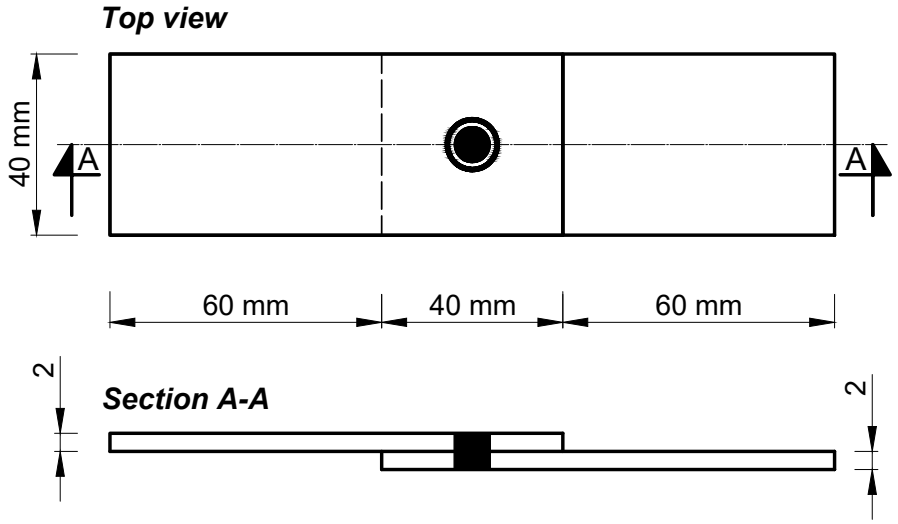

Figure 3.6 – Welding configuration

3.2.3 Current schedule

Current schedule in RSW encloses three main steps, namely the ramp up step, the welding step and the ramp down step. Applying that schedule generally lead to strong welds. However, as the RSW process is very fast, weld nugget usually experiences fully martensitic transformation. For that reason, PWHT have been applied to welds in order to reduce the cooling rate and therefore reduce the martensite content in the weld nugget. PWHT is applied here through the current ; it consists of maintaining a low-level current for a given time after the weld is done. That low level current, generally called post-heat current (PHC) is equal to the one third of the welding current in this work. Simulations and experiments were done for both normal current and PHC (PWHT) schedules. The effect of PHC on several variables has then been evaluated.

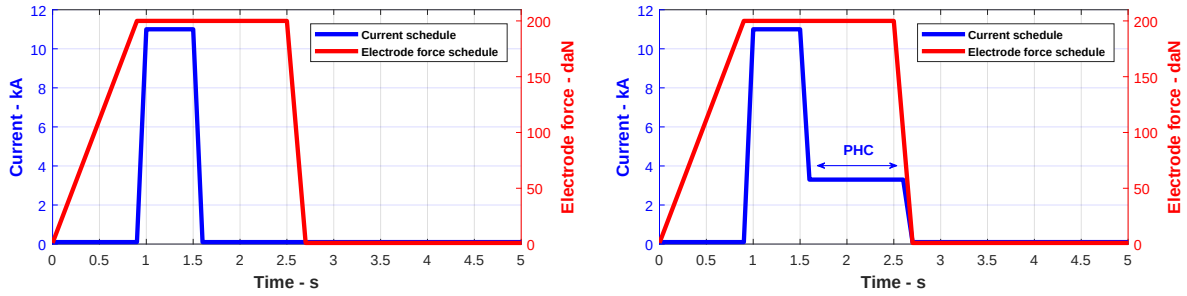

(a) Normal weld **(b)** Post heat-treated weld

Figure 3.7 – Scheduling of welding parameters (current and electrode pressing force)

3.3 Results and discussion

3.3.1 Weld temperature profile

The weld temperature profile provides important data that are essential for nugget geometry estimation. That temperature profile is simply the evolution on temperature throughout the metal during the welding process. Figure 3.8 gives temperature distribution in the nugget when heating is completed. It can be observed that the melted metal has an oval shape for both normal and post-heat treated weld. Temperature distribution in weld after 900 ms of cooling is displayed in Figure 3.9. It can be observed that for a normal weld (Figure 3.9.a), the maximum temperature (400°C) is less than

the martensite start transformation (455°C) ; therefore, the phase transformation is almost completed. However, for the post-heat treated weld (Figure 3.9.b), the temperature distribution presents a quite different scenario, temperatures ranges from 433°C to 850°C, which mean that at this particular time step, some parts of nugget are already fully transformed while other parts have not even started the transformation process. That fact enables to make hypotheses about an existence of diversity of phases in post-heat treated welds.

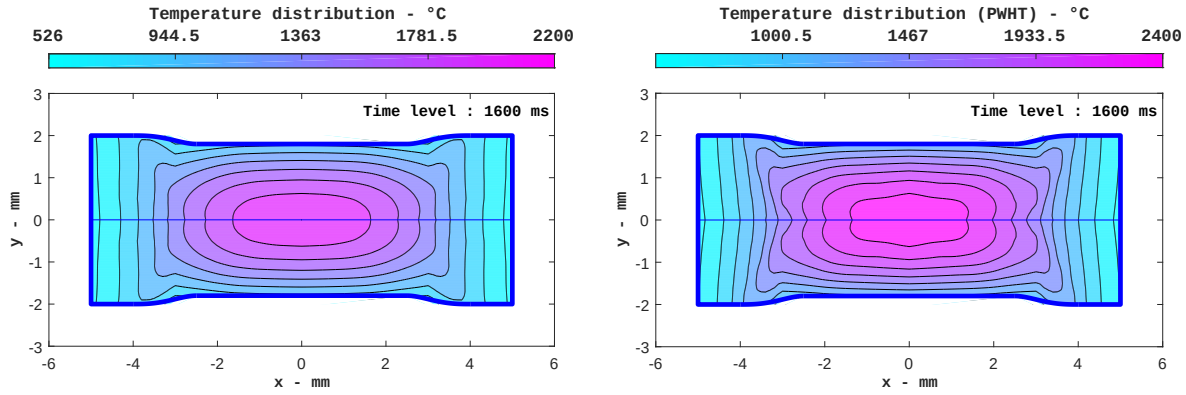

(a) Normal weld **(b)** Post heat-treated weld

Figure 3.8 – Nugget temperature distribution at the end of heating stage (t=1600 ms)

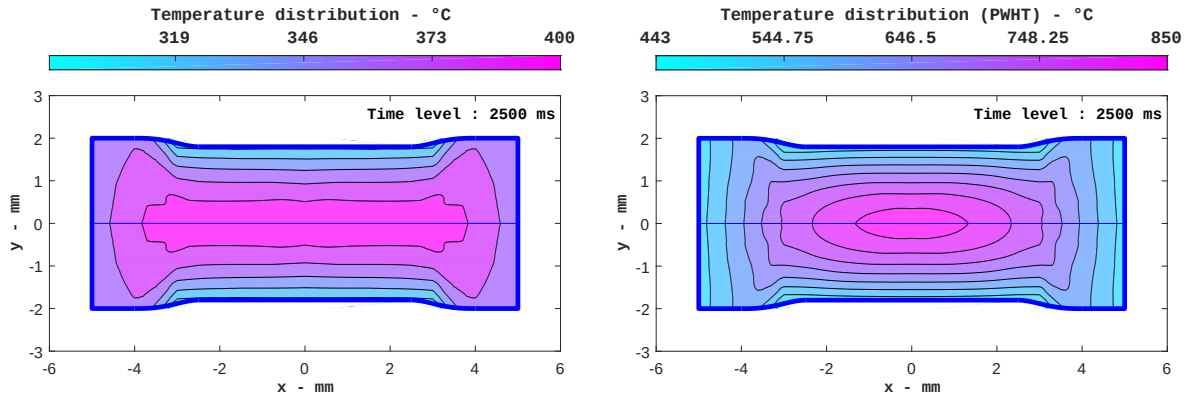

(a) Normal weld **(b)** Post heat-treated weld

Figure 3.9 – Nugget temperature distribution during the cooling stage (t=2500 ms)

3.3.2 Weld geometry

In resistance spot welding, nugget geometry is the first indicator of weld quality and strength. The most important geometrical variables are nugget diameter and nugget

height. Figure 3.10 shows the evolution of simulated nugget diameter and height as function of time. The nugget geometry discretization was performed with temperature distribution and the following hypotheses [108] :

- $(T_{\max} \geq T_L) \Rightarrow$ Fusion zone (FZ),
- $(T_L < T_{\max} \leq T_S) \Rightarrow$ Super-critical HAZ (SpC.HAZ),
- $(T_S < T_{\max} \leq Ac_3) \Rightarrow$ Inter-critical HAZ (IC.HAZ),
- $(Ac_3 < T_{\max} \leq Ac_1) \Rightarrow$ Sub-critical HAZ (SbC.HAZ),
- $(T_{\max} < AC_1) \Rightarrow$ Unaffected base metal (U.BM).

Table 3.6 – Numerical values of temperature ranges for AISI 1010 [100, 108]

Item	**Definition**	**Numerical value** $(\deg C)$
Ac_1	Austenite at which austenite begins to form	732
Ac_3	Temperature at which ferrite to austenite transformation is completed	927
T_S	Solidus : highest temperature at which an alloy is solid	1430
T_L	Liquidus : temperature where the alloy is completely melted	1515.56

Experimental nuggets widths and heights are compared to the simulated values in Figure 3.11.

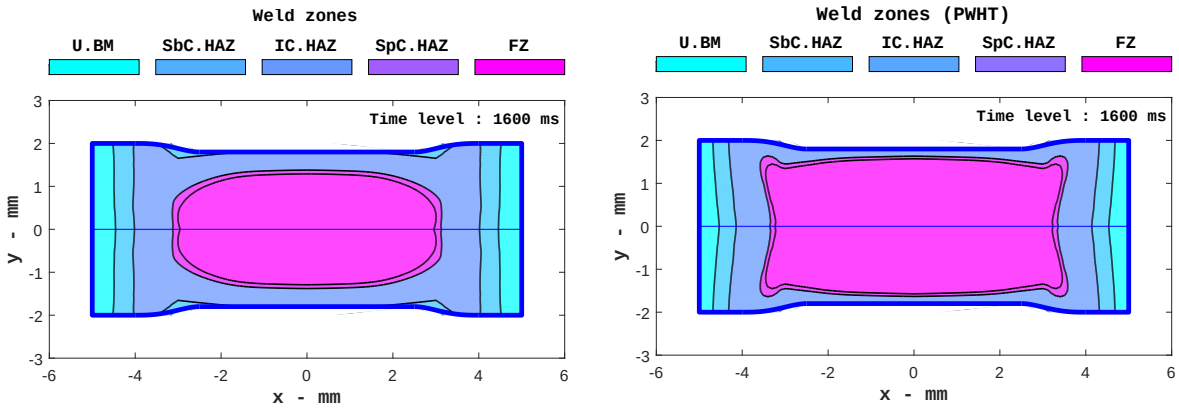

(a) Normal weld

(b) Post heat-treated weld

Figure 3.10 – Simulated nugget geometry

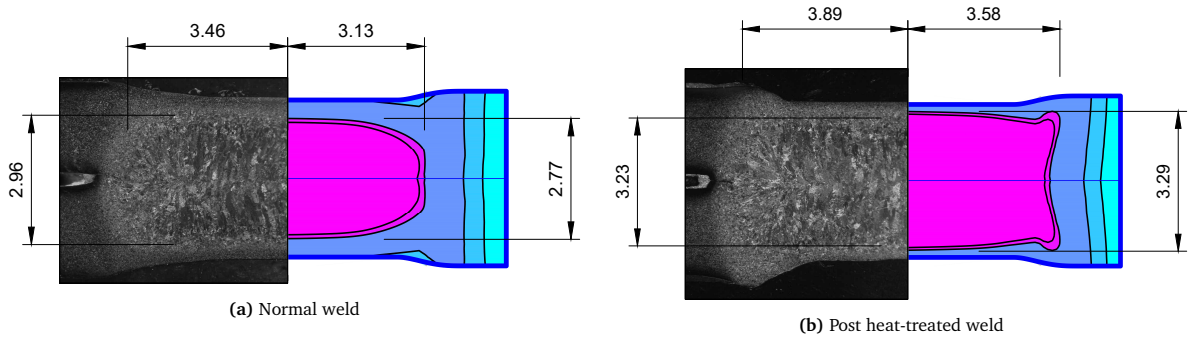

(a) Normal weld

(b) Post heat-treated weld

Figure 3.11 – Comparison between simulated and experimental nugget diameter, *dimensions in* $[mm]$

It can be seen on Figure 3.10 that the nugget diameter is slightly greater than 6 mm, which is a good value according to standards. In fact, according to the procedure of spot welding for uncoated and coated low carbon steels [109] :

$$3.5\sqrt{t} \leq d \leq 5\sqrt{t} \tag{3.64}$$

In the present work the sheet thickness $t = 2mm$,

$$\Rightarrow 4.95\text{mm} \leq d \leq 7.07 \tag{3.65}$$

Therefore, the simulated diameter $d \approx 6$mm is fully conform as regarding standards. The simulated heat affected zone (HAZ) at nugget surface here is quite wide and forms a ring of $0.5mm$ width, meanwhile experimental HAZ at nugget surface was a little smaller with a width of about $0.4mm$ for the normal current schedule while for a post heat treated weld, the HAZ width at nugget surface is $0.26mm$ and $0.25mm$ for simulation and experiment respectively. Table 3.7 gives recapitulation of the comparison between simulated and experimental geometric parameters.

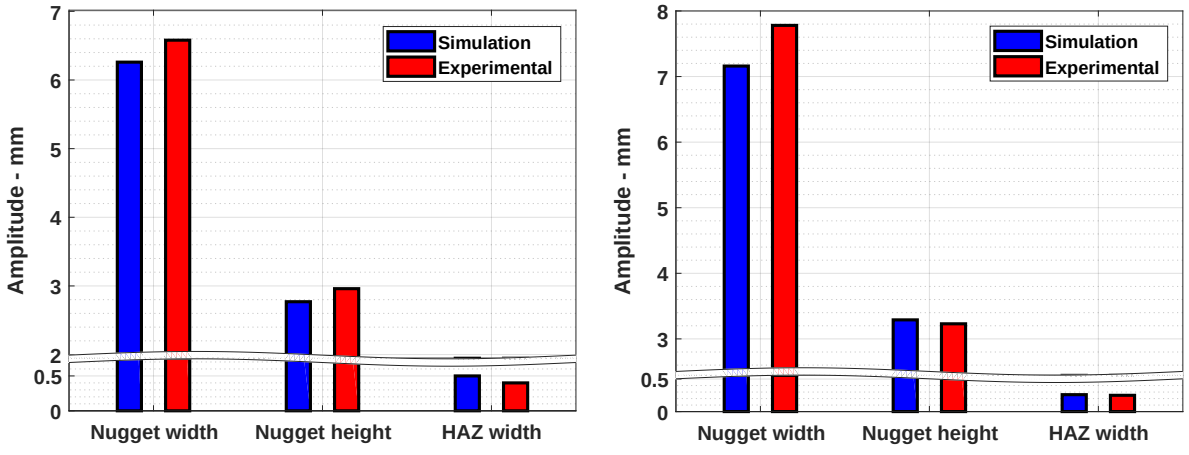

(a) Normal weld **(b)** Post heat-treated weld

Figure 3.12 – Comparison between simulated and experimental nugget geometry

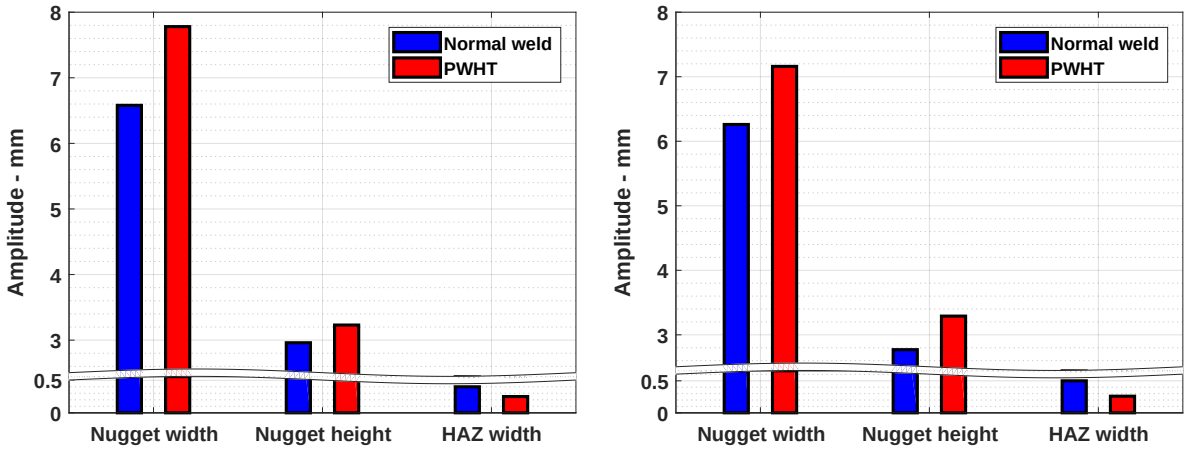

(a) Simulation **(b)** Experimental

Figure 3.13 – Effect of post weld heat treatment on nugget geometry

Table 3.7 – Comparison of geometrical parameters from simulated and experimental results

Current schedule	**Sources**	**Nugget width** $[mm]$	**Nugget height** $[mm]$	**HAZ width at nugget surface** $[mm]$
Normal weld	Simulation	6.26	2.77	0.5
	Experimental	6.58	2.96	0.4
	Relative error	-5%	-7%	20%
PWHT	Simulation	7.16	3.29	0.26
	Experimental	7.78	3.23	0.25
	Relative error	-9%	2%	4%

Table 3.8 – Effect of PWHT on nugget geometry

Current schedule	**Sources**	**Nugget width** $[mm]$	**Nugget height** $[mm]$	**HAZ width at nugget surface** $[mm]$
Simulation	Normal weld	6.26	2.77	0.5
	PWHT	7.16	3.29	0.26
	Increament	14%	19%	-48%
Experimental	Normal weld	6.58	2.96	0.4
	PWHT	7.78	3.23	0.25
	Increament	18%	9%	-38%

3.3.3 Phase transformation kinetics for a finite element

The metallurgy module enables to track the microstructure evolution in any finite element throughout the welding process. The calculations start by the determination of cooling curve, followed by the phase fraction calculation. In order to highlight the effect of PWHT on weld final microstructure, a finite element situated in the fusion zone boundary has been selected. Figure 3.14 shows cooling curve of the selected finite element for both normal weld and PWHT. The evolution of volumetric phase fraction in the selected finite element is shown in Figure 3.15. It can be observed that for a normal weld, the transformation in the element is almost fully martensitic, with up to 97% of martensite and only 3% of bainite. Meanwhile, when performing the post-weld heat treatment, the cooling speed is reduced and there is a formation of not only martensite but also of bainite (up to 7%) and ferrite (up to 4%). What confirms the increase of phase diversity in the nugget when applying PWHT.

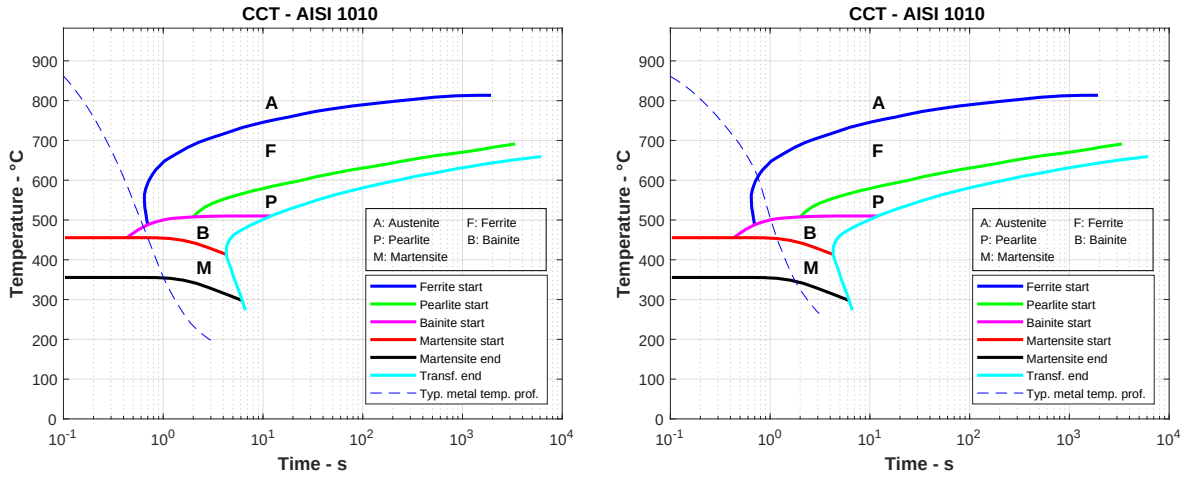

(a) Normal weld **(b)** Post heat-treated weld

Figure 3.14 – Continuous cooling transformation diagram

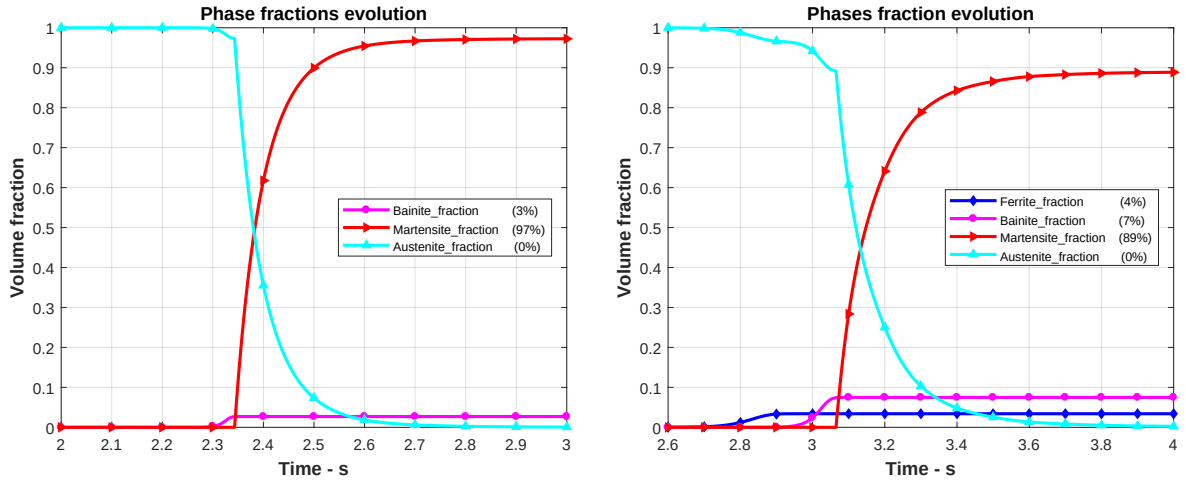

(a) Normal weld **(b)** Post heat-treated weld

Figure 3.15 – Evolution of volumetric phase fraction

3.3.4 Phase transformation kinetics all over the weld nugget

The metallurgy module also gives the phase transformation kinetics in the whole weld nugget. Ferrite, bainite and martensite fractions were represented on a transversal section of the nugget. Figure 3.16 shows the initiation of phase transformation in the nugget during the cooling process. It can be observed that bainite grows horizontally from the circumference to the center of the nugget in the case of normal weld and vertically in the case of post-heat treated weld. Ferrite grows spherically from outside to

the center of the nugget, while martensite grows from the top and bottom of the nugget to its center. Final phase fractions are plotted in Figure 3.17, it is seen that for a normal weld (Figure 3.17.a), bainite is mainly found at the circumference of the nugget, ferrite does not practically form, only four spots situated at the vicinity of super-critical HAZ experienced little ferrite transformation while martensite is omnipresent in the whole nugget area. For the post-heat treated weld (Figure 3.17.b), bainite is evenly distributed spherically in the nugget. Ferrite is distributed around the fusion zone and forms a ring in this case. Martensite is distributed throughout the nugget but with a smaller density.

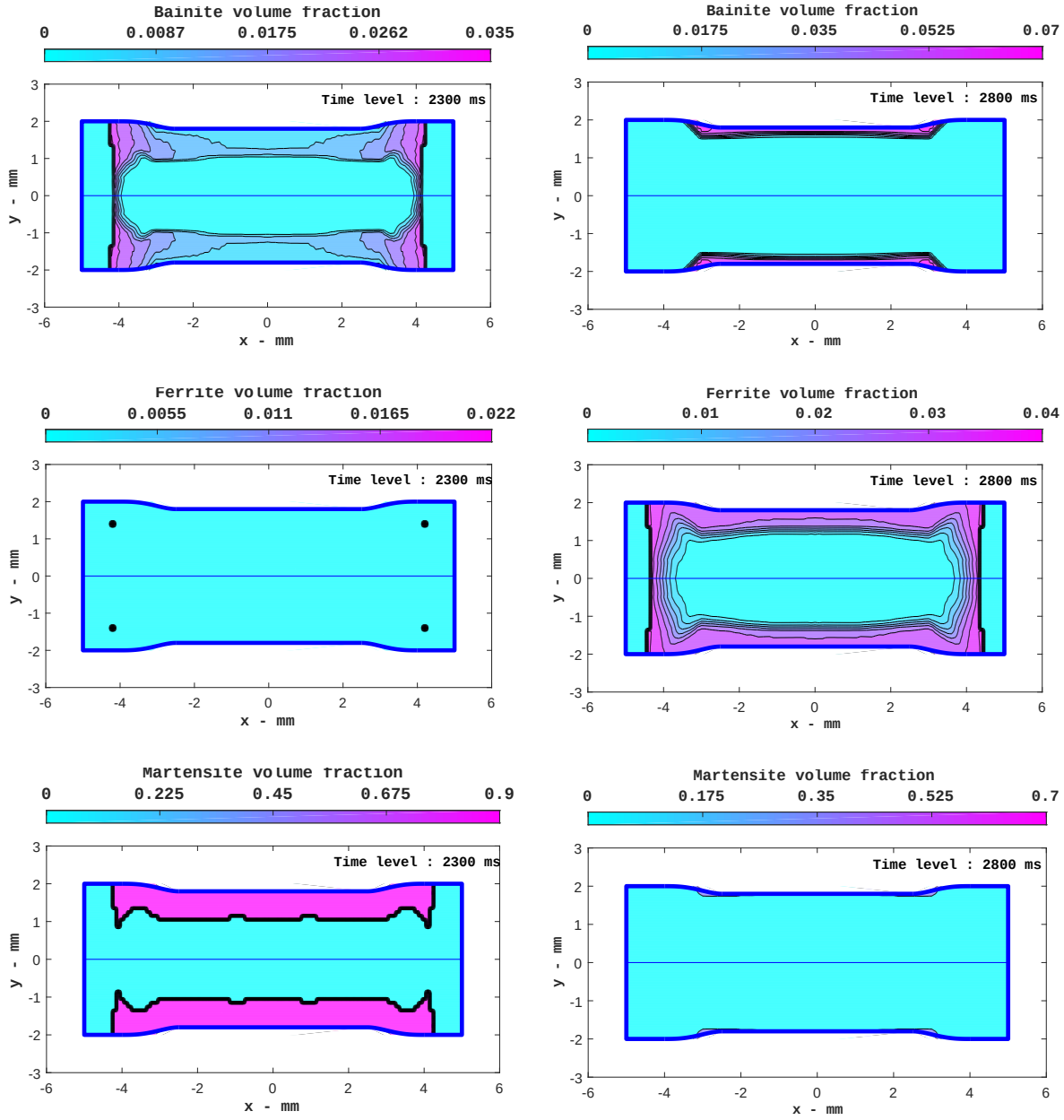

(a) Normal weld

(b) Post heat-treated weld

Figure 3.16 – Initiation of phases during nugget cooling

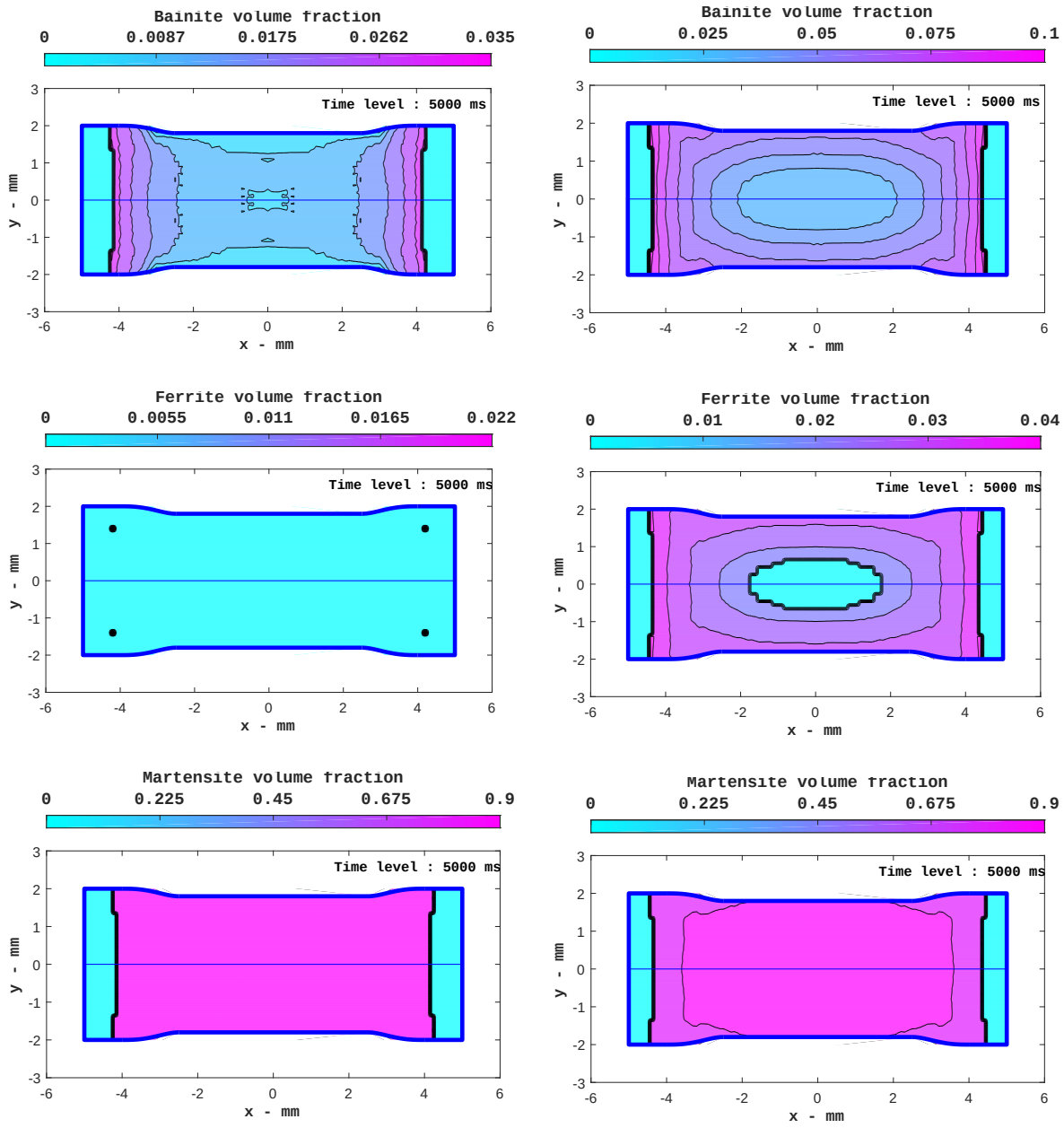

(a) Normal weld

(b) Post heat-treated weld

Figure 3.17 – Phase fraction in the nugget at the end of the welding process ($t = 5000ms$)

A calculation of average volume fractions has been done for both normal weld and post-heat treated welds, Figure 3.18 give details on volume fraction variance. The effect of PWHT on volume fraction has also been estimated in terms of change in percentage and values are given in Table 3.8.

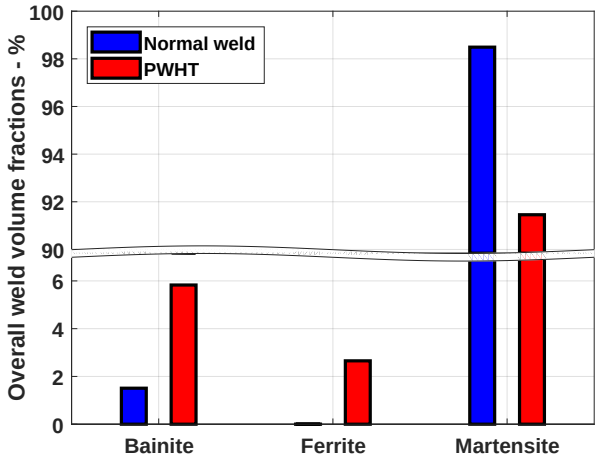

Figure 3.18 – Comparison of average volume fractions in the nugget (normal weld versus post-heat treated weld)

Table 3.9 – Recapitulation of average volume fractions and effect of PWHT

		Bainite	**Ferrite**	**Martensite**
Phase fraction (%)	Normal weld	1.51	0.0027	98.49
	PWHT	5.83	2.65	91.46
Effect of PWHT	Increase in phase fraction (%)	286.66	Inf.	-7.14

3.4 Conclusion

A fully electro-thermo-mechanical coupled model for resistance spot welding of 2 mm AISI 1010 steel sheets was developed in this work. This model enables to determine temperature evolution during welding and PWHT. From this temperature evolution, phase transformation kinetics in the weld nugget was predicted. Due to high speed of welding process, a technique called PWHT has been applied in order to reduce the cooling rate of the welded part and it effect on final phases fraction was investigated. Physical welding experiments were carried out in order to assess the validity of the proposed model.

The followings conclusions have been drawn from results analyses :

- Experimental and simulation results are in good agreement, the correlation coefficient between experimental and numerical weld nugget geometry is about 94%.
- In a normal welding of AISI 1010 steel grade, the transformation in the weld nugget is almost fully martensitic,
- The application of PWHT lead to an increase of bainite and ferrite factions and to a decrease of martensite fraction in the weld nugget.
- Bainite forms horizontally from nugget outside while martensite forms vertically from nugget top and bottom to its center.
- The application of PWHT has a significant effect on weld nugget geometry, namely an increase of 18% and 9% in nugget width and nugget height respectively while there is a decrease of 3% in nugget HAZ width at nugget surface.

Chapitre 4

Online Monitoring of Weld Quality in Resistance Spot Welding of A36 Mild Steel through Dynamic Resistance

CanWeld Conference 2019 - CWB Group

B. V. Feujofack Kemda[ψ,*], H. Ramiarison[ψ], N. Barka[ψ], M. Jahazi[χ] and D. Osmani[ζ]

Sommaire

Submitted on September 27th 2019, Revised on October 18th 2019

Online link

**Corresponding author - E-mail address :*bleriotvincent.feujofackkemda@uqar.ca (B. V. Feujofack K.)
[ψ] *University of Quebec in Rimouski, Québec G56 3A1, Canada.*
[χ] *Ecole de Technologie Superieure, Montréal, Québec H3C 1K3, Canada.*
[ζ] *AMH Canada Ltd, Rimouski, Québec G5L 1Z2, Canada.*

Avant-propos

Auteurs et affiliations

Blériot Vincent Feujofack Kemda : Étudiant en maîtrise en ingénierie, Département de mathématiques, d'informatique et de génie, Université du Québec à Rimouski, Rimouski, Québec G56 3A1, Canada.

Herinandrianina Ramiarison : Étudiant en maîtrise en ingénierie, Département de mathématiques, d'informatique et de génie, Université du Québec à Rimouski, Rimouski, Québec G56 3A1, Canada.

Noureddine Barka : Professeur, Département de mathématiques, d'informatique et de génie, Université du Québec à Rimouski, Rimouski, Québec G56 3A1, Canada.

Mohammad Jahazi : Département de génie mécanique, École de technologie supérieure, Montréal, Québec H3C 1K3, Canada.

Denis Osmani : AMH Canada Ltée, Rimouski, Québec G5L 1Z2, Canada

Titre en Français

Surveillance en temps réel de la qualité des soudures par résistance par points d'acier doux A36 à l'aide des signaux de résistance dynamique.

État de l'article

Publié et présenté à la conférence : « CanWeld Conference 2019 ».

Contribution au mémoire

Cet article de conférence constitue la quatrième partie de ce mémoire. Dans ce dernier, une méthode qui permet de mettre en évidence des soudures peu intègres pendant le processus de soudage a été développée. L'approche mise en oeuvre est basée sur la signature de résistance dynamique des joints soudés, qui est déterminée à partir de l'acquisition en temps réel des signaux de courant et de tension de soudage. Une série d'expériences de soudage a été réalisée sur de l'acier doux ASTM A36. À partir

d'analyses statistiques et de l'exploitation des résultats expérimentaux, un fuseau de passage de validation de résistance dynamique a été déterminé et permet de contrôler la qualité des soudures. Mis à part le contrôle de la qualité des joints soudés, l'approche mise en oeuvre permet également de déterminer les conditions physiques de soudage des soudures effectuées.

Résumé en Français

Le soudage par résistance par points est l'une des techniques d'assemblage les plus utilisées dans les industries aérospatiale et automobile. Aujourd'hui, ce processus a été entièrement automatisé afin d'augmenter la vitesse de production et la répétabilité. Cependant, le soudage par résistance par points reste confronté à plusieurs autres problèmes. L'un de ces problèmes est l'intégrité des soudures effectuées. En effet, en raison de risques divers, les conditions de soudage ne sont jamais les mêmes et les soudures qui en résultent sont parfois de mauvaise qualité. Dans le présent article, nous présentons une méthode qui permet de mettre en évidence ces mauvaises soudures pendant le processus de soudage. L'approche mise en œuvre est basée sur la signature de résistance dynamique des joints soudés, qui est déterminée à partir de l'acquisition en temps réel des signaux de courant et de tension. Une série d'expériences de soudage a été réalisée sur de l'acier doux A36. A partir d'analyses statistiques et de l'exploitation des résultats expérimentaux, un fuseau de validation de la résistance dynamique a été déterminé et permet de contrôler la qualité des soudures. Outre le contrôle de la qualité, l'approche mise en œuvre permet également de déterminer les conditions physiques de soudage des soudures effectuées, telles que l'état de surface des tôles, la présence de limaille de fer, les soudures qui se chevauchent, le soudage d'une seule tôle, les tôles bombées et l'absence de tôle pendant le soudage.

Abstract

Resistance spot welding is among the most used joining techniques in aerospace and automotive industries. Nowadays this process has been fully automated in order to increase the production speed and repeatability. However, resistance spot welding still faces several other issues. One of these issues is the integrity of performed welds. Indeed, due to miscellaneous hazards, welding conditions are never the same and resulting welds are sometimes of poor quality. In the present paper, a method which enables to point out these bad welds during the welding process is presented. The implemented approach is based on nugget dynamic resistance signature, which is determined from the real-time acquisition of current and voltage signals. A series of welding experiments was carried out on A36 mild steel. From statistical analyses and exploitation of experimental results, a dynamic resistance validation passageway was determined and it enables to monitor welds quality. In addition to the monitoring of quality, the implemented approach also enables to figure out physical welding conditions of performed welds such as sheet surface condition, presence of dirt, overlapping welds, one sheet welding, curved sheets, and absence of sheets during welding.

Keywords : Resistance spot welding ; Welding conditions ; Dynamic resistance signature ; Statistical analyses ; Validation passageway ; Weld integrity

4.1 Introduction

Resistance spot welding, a process intensively used in the automotive industry, has undergone great advances in recent decades and allows to produce today, reliable and durable car bodies. This welding process uses the Joule effect of a current of high intensity, in a few kA, passing through the parts to be assembled. These parts are maintained by means of contact by copper electrodes which exert a clamping pressure and allow the passage of current [9, 34]. Resistance spot welding being converted in a robotic process, some poorly executed welds are often not detected and thus, they lead to structures with poor integrity and durability [110]. Hence, this justifies the need to implement intelligent weld inspection systems. The dynamic resistance, a quantity calculated from the instantaneous values of the voltage between the electrodes and the corresponding current is a good way to monitor the welding process[111]. Many other researchers such as Savage et al.[112] and Gedeon et al.[113] have reported that dynamic resistance could be used to evaluate nugget quality. In the early 2000, the interests in dynamic resistance tracking grew more. Wang et al.[114] modeled electrical dynamic resistance during spot welding and determined the effect of various parameters on dynamic resistance. Recent development have also been done in order to improve the measurement accuracy when dealing with dynamic resistance during spot welding [115–118].

This work aims in the design and implementation of a dynamic resistance acquisition system for monitoring purposes and the evaluation of nugget quality in real time.

4.2 Experimental considerations

4.2.1 Welding equipment

The machine used for welding is shown in Figure 4.1. It can generate a welding current of up to 14 kA. The voltage generated at the electrode ends is very low, it is about ten volts.

(a) **COMPU**SPOT® 900

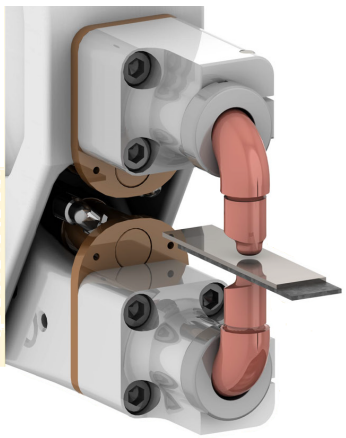

(b) Details of welding head

Figure 4.1 – Welding equipment

4.2.2 Data acquisition

4.2.2.1 Sensors

Data acquisition for this project requires two sensors, the first for current signal and the later for voltage signal. For the current, a 400K MB Rogowski coil is used and for voltage, a voltage sensor system that is directly connected to the MyDAQ system has been designed.

a. Rogowski coil

Operating principle : The toroidal coil is a sensor that measures the current passing through a conductor. Another name exists for this kind of sensor which is Rogowski coil. A 400K MB Rogowski coil which consists of a copper wire that wraps around an iron core arranged in a belt (Figure 4.2) was used. All this is protected by an insulation envelope

that reduces risks.

The principle of Rogowski coil is simple because it relies on the fundamental laws of electromagnetism. When a current passes through a conductor, a magnetic field is generated. This magnetic field will interact with coil and this will result in an induced voltage that is proportional to the variation of the current along the conductor. The relationship between voltage and current can be determined by Faraday's law [120–122] :

$$V(t) = \frac{A}{S} \cdot \mu_0 \cdot I(t) \tag{4.1}$$

With :

μ_0	Magnetic permeability
A	Winding section
S	Number of revolutions per unit of measurement

This induced voltage is measured as output from the coil to determine the current intensity generated by the welding machine.

Calibration : It should be noted that resistance spot welding requires a very high current intensity, about 15×10^3 A. To calibrate the Rogowski coil, a current generator capable of supplying as much welding current was needed. However, it is rare to find such a generator, and in the environment where the work was carried out, only the welding machine could generate such values.

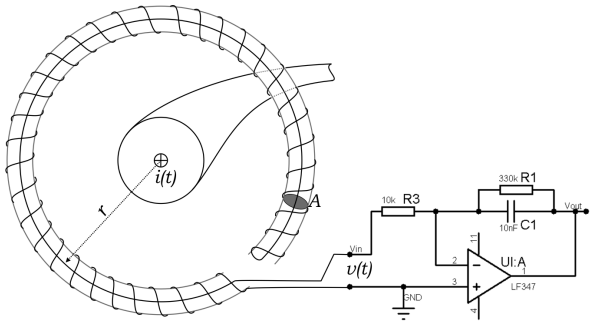

Figure 4.2 – Rogowski coil MB400K [119]

From the literature review carried out, no document concerning the MB 400K Rogowski coil mentioned the output voltage of the coil. Even on the manufacturer's website (AMADA MIYACHI®), no information were available on this feature. Only geometric information were given in the documents provided about the MB 400K Rogowski coil.

However, knowing that the voltage at the output of the coil is proportional to the current flowing along a conductor from what was seen in the Equation 4.1, several measurements were made to determine the linear equation that gives the relationship between the current and the voltage output of the MB 400K Rogowski coil. This relationship allowed us to determine the current intensity according to the voltage obtained from the coil.

For this calibration purpose, a high sensitivity multimeter was used to measure the voltage at the output of the Rogowski coil (placed around welding electrodes). The series of measurements performed allowed us to deduce that the MB 400K Rogowski coil has an output voltage of $470mV$ per $1000A$ - AC.

b. Voltage measurement

The voltage measurement was carried out using a voltage probe system directly linked to the data acquisition device. The system consisted of an electrical cable attached to the electrodes of the spot welding machine. The wires were arranged in such a way as to reduce as much as possible the noise that could interfere with the measurements, this was done by minimizing the space between the wires and the electrodes as much as possible.

4.2.2.2 Experimental set-up

As it can be seen in Figure 4.3, the sensors are placed directly on the welding machine. The cables for voltage measurement are attached to the electrodes and are connected to the MyDAQ board. The Rogowski coil is placed around the electrode. Measurements made by placing the Rogowski coil in different ways showed that the arrangement of the Rogowski coil does not affect the output value. For this reason, the

most stable location that does not generate any disturbance during the welding process was chosen.

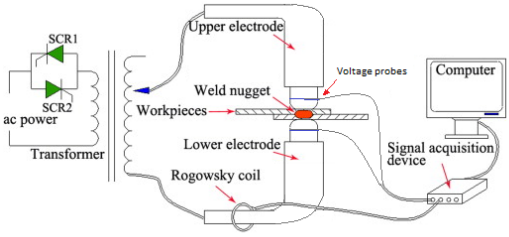

(a) Schematic of acquisition system (Adapted from Zhang et al. [123])

(b) Welding equipment and measurement setup

Figure 4.3 – Experimental set-up

4.2.2.3 Acquisition system

a. Signal conditioning

It should be noted that the signals need to be conditioned since many disturbances occur during the welding process and affect the quality of signals. This noise is mainly due to phenomena that are related to the welding machine and equipment. These include the vibration of the electrodes during welding and the induced voltage generated by the passage of current through a conductor.

Conditioning of current signals : Measurements made during the calibration of the Rogowski coil showed that the values of the voltage at the output of the Rogowski coil are low, varying within a range of 2 to 4 $Volts$. In this sense, it was decided to pass the signals through an amplifier with a gain of 2; for the noise from the various phenomena mentioned above, the use of a low-pass filter was recommended in order to obtain better quality signals .

The amplifier consists of a UA 741 op-amp that needs to be powered with a voltage of $+15V$ and $-15V$, and two similar resistors of $510\Omega \pm 1\%$ in order to reach the objective which is a gain of 2, so the output voltage of the coil is multiplied by two before passing through the low pass filter (Figure 4.4).

After it's amplification, the signal is filtered so that the accompanying noise is significantly reduced. To perform the filtering, a passive low-pass filter is used, which consists of a $0.01\mu F \pm 5\%$ capacitor and a $330k\Omega \pm 5\%$ resistance. Knowing that the frequency of the signals is $12.85Hz$ from to the preliminary measurements made in laboratory, the characteristics of the filter are as follows :

- Transfer function

$$V_o = \frac{V_i}{1.02} \tag{4.2}$$

  As $1.02 \simeq 1$,V_o and V_i are substantially equal.

- Cut-off frequency is 42.83 Hz

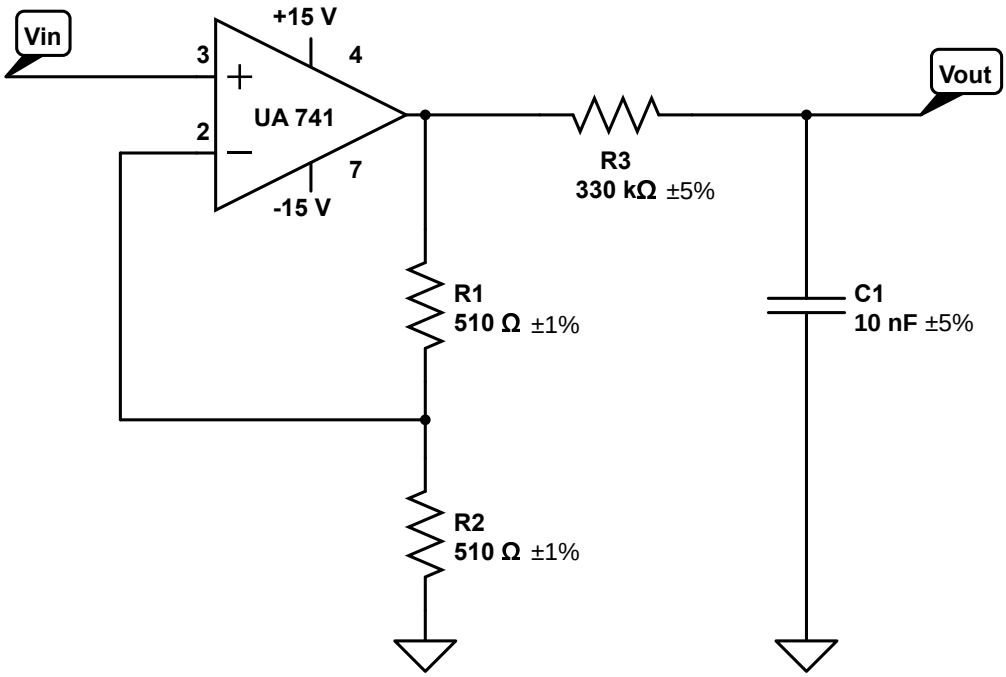

Figure 4.4 – Amplifier - low pass filter circuit

Conditioning of voltage signals : It is indicated on the welding machine that the voltage generated by the machine varies between 2 and $16V$. Knowing that the MyDAQ acquisition device which will convert analog signals into digital signals works in a range from -10 to $+10V$, it is important to make sure the input values fit in that interval to avoid

damaging the device. To achieve this, a voltage divider bridge that consists of two resistors of 510Ω to reduce the value of the voltage to half its value was used (Figure 4.5).

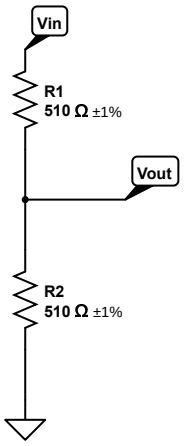

Figure 4.5 – Voltage divider bridge

b. Acquisition circuit

The acquisition circuit for current and voltage signals (Figure 4.6) consists of :

- The sensors given in the previous section,
- A NI (National Instruments) myProto board where the various components necessary for signal conditioning are arranged,
- A myDAQ acquisition board that convert analog signals into digital signals,
- A computer in which signals are processed and recorded using software dedicated to these tasks which are NI LabVIEW, Excel and MATLAB.

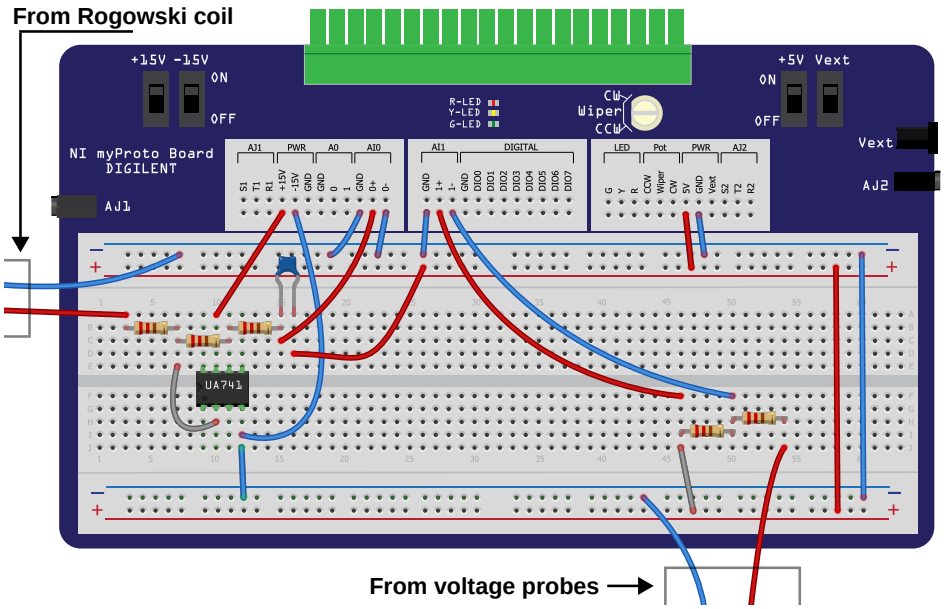

Figure 4.6 – Acquisition circuit board

c. Acquisition and recording of signals :

The signal acquisition is done on a computer with NI Labview software. It should be noted that after conditioning, the signals must pass through programs on Labview in order to have a reading of the actual values at the output. In this sense, for voltage, a program that will multiply the value in two is applied because, as mentioned in the previous section, the voltage passes through a voltage divider bridge that divides its value in two.

The same applies to the welding current expressed by a voltage at the output of the Rogowski coil and passing through an amplifier. The relationship between current and voltage determined during calibration was applied to give the welding current directly. Figure 4.7 shows the diagram of the LabVIEW program developed as part of this project.

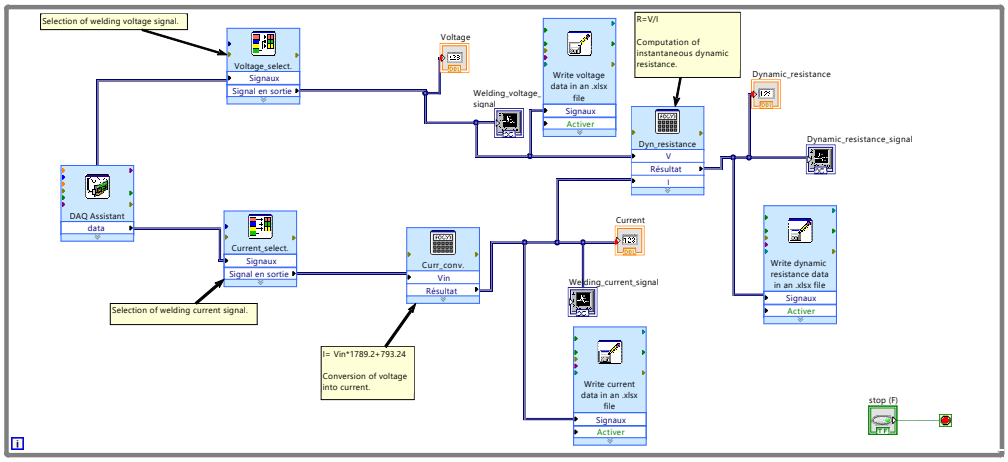

Figure 4.7 – Diagram of the program developed under LabVIEW

Once the entire circuit is in place, welding can be started, current and voltage signals, obtained. It can be seen that the signals only appear for a short period of time, since resistance spot welding is a very fast process, for this project, the welding time is 350 ms.

4.2.3 Signal processing

4.2.3.1 Objectives of signal processing

Signal processing is the discipline that develops and studies signal analysis and interpretation techniques. Among the possible types of operations on signals, one can denote control, filtering, data compression and transmission, noise reduction, deconvolution, prediction, identification, classification, etc. [124]

The main purpose of signal processing in this project is to reduce the noise, which, despite the presence of an analog filter in the circuit, has proven to be omnipresent. The signals were acquired in real time during the welding process. Following a test *lambda*, here are the results displayed in the LabVIEW interface.

The signal in red represents the voltage, the signal in white the current and the signal in blue the dynamic resistance. It can be noticed the difficulty of reading these signals. A procedure for processing and exploiting these latter has therefore been designed to make the most of the data acquired.

4.2.3.2 Signal Processing Methodology

a. Creation of an Excel database

In order to perform post-processing of all signals, they were saved in an Excel spreadsheet one by one and after each welding operation. Each signal is represented by two column matrices, the first indicating the time coordinate and the second indicating the amplitude of the acquired variable (either current or voltage). Time is subdivided here on a millisecond scale.

b. Filtering and display of signals via MATLAB®

Being in possession of several dozen signals to be processed, it seemed illogical to filter them one by one, that is why a MATLAB program was developed to systematically process the signals from LabVIEW (signals are save from LabVIEW program to Excel sheets, the MATLAB program then reads signals from Excel sheets). In general, this program performs several specific steps and provides data on filtered signals as they occur. These steps are as follows :

Step 1 - Reading and displaying raw signals : Here, the program reads the data relating to signals specified by the user and displays them as curves (Figure 4.8).

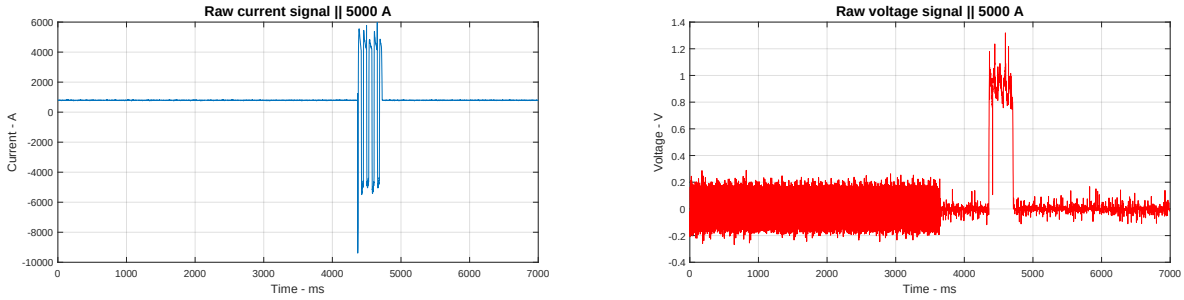

Figure 4.8 – Raw signals of current and voltage of a weld

Step 2 - Locating and extracting the desired part of the signal : The raw signals are defined over a period of 7 seconds. Since the welding is only effective over 350 ms, it is necessary to locate and segment the signals to keep only the desired part. A few lines of code allows this operation to be performed for all recorded signals (Figure 4.9).

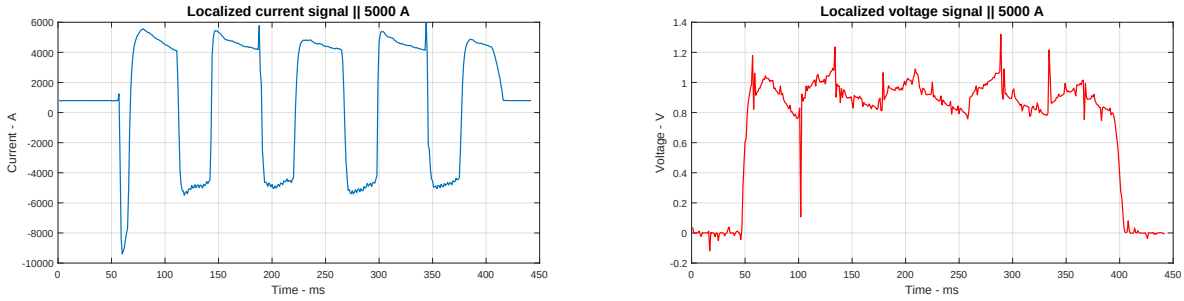

Figure 4.9 – Localized current and voltage signals

Step 3 - Signal filtering : After the signals have been located, the program filters them (Figure 4.10). The parameters of the filter are as follows :

- Filter type : Low pass
- Filter order : 20
- Cut-off frequency : 1 Hz
- Sampling frequency : 10 kHz

This makes it possible to switch from highly noisy signals to filtered and usable signals.

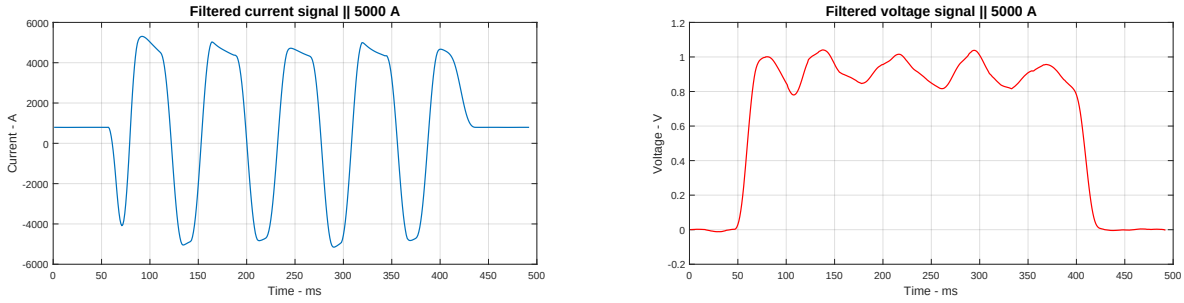

Figure 4.10 – Filtered current and voltage signals

Step 4 - Signal sampling : As the welding current here is alternating, it is therefore advisable to consider only positive values. To obtain a usable dynamic resistance, some discrete signal values were used, some researcher recommended to take these values at each current peak [113]. The curves obtained being broken lines, a smoothing is carried out in order to make them more homogeneous (Figure 4.11).

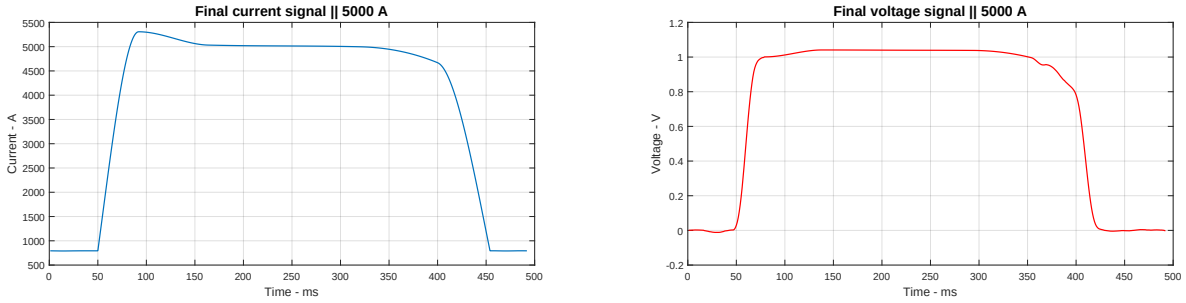

Figure 4.11 – Typical current and voltage signals from a weld

Step 5 - Calculation and plotting of the dynamic resistance : From the last current and voltage signals obtained, the dynamic resistance is deduced. Everything is based on Ohm's law.

$$V = R \cdot I \tag{4.3}$$

The dynamic resistance can thus be determined as a function of the welding voltage and current from the following relationship :

$$R_d = \frac{V}{I} \tag{4.4}$$

With :

$\boldsymbol{R_d}$	Dynamic resistance of the weld nugget (Ω)
$\boldsymbol{V}$	Voltage between electrodes (V)
$\boldsymbol{I}$	Welding current (A)

The Figure 4.12 represents a typical dynamic resistance signal of a weld nugget.

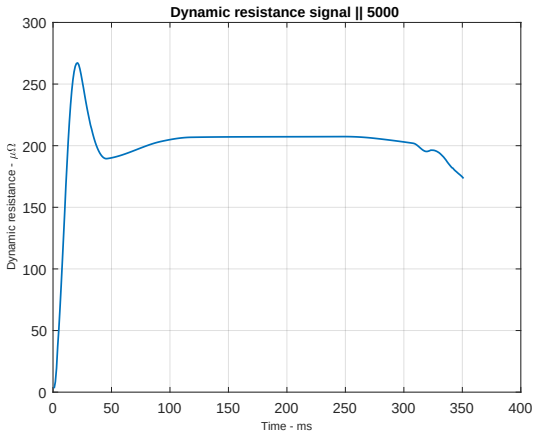

Figure 4.12 – Typical dynamic resistance signal of a weld nugget

A study was carried out on the basis of a comparison between the different dynamic resistance signals of good welds and those emanating from bad welds, the latter will highlight the correlation between the quality of the welds and their dynamic resistance signals.

4.3 Results and discussions

A battery of welds was made upstream by varying the welding parameters such as welding current, time and electrode pressing force. These welds are considered to be of good quality because no defects were found on the plates before, during and after the process was carried out. The signals from these welds were also considered as reference signals (Figure 4.13).

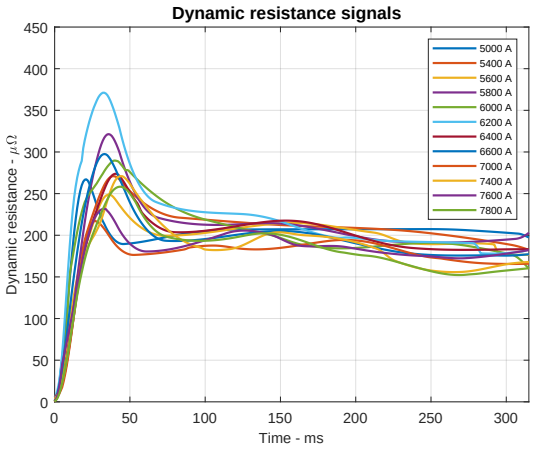

Figure 4.13 – Dynamic resistance signals of good quality (defect-free) welds

4.3.1 Passageway

A **Passageway**, defined by all the dynamic resistance signals corresponding to the so-called good quality welds, was thus drawn (Figure 4.14).

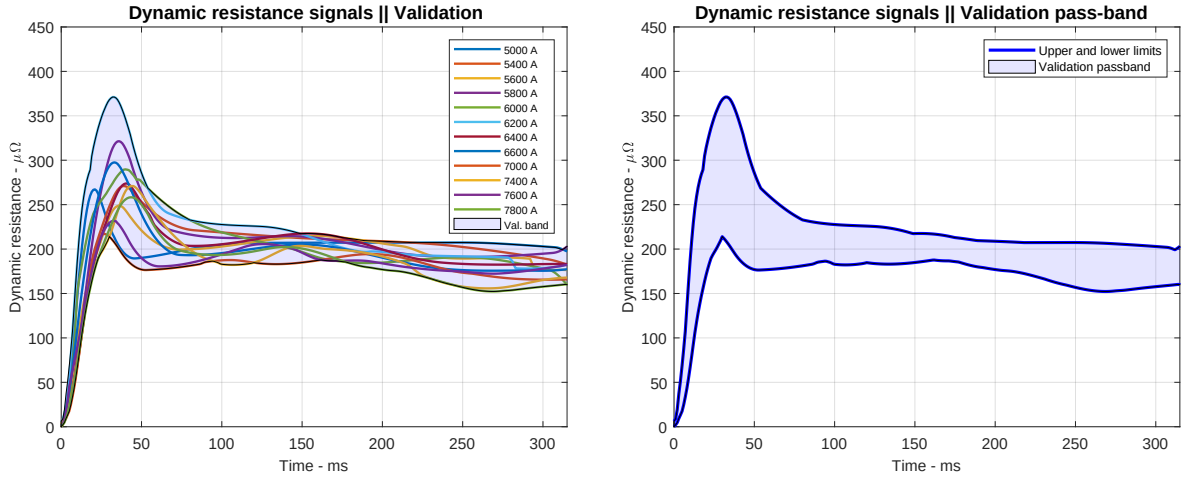

(a) Validation of good welds

(b) Passageway

Figure 4.14 – Successful welds passageway

This passageway represents a basis for judgment for any signal that would be recorded during the welding operation. Thus, if the dynamic resistance signal of a weld is in the passageway, the weld is considered to be of good quality and from good welding conditions **(Theory 1)**. If this is not the case, the operator may deduce that the

weld is not completely successful and must carry out an inspection, followed by a repair of the weld nugget if necessary.

4.3.2 Defective welds

In order to validate the *theory 1*, a series of welds was performed while obviously introducing defects in the plates. Six configurations of defective welds were tested, specifically, the following cases :

- Insertion of a sheet of paper between the plates to be welded (Paper),
- Presence of iron filings on the plates to be welded (Dust),
- Welding of a convex plate on a straight plate (Flat-convex),
- Welding of a single plate (One-sheet),
- Welding on and existing nugget (Doubling),
- Welding in the vacuum (Vacuum).

APPENDIX - A

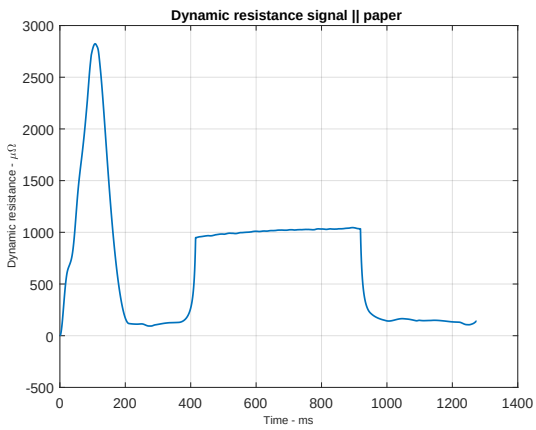

(a)

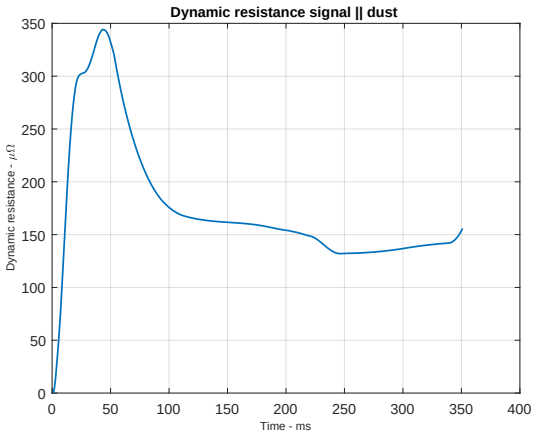

(b)

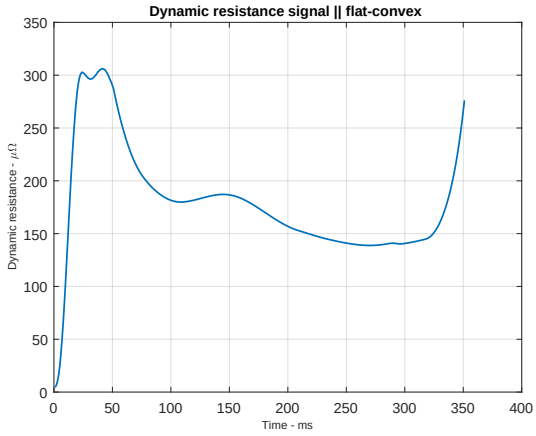

(c)

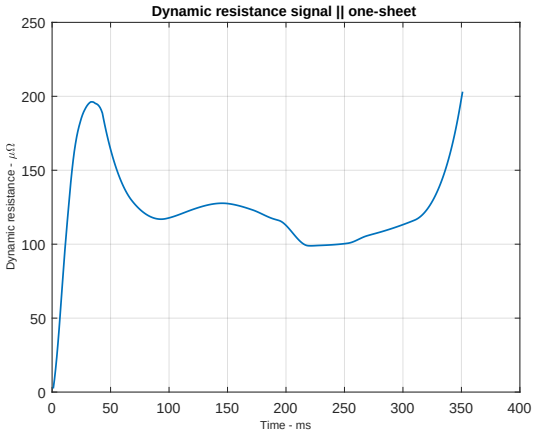

(d)

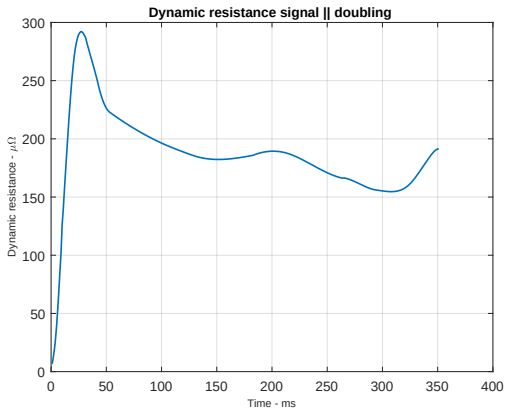

(e)

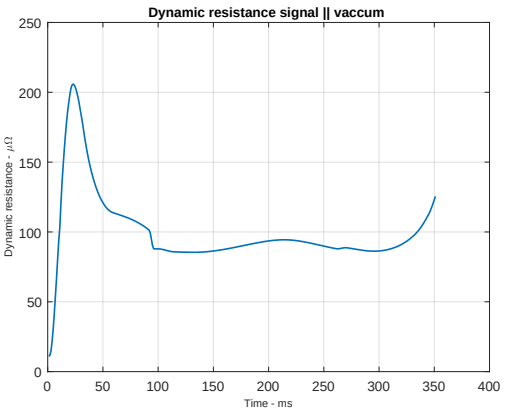

(f)

Figure 4.15 – Dynamic resistance signals from defective welds

These six welding variants, including obvious defects, made it possible to evaluate

the effectiveness of the *passageway* and the *theory 1*.

Figure 4.15 (Appendix A) represents the different dynamic resistance signals of welds with defects.

The signals from these welds do not perfectly fit into the welds *validation passageway* (Figure 4.16), which comforts the established *theory*. Nugget dynamic resistance signal thus represent a solid and reliable means of determining the physical conditions of welding and predicting the quality of welds.

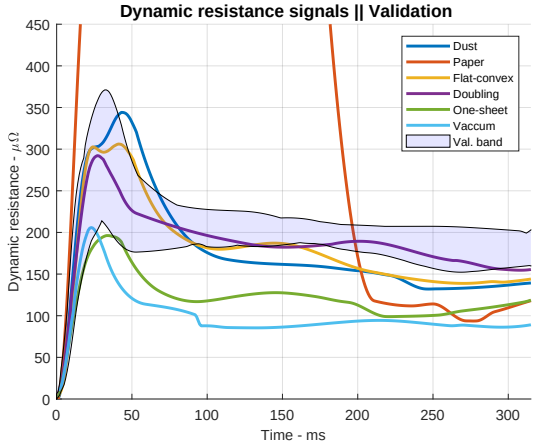

Figure 4.16 – Dynamic resistance signals of defective welds - validation

4.4 Conclusion

In this work, it was a question of acquiring dynamic resistance signals during the resistance spot welding operation of thin steel sheets. This was done in order control the process in real time and to predict the quality of the welds. To achieve this, the welding current and voltage signals were acquired using a Rogowski coil and voltage probes respectively. A conditioning circuit developed on a MyProto board, connected to a MyDAQ module and controlled by the 2018 version of LabVIEW software, made it possible to represent the signals in digital form and save them. A program developed under MATLAB made it possible to process and exploit these signals. The dynamic resistance of all welds was obtained by applying Ohm's law to the welding current and voltage signals. A series of welds was carried out by varying the welding current, a

representation of their dynamic resistances revealed a passageway. Any good quality weld should therefore have a dynamic resistance signal that would fit into the passageway *-Theory 1-*. In order to validate this theory, the signals of welds in which defects were wilfully introduced were traced. None of these signals fitted into the pre-set passageway. Which validates the established theory. It is therefore possible to determine welding conditions and predict weld quality using dynamic resistance signals.

Conclusion Générale

Ce mémoire présente une étude visant à améliorer le procédé de soudage par résistance par points des tôles minces pour l'industries automobile. Cette étude a été articulée autour de quatre objectifs spécifiques, à savoir : 1. Déterminer l'effet des paramètres de procédé sur la géométrie et la résistance mécanique des soudures par résistance par points ; 2. Optimiser les paramètres de procédé du soudage par résistance par points ; 3. Développer des outils pour la prédiction des cycles de chauffage/refroidissement permettant d'appliquer avec succès le soudage par résistance par points au aciers ultrarésistants ; 4. Développer une technique permettant de prédire la qualité des soudures et les conditions physiques du soudage en temps réel.

Premièrement, les effets des paramètres de procédé dans le soudage par résistance par points ont été évalués. L'étude a été réalisée sur deux nuances d'aciers ; l'acier doux ASTM A36 et l'acier galvanisé ASTM A653. Les échantillons d'aciers ont été soudés en transparence selon des plans factoriels complets prédéfinis. L'analyse micrographique et les essais de dureté de micro-indentations ont révélé la qualité des soudures. Sur la base des résultats de ces essais, des analyses de variance ont été effectuées pour déterminer l'influence des paramètres de soudage sur la géométrie et la dureté des soudures afin d'établir des modèles prédictifs. La méthodologie de surface de réponse a ensuite été utilisée pour relier simultanément la dureté et le diamètre des nœuds de soudure aux paramètres du procédé. On note qu'il y a une augmentation de la dureté de 168 % et 127 % dans la zone de fusion par rapport au métal de base pour l'acier doux A36 et l'acier galvanisé respectivement. Cette augmentation de dureté est due d'une part, à la densification du métal sous l'action de la force de pressage des électrodes, et d'autre part, au phénomène d'auto-trempe du métal sous l'effet de la chaleur. Le courant de soudage est le paramètre le plus influent et contribue pour environ 70% à la géométrie et à la dureté des nœuds de soudure. Le rapport *dureté/diamètre* du noeud (HV/d) peut être utilisé dans la prédiction de la qualité et la résistance globale de la soudure, plus le rapport HV/d est petit, plus la soudure est résistante. Pour les tôles d'acier doux A36, le courant doit être maximisé tandis que la force et le temps de soudage doivent être minimisés,

afin de réduire le rapport HV/d et d'obtenir des soudures de bonne qualité. Pour les tôles d'acier galvanisé, le courant, la force et le temps de soudage doivent être maximisés, afin de réduire le rapport HV/d et d'obtenir des soudures de bonne qualité ; cela est dû à la présence d'un revêtement de zinc sur la surface de contact des tôles galvanisées.

Dans la seconde partie de ce travail, une approche visant à optimiser les paramètres de procédé pour le soudage par résistance par points a été mise sur pied. Elle a permis d'obtenir des paramètres de soudage optimums, qui conduisent à une minimisation de l'énergie de production tout en assurant la bonne résistance mécanique des soudures. L'optimisation des paramètres de procédé a été réalisée à travers l'algorithme génétique NSGA-II. Purement stochastique et basée sur l'évolution génétique, l'approche d'optimisation proposée est plus pratique que les approches déterministes, car elle surmonte le problème d'optimum local et nécessite moins de temps d'exécution. On note que l'acier doux A36 présente une fenêtre de soudabilité plus large que l'acier galvanisé. L'optimisation des paramètres de procédé a entraîné une diminution moyenne du courant de soudage, de la force de pressage des électrodes et du temps de soudage de 10.58%, 13.59% et 32.61% respectivement. L'utilisation de paramètres optimisés conduit non seulement à une réduction de l'énergie de soudage, mais aussi à une augmentation de la durée de vie globale des soudeuses.

Après l'optimisation des paramètres de procédés, la troisième partie de cette étude a fait appel aux outils de modélisation et de simulation. Un modèle couplé électro-thermo-mécano-métallurgique pour le soudage par résistance par points de tôles d'acier AISI 1010 de 2 mm a été développé. À partir de l'évolution de la température, la cinétique de transformation de phases dans le nœud de soudure a été prédite. En raison de la vitesse élevée du processus de soudage, une technique appelée traitement thermique post-soudage (TTPS) a été appliquée afin de réduire la vitesse de refroidissement de la pièce soudée et son effet sur les fractions de phases a été étudié. Des expériences de soudage physique ont été effectuées afin d'évaluer la validité du modèle proposé. Les résultats expérimentaux et de simulation sont concordant, le coefficient de corrélation entre la géométrie des joints soudés obtenue de façon expérimentale et celle obtenue par simulation est d'environ 94%. Dans une soudure

normale d'acier AISI 1010, la transformation dans le nœud de soudure est presque entièrement martensitique. L'application du TTPS a entraîné une augmentation des fractions de bainite et de ferrite et une diminution de la fraction de martensite dans le nœud de soudure. La bainite se forme horizontalement à partir de l'extérieur du nœud tandis que la martensite se forme verticalement à partir du haut et du bas du nœud jusqu'à son centre. L'application du TTPS a un effet significatif sur la géométrie des nœuds de soudure. D'une part, on note une augmentation de 18 % et 9 % de la largeur et de la hauteur des nœuds respectivement. Cela constitue un très grand avantage, car la résistance mécanique des soudures est proportionnelle à leur taille (largeur et hauteur). D'autre part, on note une diminution de 38 % de la largeur de la ZAT des nœuds à leur surface. Cela constitue également un aspect favorable, car plus la ZAT est étroite, plus la soudure est ductile.

La quatrième et dernière partie de cette étude visait à une inspection automatique du procédé de SRP. Il s'agissait d'acquérir des signaux de résistance dynamique lors de l'opération de soudage par résistance par points de tôles minces en acier. Ceci a été fait afin de contrôler le processus en temps réel et de prédire la qualité des soudures. Pour ce faire, les signaux de courant et de tension de soudage ont été acquis à l'aide d'une bobine de Rogowski et de sondes de tension respectivement. Un circuit de conditionnement développé sur une carte MyProto, connecté à un module MyDAQ et contrôlé par la version 2018 du logiciel LabVIEW a permis de représenter les signaux sous forme numérique et de les sauvegarder. Un programme développé sous MATLAB a permis de traiter et d'exploiter ces signaux. La résistance dynamique de toutes les soudures a été obtenue en appliquant la loi d'Ohm aux signaux de courant et de tension de soudage. Une série de soudures a été réalisée en faisant varier le courant de soudage, une représentation de leurs résistances dynamiques a révélé un fuseau de passage. Une théorie a été établie sur la base de ce fuseau de passage : Toute soudure de bonne qualité doit avoir un signal de résistance dynamique qui s'insère dans le fuseau de passage de validation. Afin de valider cette théorie, les signaux de soudures dans lesquelles des défauts ont été délibérément introduits ont été tracés. Aucun de ces signaux ne s'insérait dans le fuseau de passage prédéfini ; ce qui valide la théorie

préétablie. Il est donc possible de déterminer les conditions de soudage et de prédire la qualité des soudures à l'aide de signaux de résistance dynamiques.

L'application des résultats de cette étude mèneront à une augmentation de la viabilité du SRP et à une réduction des coûts de production. Cependant, des travaux futurs permettront de placer le SRP en tête de liste dans le domaine de l'assemblage des carrosseries automobiles. En ce qui concerne la modélisation micro-structurale lors du soudage, il est suggéré de concevoir, implémenter et valider un modèle versatile, capable de gérer des cas de soudage du boron steel et du TRIP steel ; concevoir, implémenter et valider un modèle versatile, capable de gérer des cas de soudage de métaux dissimilaires, et enfin tester ces techniques dans des configurations et conditions industrielles (à grande échelle). Pour ce qui est du volet inspection automatisée à travers la signature de résistance dynamique, il est recommandé de faire des essais répétitifs à l'aide des capteurs plus précis afin d'obtenir un fuseau de passage plus robuste ; concevoir et implémenter une carte mère permettant d'effectuer les opérations d'acquisition et traitement des signaux ; intégrer cette carte aux soudeuses par résistance afin de contrôler, en temps réel, les conditions de soudage et la qualité des soudures par résistance par points. Il est également recommandé d'étendre ces études en incluant plusieurs nuances d'acier.

Bibliographie

[1] Jean Nègre. *Le Soudage électrique par résistance : Soudage par points, soudage à la molette, soudage en bout*. Publ. de la Soudure Autogène, Paris, 5. éd. revue et augmentée edition, 1979. OCLC : 35345159.

[2] Éric Thieblemont. *Modélisation du soudage par résistance par points*. thesis, Vandoeuvre-les-Nancy, INPL, January 1992.

[3] Bobin Xing, Yi Xiao, and Qing H. Qin. Characteristics of shunting effect in resistance spot welding in mild steel based on electrode displacement. *Measurement*, 115 :233 – 242, 2018.

[4] American Institute of Steel Construction. *Steel Construction Manual*. American Institute of Steel Construction, 2017.

[5] Lifang Mei, Jiming Yi, Dongbing Yan, Jinwu Liu, and Genyu Chen. Comparative study on CO2 laser overlap welding and resistance spot welding for galvanized steel. *Materials & Design*, 40 :433–442, September 2012.

[6] S.M. Hamidinejad, F. Kolahan, and A.H. Kokabi. The modeling and process analysis of resistance spot welding on galvanized steel sheets used in car body manufacturing. *Materials & Design*, 34 :759–767, February 2012.

[7] D.S. Mei, D.Q. Li, Z.D. Zhang, and L. Lan. On-line monitoring method for electrode invalidation during spot welding of zinc-coated steel. *Materials Science and Engineering : A*, 499(1-2) :279–281, January 2009.

[8] S. Aslanlar, A. Ogur, U. Ozsarac, E. Ilhan, and Z. Demir. Effect of welding current on mechanical properties of galvanized chromided steel sheets in electrical resistance spot welding. *Materials & Design*, 28(1) :2–7, January 2007.

[9] Ugur Ozsarac. Investigation of Mechanical Properties of Galvanized Automotive Sheets Joined by Resistance Spot Welding. *Journal of Materials Engineering and Performance*, 21(5) :748–755, May 2012.

[10] Xiaomin Luo, Jiangwei Ren, Dong Li, Youqiong Qin, and Peiquan Xu. Macro characteristics of dissimilar high strength steel resistance spot welding joint. *The International Journal of Advanced Manufacturing Technology*, 87(1) :1105–1113, October 2016.

[11] Fatih Hayat and İbrahim Sevim. The effect of welding parameters on fracture toughness of resistance spot-welded galvanized DP600 automotive steel sheets. *The International Journal of Advanced Manufacturing Technology*, 58(9) :1043–1050, February 2012.

[12] S. M. Manladan, F. Yusof, S. Ramesh, and M. Fadzil. A review on resistance spot welding of magnesium alloys. *The International Journal of Advanced Manufacturing Technology*, 86(5) :1805–1825, September 2016.

[13] S. Aslanlar. The effect of nucleus size on mechanical properties in electrical resistance spot welding of sheets used in automotive industry. *Materials & Design*, 27(2) :125 – 131, 2006.

[14] Hongyan Zhang and Jacek Senkara. *Resistance Welding : Fundamentals and Applications, Second Edition*. CRC Press, 2 edition, December 2011.

[15] Mr Niranjan Kumar Singh and Dr Y Vijayakumar. Application of Taguchi method for optimization of resistance spot welding of austenitic stainless steel AISI 301l. 3(10) :15, 2012.

[16] Hamed Pashazadeh, Yousof Gheisari, and Mohsen Hamedi. Statistical modeling and optimization of resistance spot welding process parameters using neural networks and multi-objective genetic algorithm. *Journal of Intelligent Manufacturing*, 27(3) :549–559, June 2016.

[17] R. K. Suresh. Parameter Optimization for Tensile Shear Strength during Spot Welding Of Corrugated Mild Steel Plates. *VSRD International Journal of Mechanical, Civil, Automobile and Production Engineering*, 4 :2319–2208, 2014.

[18] Darshan Shah and Patel P. Dhaval. Prediction of Weld Strength of Resistance Spot Welding Using Artificial Neural Network. *Int. Journal of Engineering Research and Applications*, IV(VII) :2249–8303, July 2014.

[19] Arvinder Singh, Vanraj , and Kant Suman. PARAMETER OPTIMIZATION FOR TENSILE STRENGTH OF SPOT WELD FOR 316l STAINLESS STEEL. *International Journal of Scientific and Engineering Research*, 4, 2013.

[20] A. K. Pandey, M. I. Khan, and K. M. Moeed. Optimization Of Resistance Spot Welding Parameters using Taguchi Method. *International Journal of Engineering Science and Technology (Ijest)*, 5(2) :234–241, February 2013.

[21] P. Zhang, S.X. Li, and Z.F. Zhang. General relationship between strength and hardness. *Materials Science and Engineering : A*, 529 :62–73, November 2011.

[22] Peng-Hsiang Chang and Tso-Liang Teng. Numerical and experimental investigations on the residual stresses of the butt-welded joints. *Computational Materials Science*, 29(4) :511 – 522, 2004.

[23] Francesco Rosalbino, Giorgio Scavino, Giovanni Mortarino, Emma Angelini, and Giancarlo Lunazzi. EIS study on the corrosion performance of a Cr(III)-based conversion coating on zinc galvanized steel for the automotive industry. *Journal of Solid State Electrochemistry*, 15(4) :703–709, April 2011.

[24] Lifang Mei, Dongbing Yan, Genyu Chen, Dang Xie, Mingjun Zhang, and Xiaohong Ge. Comparative study on CO2 laser overlap welding and resistance spot welding for automotive body in white. *Materials & Design*, 78 :107–117, August 2015.

[25] J. M. Sawhill. Spot weldability of high strength sheet steels. *Welding J.*, 59 :19s–31s, 1980.

[26] M. Pouranvari, H. R. Asgari, S. M. Mosavizadch, P. H. Marashi, and M. Goodarzi. Effect of weld nugget size on overload failure mode of resistance spot welds. *Science and Technology of Welding and Joining*, 12(3) :217–225, April 2007.

[27] C. Ma, D.L. Chen, S.D. Bhole, G. Boudreau, A. Lee, and E. Biro. Microstructure and fracture characteristics of spot-welded DP600 steel. *Materials Science and Engineering : A*, 485(1-2) :334–346, June 2008.

[28] ASTM E384-17. Standard Test Method for Microindentation Hardness of Materials. Technical report, ASTM International, West Conshohocken, PA,, 2017.

[29] ASTM E407-07(2015)e1. Practice for Microetching Metals and Alloys. Technical report, ASTM International, West Conshohocken, PA,, 2015.

[30] P. Marashi, M. Pouranvari, S. Amirabdollahian, A. Abedi, and M. Goodarzi. Microstructure and failure behavior of dissimilar resistance spot welds between low carbon galvanized and austenitic stainless steels. *Materials Science and Engineering : A*, 480(1-2) :175–180, May 2008.

[31] B. V. Feujofack Kemda, N. Barka, M. Jahazi, and D. Osmani. Modeling of Phase Transformation Kinetics in Resistance Spot Welding and Investigation of Effect of Post Weld Heat Treatment on Weld Microstructure. *Metals and Materials International*, October 2019.

[32] J E Gould, S P Khurana, and T Li. Predictions of Microstructures when Welding Automotive Advanced High-Strength Steels. page 6, 2006.

[33] M. Goodarzi, S.P.H. Marashi, and M. Pouranvari. Dependence of overload performance on weld attributes for resistance spot welded galvanized low carbon steel. *Journal of Materials Processing Technology*, 209(9) :4379–4384, 2009.

[34] Yahya Bozkurt, Adnan Türker, and Serdar Salman. The Investigation and Comparison of friction stir spot welding and Electrical Resistance Spot Welding of AA2024 Aluminum Alloy Joints. page 7, 2018.

[35] H.T. Sun, X.M. Lai, Y.S. Zhang, and J. Shen. Effect of variable electrode force on weld quality in resistance spot welding. *Science and Technology of Welding and Joining*, 12(8) :718–724, November 2007.

[36] Y. B. Li, D. L. Li, Z. Q. Lin, S. A. David, Z. Feng, and W. Tang. Review : magnetically assisted resistance spot welding. *Science and Technology of Welding and Joining*, 21(1) :59–74, January 2016.

[37] Norasiah Muhammad, Yupiter H. P. Manurung, Mohammad Hafidzi, Sunhaji Kiyai Abas, Ghalib Tham, and Esa Haruman. Optimization and modeling of spot welding parameters with simultaneous multiple response consideration using multi-objective Taguchi method and RSM. *Journal of Mechanical Science and Technology*, 26(8) :2365–2370, August 2012.

[38] John H. Holland. Adaptation in natural and artificial systems Ann Arbor. *The University of Michigan Press*, 1 :975, 1975.

[39] M. Srinivas and L. M. Patnaik. Genetic algorithms : a survey. *Computer*, 27(6) :17–26, June 1994.

[40] Hsien-Yu Tseng. Welding parameters optimization for economic design using neural approximation and genetic algorithm. *The International Journal of Advanced Manufacturing Technology*, 27(9) :897–901, 2006.

[41] B. Li and B. W. Shiu. Principle and Simulation of Fixture Configuration Design for Sheet Metal Assembly with Laser Welding, Part 2 : Optimal Configuration Design with Genetic Algorithm. *The International Journal of Advanced Manufacturing Technology*, 18(4) :276–284, August 2001.

[42] Yusliza Yusoff, Mohd Salihin Ngadiman, and Azlan Mohd Zain. Overview of NSGA-II for Optimizing Machining Process Parameters. *Procedia Engineering*, 15 :3978 – 3983, 2011.

[43] M. Vasudevan, V. Arunkumar, N. Chandrasekhar, and V. Maduraimuthu. Genetic algorithm for optimisation of A-TIG welding process for modified 9cr–1mo steel. *Science and Technology of Welding and Joining*, 15(2) :117–123, February 2010.

[44] A. Kumar and T. DebRoy. Neural network model of heat and fluid flow in gas metal arc fillet welding based on genetic algorithm and conjugate gradient optimisation. *Science and Technology of Welding and Joining*, 11(1) :106–119, February 2006.

[45] K. Deb, A. Pratap, S. Agarwal, and T. Meyarivan. A fast and elitist multiobjective genetic algorithm : NSGA-II. *IEEE Transactions on Evolutionary Computation*, 6(2) :182–197, April 2002.

[46] ASTM E8 / E8M-16a. Test Methods for Tension Testing of Metallic Materials. Technical report, ASTM International, West Conshohocken, PA,, 2016.

[47] D. F. Watt, L. Coon, M. Bibby, J. Goldak, and C. Henwood. An algorithm for modelling microstructural development in weld heat-affected zones (part a) reaction kinetics. *Acta Metallurgica*, 36(11) :3029 – 3035, 1988.

[48] S. A. Gedeon and T. W. Eagar. Resistance spot welding of galvanized steel : Part I. Material variations and process modifications. *Metallurgical Transactions B*, 17(4) :879–885, 1986.

[49] H.C. Lin, C.A. Hsu, C.S. Lee, T.Y. Kuo, and S.L. Jeng. Effects of zinc layer thickness on resistance spot welding of galvanized mild steel. *Journal of Materials Processing Technology*, 251 :205–213, January 2018.

[50] Shiquan Zhou, Lei Liu, Jae Pil Jung, Mok-Young Lee, and Y. Norman Zhou. Effects of welding parameters and surface pretreatments on resistance spot welding of AZ31b Mg alloy. *Metals and Materials International*, 16(6) :967–974, 2010.

[51] Ding Min and Wang Yicheng. Microstructure and properties evaluations of spot-welded ferritic steel sheets via static magnetic field. *Metals and Materials International*, 22(1) :94–100, January 2016.

[52] Insung Hwang, Dongcheol Kim, Munjin Kang, Jae-Hyun Kwak, and Young-Min Kim. Resistance spot weldability of lightweight steel with a high Al content. *Metals and Materials International*, 23(2) :341–349, March 2017.

[53] David Lövenborn. *3D FE Simulations of Resistance Spot Welding*. Student thesis, 2016.

[54] H. Huh and W.J. Kang. Electrothermal analysis of electric resistance spot welding processes by a 3-D finite element method. *Journal of Materials Processing Technology*, 63(1-3) :672–677, January 1997.

[55] Min Jou. Experimental Investigation of Resistance Spot Welding for Sheet Metals Used in Automotive Industry. *JSME International Journal Series C*, 44(2) :544–552, 2001.

[56] Gu-Cheol Kim, Insung Hwang, Munjin Kang, Dongcheol Kim, Hyunsung Park, and Young-Min Kim. Effect of Welding Time on Resistance Spot Weldability of Aluminum 5052 Alloy. *Metals and Materials International*, 25(1) :207–218, January 2019.

[57] M Hamedi and H Pashazadeh. Numerical study of nugget formation in resistance spot welding. 2(1) :5, 2008.

[58] Du-Youl Choi, Ashutosh Sharma, Sang-Ho Uhm, and Jae Pil Jung. Liquid Metal Embrittlement of Resistance Spot Welded 1180 TRIP Steel : Effect of Electrode Force on Cracking Behavior. *Metals and Materials International*, 25(1) :219–228, January 2019.

[59] Tapan Kumar Pal and Kaushik Bhowmick. Resistance Spot Welding Characteristics and High Cycle Fatigue Behavior of DP 780 Steel Sheet. *Journal of Materials Engineering and Performance*, 21(2) :280–285, February 2012.

[60] Ci Li, Xinjian Yuan, Kanglong Wu, Haodong Wang, Zhan Hu, and Xueyu Pan. Nugget formation and its mechanism of resistance spot welded joints in DP600 dual-phase and DC54d ultralow carbon steel. *Metals and Materials International*, 23(3) :543–553, May 2017.

[61] Mustafa Taskin, Ugur Caligulu, and Sedat Kolukisa. The Effect of Welding Speed on the Laser Welding of AISI 430 Ferritic Stainless—AISI 1010 Low-Carbon Steel. *Practical Metallography*, 46(11) :598–608, November 2009.

[62] Edgar López-Martínez, Octavio Vázquez-Gómez, Héctor Javier Vergara-Hernández, Sergio Serna, and Bernardo Campillo. Mechanical characterization of the welding of two experimental HSLA steels by microhardness and nanoindentation tests. *Metals and Materials International*, 22(6) :987–994, November 2016.

[63] Hyunbin Nam, Chulho Park, Cheolhee Kim, Hyoungseop Kim, and Namhyun Kang. Effect of post weld heat treatment on weldability of high entropy alloy welds. *Science and Technology of Welding and Joining*, 23(5) :420–427, July 2018.

[64] A. R. Jahandideh, M. Hamedi, S. A. Mansourzadeh, and A. Rahi. An experimental study on effects of post-heating parameters on resistance spot welding of SAPH440 steel. *Science and Technology of Welding and Joining*, 16(8) :669–675, 2011.

[65] W. L. Chuko and J. E. Gould. Development of appropriate resistance spot welding practice for transformation-hardened steels. *Weld. J*, 81(1) :1s–8s, 2002.

[66] I. Khan, Michael L. Kuntz, Y. Zhou, K. Chan, and N. Scotchmer. Monitoring the Effect of RSW Pulsing on AHSS using FEA (SORPAS) Software. Technical report, SAE Technical Paper, 2007.

[67] C. T. Lane, C. D. Sorensen, G. B. Hunter, S. Gedeon, and T. W. Eagar. Cinematography of resistance spot welding of galvanized steel sheet. *Weld. J.*, 66(9) :260, 1987.

[68] S. H. Arabi, M. Pouranvari, and M. Movahedi. Pathways to improve the austenite–ferrite phase balance during resistance spot welding of duplex stainless steels. *Science and Technology of Welding and Joining*, 24(1) :8–15, January 2019.

[69] VH Baltazar Hernandez, Y. Okita, and Y. Zhou. Second pulse current in resistance spot welded TRIP steel—Effects on the microstructure and mechanical behavior. *impulse*, 91, 2012.

[70] Chris V Nielsen, Wenqi Zhang, William Perret, Paulo AF Martins, and Niels Bay. Three-dimensional simulations of resistance spot welding. *Proceedings of the Institution of Mechanical Engineers, Part D : Journal of Automobile Engineering*, 229(7) :885–897, June 2015.

[71] M. Jafari Vardanjani, A. Araee, J. Senkara, J. Jakubowski, and J. Godek. Experimental and numerical analysis of shunting effect in resistance spot welding of Al2219 sheets. *Bulletin of the Polish Academy of Sciences Technical Sciences*, 64(2) :425–434, June 2016.

[72] M. Venkatraman, O. N. Mohanty, and R. N. Ghosh. Modelling of transformation kinetics in HSLA 100 steel during continuous cooling. *Scandinavian Journal of Metallurgy*, 30(1) :8–13, February 2001.

[73] P. R. Woodard, S. Chandrasekar, and H. T. Y. Yang. Analysis of temperature and microstructure in the quenching of steel cylinders. *Metallurgical and Materials Transactions B*, 30(4) :815, 1999.

[74] Wendell Porto de Oliveira, Marcelo Amorim Savi, Pedro Manuel Calas Lopes Pacheco, and Luís Felipe Guimarães de Souza. Thermomechanical analysis of steel cylinders quenching using a constitutive model with diffusional and non-diffusional phase transformations. *Mechanics of Materials*, 42(1) :31–43, January 2010.

[75] W. Piekarska, M. Kubiak, and A. Bokota. Numerical Simulation of Thermal Phenomena and Phase Transformations in Laser-Arc Hybrid Welded Joints. *Archives of Metallurgy and Materials*, 56(2), January 2011.

[76] J. Trzaska and L.A. Dobrzański. Modelling of CCT diagrams for engineering and constructional steels. *Journal of Materials Processing Technology*, 192-193 :504–510, October 2007.

[77] Comsol. AC/DC Module, 2015.

[78] William H. Hayt and John A. Buck. *Engineering electromagnetics*. McGraw-Hill series in electrical engineering. McGraw-Hill Higher Education, Boston, 7th ed edition, 2006.

[79] Edward J. Rothwell and Michael J. Cloud. *Electromagnetics*. CRC Press, Taylor & Francis Group, Boca Raton, third edition edition, 2018.

[80] David K Cheng. *Field and wave electromagnetics*. Tsinghua University Press, Beijing, 2007. OCLC : 660961466.

[81] Yong Bing Li, Zhong Qin Lin, S. Jack Hu, and Guan Long Chen. Numerical analysis of magnetic fluid dynamics behaviors during resistance spot welding. *Journal of Applied Physics*, 101(5) :053506, March 2007.

[82] H S Chang and H S Cho. A Study on the Shunt Effect in Resistance Spot Welding. page 11.

[83] Euiwhan Kim and Thomas W. Eagar. Simulation and sensitivity analysis of controlling parameters in resistance spot welding. *Metals and Materials International*, 21(2) :356–364, March 2015.

[84] Chon L. Tsai, Weng L. Dai, and David W. Dickinson. Analysis and Development of A Real-Time Control Methodology in Resistance Spot Welding. *SAE Transactions*, 100 :158–176, 1991.

[85] Mohsen Hamedi, Hamid Eisazadeh, and Mousa Esmailzadeh. Numerical simulation of tensile strength of upset welded joints with experimental verification. *Materials & Design (1980-2015)*, 31(5) :2296–2304, May 2010.

[86] Jos Vander Sloten, Pascal Verdonck, Marc Nyssen, Jens Haueisen, R. Magjarevic, and J. H. Nagel, editors. *4th European Conference of the International Federation for Medical and Biological Engineering*, volume 22 of *IFMBE Proceedings*. Springer Berlin Heidelberg, Berlin, Heidelberg, 2009.

[87] William S. Slaughter. *The Linearized Theory of Elasticity*. Birkhäuser Boston, Boston, MA, 2002.

[88] Yavuz Başar and Dieter Weichert. *Nonlinear continuum mechanics of solids : fundamental mathematical and physical concepts*. Springer, Berlin [etc., 2010. OCLC : 781067114.

[89] V. A. Goldade, Serge Shilko, and A. S. Neverov. *Smart materials taxonomy*. CRC Press, Taylor & Francis Group, Boca Raton, 2016.

[90] Raymond Kwesi Nutor. Using the Hollomon Model to Predict Strain-Hardening in Metals. *American Journal of Materials Synthesis and Processing*, 2(1) :1, 2017.

[91] John H. Hollomon. Tensile deformation. *Aime Trans*, 162(4) :268–290, 1945.

[92] Serope Kalpakjian, Steven R. Schmid, and Hamidon Musa. *Manufacturing engineering and technology*. Prentice Hall, Singapore, 6. ed. in si units edition, 2010. OCLC : 503257924.

[93] Ray M. Bowen. *Introduction to continuum mechanics for engineers*. Number 39 in Mathematical concepts and methods in science and engineering. Plenum Press, New York, 1989.

[94] Melvin Avrami. Kinetics of Phase Change. II Transformation-Time Relations for Random Distribution of Nuclei. *The Journal of Chemical Physics*, 8(2) :212–224, February 1940.

[95] T. Domański and A. Bokota. Numerical Models of Hardening Phenomena of Tools Steel Base on the TTT and CCT Diagrams. *Archives of Metallurgy and Materials*, 56(2) :325–344, June 2011.

[96] Fang Zhang and Feng-shan Du. A Model for Prediction of Phase Transformation during Quenching of Steel. In *2008 International Symposium on Information Science and Engineering*, pages 431–435, Shanghai, December 2008. IEEE.

[97] C. Verdi and A. Visintin. A mathematical model of the austenite-pearlite transformation in plain carbon steel based on the Scheil's additivity rule. *Acta Metallurgica*, 35(11) :2711–2717, November 1987.

[98] D.P. Koistinen and R.E. Marburger. A general equation prescribing the extent of the austenite-martensite transformation in pure iron-carbon alloys and plain carbon steels. *Acta Metallurgica*, 7(1) :59–60, January 1959.

[99] Fei Huyan, Peter Hedström, Lars Höglund, and Annika Borgenstam. A Thermodynamic-Based Model to Predict the Fraction of Martensite in Steels. *Metallurgical and Materials Transactions A*, 47(9) :4404–4410, September 2016.

[100] George F. Vander Voort, editor. *Atlas of time-temperature diagrams for irons and steels*. Materials data series. ASM International, United States, 1991.

[101] Philip D. Harvey and American Society for Metals, editors. *Engineering properties of steel*. American Society for Metals, Metals Park, Ohio, 1982.

[102] Marlene Spittel, Thilo Spittel, Hans Warlimont, Hans Landolt, Richard Börnstein, and Werner Martienssen. *Numerical data and functional relationships in science and technology : new series. Group 8 Vol. 2 Subvol. C Pt. 1 : Advanced materials and technologies Materials Metal forming data Ferrous alloys*. Springer, Berlin, 2009. OCLC : 436284132.

[103] M. Zidek, V. Dedek, and B. Sommer. *Tvareni oceli*. SNTL, Praha, 1988.

[104] United States and Department of Defense. *Composite materials handbook*. U.S. Dept. of Defense, Washington, D.C., 2002. OCLC : 63763185.

[105] Howard E. Boyer, Timothy L. Gall, and American Society for Metals, editors. *Metals handbook*. American Society for Metals, Metals Park, Ohio, desk ed edition, 1984.

[106] ASM Speciality Handbook. Copper and Copper alloys. *Davis & Associated, USA*, page 14, 2001.

[107] ISO 5821 :2009. Resistance welding — Spot welding electrode caps. Technical report, International Organization for Standardization, Geneva, February 2009.

[108] G. E Linnert. *Welding metallurgy*. American Welding Society, 1994. OCLC : 643133648.

[109] ISO 14373 :2015(en). Resistance welding — Procedure for spot welding of uncoated and coated low carbon steels. Technical Report IIW, International Organization for Standardization, March 2015.

[110] Osayande Lord-Rufus Ighodaro, Elliot Biro, and Y. Norman Zhou. Study and Applications of Dynamic Resistance Profiles During Resistance Spot Welding of Coated Hot-Stamping Steels. *Metallurgical and Materials Transactions A*, 48(2) :745–758, 2017.

[111] D W Dickinson. Characterization of Spot Welding Behavior by Dynamic Electrical Parameter Monitoring. page 7, 1980.

[112] W. F. Savage, E. F. Nippes, and F. A. Wassell. Dynamic contact resistance of series spot welds. *Welding Journal*, 57(2) :43s–50s, 1978.

[113] S. A. Gedeon, C. D. Sorensen, K. T. Ulrich, and T. W. Eagar. Measurement of dynamic electrical and mechanical properties of resistance spot welds. *Welding Journal*, 66(12) :378–385, 1987.

[114] S. C. Wang and P. S. Wei. Modeling Dynamic Electrical Resistance During Resistance Spot Welding. *Journal of Heat Transfer*, 123(3) :576–, 2001.

[115] W Tan, Y Zhou, H W Kerr, and S Lawson. A study of dynamic resistance during small scale resistance spot welding of thin Ni sheets. *Journal of Physics D : Applied Physics*, 37(14) :1998–2008, July 2004.

[116] Yongbing Li and XianFeng Wang. *Online Monitoring the Quality of AC Resistance Spot Welding Using Electrode Vibration Signals*. 2012.

[117] Yanhua Ma, Pei Wu, Chuanzhong Xuan, Yongan Zhang, and He Su. Review on Techniques for On-Line Monitoring of Resistance Spot Welding Process. *Advances in Materials Science and Engineering*, 2013 :1–6, 2013.

[118] S. Chen, T. Sun, X. Jiang, J. Qi, and R. Zeng. Online monitoring and evaluation of the weld quality of resistance spot welded titanium alloy. *Journal of Manufacturing Processes*, 23 :183–191, August 2016.

[119] Toroidal Coil.

[120] J. Cooper. On the high-frequency response of a Rogowski coil. *Journal of Nuclear Energy. Part C, Plasma Physics, Accelerators, Thermonuclear Research*, 5(5) :285, 1963.

[121] Donald G. Pellinen, Marco S. Di Capua, Stephen E. Sampayan, Harold Gerbracht, and Ming Wang. Rogowski coil for measuring fast, high-level pulsed currents. *Review of Scientific Instruments*, 51(11) :1535–1540, 1980.

[122] Mohammad Hamed Samimi, Arash Mahari, Mohammad Ali Farahnakian, and Hossein Mohseni. The Rogowski Coil Principles and Applications : A Review. *IEEE Sensors Journal*, 15(2) :651–658, February 2015.

[123] Hongjie Zhang, Fujun Wang, Tao Xi, Jian Zhao, Lijing Wang, and Weiguo Gao. A novel quality evaluation method for resistance spot welding based on the electrode displacement signal and the Chernoff faces technique. *Mechanical Systems and Signal Processing*, 62-63 :431–443, October 2015.

[124] Todd K. Moon and Wynn C. Stirling. *Mathematical methods and algorithms for signal processing*, volume 1. Prentice hall Upper Saddle River, NJ, 2000.

Annexe A

Code MATLAB de l'algorithme génétique (NSGA - II) implémenté pour l'optimisation des paramètres de procédé - Article 2

A.1 Programme principal

```
% ------------------------------------------------------------------------- %
% Function main_optimization.m, which performs a Non Sorting Genetic       %
% Algorithm II (NSGA-II), based on Deb2002.                                 %
% ------------------------------------------------------------------------- %
%   Author:  Bleriot Feujofack                                              %
%   Date:    09/04/2019                                                     %
%   E-mail:  f.bleriotvincent (at) yahoo (dot) fr                           %
% ------------------------------------------------------------------------- %
%   References:                                                             %
%    [1] Deb, K., Pratap, A., Agarwal, S., & Meyarivan, T. A. M. T. (2002)%
%        A fast and elitist multiobjective genetic algorithm: NSGA-II.      %
%        IEEE transactions on evolutionary computation, 6(2), 182-197.      %
% ------------------------------------------------------------------------- %
clear all; clc; close all;
inf=1;
while inf==1
 clear all;
    inf=1;
prompt='\n #Enter_set_code\n';
set_code=input(prompt);
set_code_num=set_code;
switch set_code
    case 1
        f1 = @(I,F,t) t.*I.^2;
        f2 = @(I,F,t) F;
```

```
        MultiObj.fun = @(x) [f1(x(:,1),x(:,2),x(:,3)), f2(x(:,1),x(:,2),x(:,3))];
        MultiObj.nVar = 3;
        MultiObj.var_min = [5000, 100, 150];
        MultiObj.var_max = [7000, 200, 300];
        Tresh=28.63;
        set_code=num2str(set_code);
        Name=strcat('A36S',set_code);
        copyfile('R_A36S1.m','constr_funct.m');
    case 2
        f1 = @(I,F,t) t.*I.^2;
        f2 = @(I,F,t) F;
        MultiObj.fun = @(x) [f1(x(:,1),x(:,2),x(:,3)), f2(x(:,1),x(:,2),x(:,3))];
        MultiObj.nVar = 3;
        MultiObj.var_min = [7000, 250, 250];
        MultiObj.var_max = [8500, 350, 400];
        Tresh=22.53;
        set_code=num2str(set_code);
        Name=strcat('A36S',set_code);
        copyfile('R_A36S2.m','constr_funct.m');
    case 3
        f1 = @(I,F,t) t.*I.^2;
        f2 = @(I,F,t) F;
        MultiObj.fun = @(x) [f1(x(:,1),x(:,2),x(:,3)), f2(x(:,1),x(:,2),x(:,3))];
        MultiObj.nVar = 3;
        MultiObj.var_min = [7500, 200, 300];
        MultiObj.var_max = [9500, 400, 500];
        Tresh=8.68;
        set_code=num2str(set_code-2);
        Name=strcat('ZnS',set_code);
        copyfile('R_ZnS1.m','constr_funct.m');
    case 4
        f1 = @(I,F,t) t.*I.^2;
        f2 = @(I,F,t) F;
        MultiObj.fun = @(x) [f1(x(:,1),x(:,2),x(:,3)), f2(x(:,1),x(:,2),x(:,3))];
        MultiObj.nVar = 3;
        MultiObj.var_min = [8000, 350, 350];
        MultiObj.var_max = [10000, 450, 650];
        Tresh=4.65;
        set_code=num2str(set_code-2);
        Name=strcat('ZnS',set_code);
        copyfile('R_ZnS2.m','constr_funct.m');
end
params.Np = 500;        % Population size
params.pc = 0.9;
```

```
70 params.pm = 0.1;
71 params.maxgen = 100;     % Maximum number of generations
72 params.lim = Tresh;
73 [Rep,Fit]=NSGAII(params,MultiObj);
74     xlswrite(Name,Rep,1);
75     A=MultiObj.var_min;
76     B=MultiObj.var_max;
77     for i=1:MultiObj.nVar
78     Gain(i)=100*(B(i)-Rep(1,i))./Rep(1,i);
79     end
80     Gain(4)=100*((B(1)^2)*(B(3))-(Rep(1,1)^2)*(Rep(1,3)))/((Rep(1,1)^2)
81     *(Rep(1,3)));
82     xlswrite(Name,Gain,2);
83     xlswrite('Convergence',Fit,set_code_num);
84
85 end
```

A.2 Algorithme génétique (NSGA-II)

```
% ------------------------------------------------------------------------- %
% Function NSGAII performs a Non Sorting Genetic Algorithm-II over conti- %
% nous functions.                                                           %
%                                                                           %
%   Input parameters:                                                       %
%       - params:   Struct that contains the customized parameters.         %
%           * params.Np:        Number of chromosomes in the population.    %
%           * params.maxgen:    Maximum number of generations.              %
%           * params.pc:        Probability of crossover.                   %
%           * params.pm:        Probability of mutation.                    %
%       - MultiObj: Struct that contains the parameters relative to the     %
%                   optimization functions.                                 %
%           * MultiObj.fun:     Anonymous multi-obj function to minimize.   %
%           * MultiObj.nVar:    Number of variables.                        %
%           * MultiObj.var_min: Vector that indicates the minimum values    %
%                               of the search space in each dimension.      %
%           * MultiObj.var_max: Same than 'var_min' with the maxima.        %
% ------------------------------------------------------------------------- %
%   For an example of use, run 'main_optimization.m'.                       %
% ------------------------------------------------------------------------- %
%   Author:  Bleriot Feujofack                                              %
%   Date:    09/04/2019                                                     %
%   E-mail:  f.bleriotvincent (at) yahoo (dot) fr                           %
%           - 1.0:  Initial version (22/02/2019).                           %
%           - 1.1:  Fast Non Sorting Algorithm is now vectorized for im-    %
%                   proving the performance (much less computation time)    %
%                   (09/04/2019).                                           %
% ------------------------------------------------------------------------- %
%   References:                                                             %
%    [1] Deb, K., Pratap, A., Agarwal, S., & Meyarivan, T. A. M. T. (2002)%
%        A fast and elitist multiobjective genetic algorithm: NSGA-II.      %
%        IEEE transactions on evolutionary computation, 6(2), 182-197.      %
% ------------------------------------------------------------------------- %
function [Rep,Fit]=NSGAII(params,MultiObj)

    % Parameters
    Np      = params.Np;        % Number of chromosomes in the population
    maxgen  = params.maxgen;    % Maximum number of generations
    pc      = params.pc;        % Probability of crossover
    pm      = params.pm;        % Probability of mutation
    fun     = MultiObj.fun;     % Objective function
    nVar    = MultiObj.nVar;    % Number of variables (dimensions or objectives)
```

```
43      var_min = MultiObj.var_min(:);  % Minimum value for each gen
44      var_max = MultiObj.var_max(:);  % Maximum value for each gen
45      tresh   = params.lim;
46
47      % Initialization
48      gen   = 1;
49       for i=1:Np
50          POS1=(var_max-var_min)'.*rand(1,nVar)+var_min';
51          while (constr_funct(POS1(1),POS1(2),POS1(3))>tresh)
52
53      POS1=(var_max-var_min)'.*rand(1,nVar)+var_min';
54          end
55          POS(i,:)=POS1;
56      end
57      P=repmat(POS,1);
58  %     P     = repmat((var_max-var_min)',Np,1).*rand(Np,nVar)
59  + repmat(var_min',Np,1);
60      Pfit  = fun(P);
61      Prank = FastNonDominatedSorting_Vectorized(Pfit);
62      [P,~] = selectParentByRank(P,Prank);
63      Q = applyCrossoverAndMutation(P,pc,pm,var_max,var_min,tresh);
64
65      % Plotting and verbose
66      if(size(Pfit,2) == 2)
67          h_fig = figure(1);
68          h_par=scatter(Pfit(:,1),Pfit(:,2),20,'filled', 'markerFaceAlpha',0.3,
69          'MarkerFaceColor',[100 150 200]./255,'HandleVisibility','off'); hold on;
70          h_rep = plot(Pfit(:,1),Pfit(:,2),'ok','HandleVisibility','off'); hold on;
71          grid on;
72  %         xlabel('f1'); ylabel('f2');
73          drawnow;
74          axis square;
75      end
76      if(size(Pfit,2) == 3)
77          h_fig = figure(1);
78          h_rep = plot3(Pfit(:,1),Pfit(:,2),Pfit(:,3),'ok'); hold on;
79          grid on; xlabel('f1'); ylabel('f2'); zlabel('f3');
80          drawnow;
81          axis square;
82      end
83      display(['Generation #' num2str(gen) ' - First front size: '
84      num2str(sum(Prank==1))]);
85  xlabel('Obj. function 1 (I^2\cdot t)','Fontsize',9);
86  ylabel('Obj. function 2 (F)','Fontsize',9);
```

```
Title=strcat('Pareto frontier');
title(Title, 'Fontsize',10);
legend('location','southeast');
set(findobj(gcf,'type','axes'),'FontName','Arial','FontSize',12);
  LSA=strcat('Generation #', num2str(gen)');
  LSB=strcat('First front size: ', num2str(sum(Prank==1)));
% LSC=strcat('Specimen C || (Mode ',' - ', RML,') ');
lgd=legend(LSA,LSB);
lgd.FontSize = 12;
newfilen1=fullfile(inpath,filen1);
print(newfilen1,'-dpng','-r1200');
print(newfilen1,'-djpeg','-r1200');
print(newfilen1,'-dpdf');
print(newfilen1,'-dmeta');
    % Main NSGA-II loop
    stopCondition = false;
    while ¬stopCondition
        % Merge the parent and the children
        R = [P; Q];
        % Compute the new Pareto Fronts
        Rfit = fun(R);
        Rrank = FastNonDominatedSorting_Vectorized(Rfit);

        % Plotting and verbose
        if(size(Rfit,2) == 2)
            figure(h_fig); delete(h_rep);
            h_par=scatter(Rfit(1:Np,1),Rfit(1:Np,2),20,'filled', 'markerFaceAlpha'
            ,0.3,'MarkerFaceColor',[100 150 200]./255,'HandleVisibility','off');
            hold on;
            h_rep = plot(Rfit(1:Np,1),Rfit(1:Np,2),'ok','HandleVisibility','off');
            hold on;
            if(isfield(MultiObj,'truePF'))
                try delete(h_pf); end
 h_pf = plot(MultiObj.truePF(:,1),MultiObj.truePF(:,2),'.','color',0.8.*ones(1,3));
 hold on;
            end
            grid on;
%             xlabel('f1'); ylabel('f2');
            drawnow;
            axis square;
        end
        if(size(Rfit,2) == 3)
            figure(h_fig); delete(h_rep);
            h_rep = plot3(Rfit(1:Np,1),Rfit(1:Np,2),Rfit(1:Np,3),'ok'); hold on;
```

```
            if(isfield(MultiObj,'truePF'))
                try delete(h_pf); end
                h_pf = plot3(MultiObj.truePF(:,1),MultiObj.truePF(:,2),
                MultiObj.truePF(:,3),'.','color',0.8.*ones(1,3)); hold on;
            end
            grid on; xlabel('f1'); ylabel('f2');
            drawnow;
            axis square;
        end
        display(['Generation #' num2str(gen) ' - First front size: '
        num2str(sum(Rrank==1))]);
        Fity1(gen)=.5*sum(Rfit(:,1))./Np;
        Fity2(gen)=.5*sum(Rfit(:,2))./Np;
        Fit=[Fity1;Fity2]';
    hold on
    plot(nan,nan,'-w',nan,nan,'ow',nan,nan,'ow');
        xlabel(' Energy (mJ/\Omega)','fontweight','bold','Fontsize',11);
ylabel(' Force (daN)','fontweight','bold','Fontsize',11);
hold on
gen1=num2str(gen);
ffs= num2str(sum(Rrank==1));
pop= num2str(2*Np);
title('Pareto frontier' ,'FontName','Helvetica','FontSize',12);
legend('location','northeast');
  LSA=strcat('Generation # ','\color{white}AAI','\color{black}',gen1);
  LSB=strcat('First front size','\color{white}AIi','\color{black}',ffs );
  LSC=strcat('Population size','\color{white}A', '\color{black}',pop);
lgd=legend( LSA, LSB, LSC);
lgd.FontSize = 9;
set(findobj(gcf,'type','axes'),'FontName','Helvetica','Fontsize',11);
if ismember(gen,[1,5,10,20,30,40,50,100])
%  print(num2str(gen),'-dpng','-r300');
 print(num2str(gen),'-dmeta');
print(num2str(gen),'-dpdf');

end
         % Sort by rank
        [Rrank,idx] = sort(Rrank,'ascend');
        Rfit = Rfit(idx,:);
        R = R(idx,:);
                % Compute the crowding distance index
        [Rcrowd,Rrank,~,R] = crowdingDistances(Rrank,Rfit,R);

        % Select Parent
```

```
175         P = selectParentByRankAndDistance(Rcrowd,Rrank,R);
176                 % Compute child
177         Q = applyCrossoverAndMutation(P,pc,pm,var_max,var_min,tresh);
178 %           Rep=P;
179 %         P
180         % Increment generation
181         gen = gen + 1;
182         if(gen>maxgen), stopCondition = true; end
183     end
184   Rep=P;
185   %     %Plotting fitness
186         figure(2)
187         genx=1:gen-1;
188   xlim([1,gen-1]);
189         plot(genx, Fity1,'-b','LineWidth',1.15,'HandleVisibility','off');
190     grid on
191 xlabel('Generations','fontweight','bold','Fontsize',11,'FontName','Helvetica');
192 ylabel('Average Energy  - mJ/\Omega','fontweight','bold','Fontsize',11,
193 'FontName','Helvetica');
194 title('Convergence plot - Energy', 'Fontsize',12);
195     hold on
196     plot(nan,nan,'-w',nan,nan,'ow',nan,nan,'ow');
197 legend('location','northeast');
198    LSA=strcat('Population size','\color{white}.......', '\color{black}',pop);
199    LSB =strcat('Prob. of crossover','\color{white}..','\color{black}',num2str(pc) );
200    LSC =strcat('Prob. of mutation  ','\color{white}....','\color{black}',
201    num2str(pm));
202   lgd=legend(LSA, LSB, LSC);
203 lgd.FontSize = 9;
204 set(findobj(gcf,'type','axes'),'FontName','Helvetica','Fontsize',11);
205  print(num2str(gen+10),'-dpng','-r300');
206  print(num2str(gen+10),'-dmeta');
207  print(num2str(gen+10),'-dpdf');
208
209 %           %Plotting fitness
210         figure(3)
211         genx=1:gen-1;
212       xlim([1,gen-1]);
213         plot(genx, Fity2,'-b','LineWidth',1.15,'HandleVisibility','off');
214   grid on
215                         xlabel('Generations','fontweight','bold','Fontsize',11);
216 ylabel('Average Force - daN','fontweight','bold','Fontsize',11);
217 title('Convergence plot - Force', 'Fontsize',12);
218     hold on
```

```
    plot(nan,nan,'-w',nan,nan,'ow',nan,nan,'ow');
legend('location','southeast');
   LSA=strcat('Population size','\color{white}.......', '\color{black}',pop);
   LSB =strcat('Prob. of crossover','\color{white}..','\color{black}',num2str(pc) );
   LSC =strcat('Prob. of mutation  ','\color{white}....','\color{black}',
   num2str(pm));
lgd=legend(LSA, LSB, LSC);
lgd.FontSize = 9;

set(findobj(gcf,'type','axes'),'FontName','Helvetica','Fontsize',11);
 print(num2str(gen+20),'-dmeta');
 print(num2str(gen+20),'-dpng','-r300');
 print(num2str(gen+20),'-dpdf');
end

% Function that selects a new parent based on the crowding distance
% operator
function [newParent] = selectParentByRankAndDistance(Rcrowd,Rrank,R)
    % Initialization
    N = length(Rcrowd)/2;
    Npf = length(unique(Rrank));
    newParent = zeros(N,size(R,2));
    % Selecting the chromosomes
    pf = 1;
    numberOfSolutions = 0;
    while pf ≤ Npf
        % If there is enough space, select solutions based on rank
        if numberOfSolutions + sum(Rrank == pf) ≤ N
            newParent(numberOfSolutions+1:numberOfSolutions+sum(Rrank == pf),:)
            = R(Rrank == pf,:);
            numberOfSolutions = numberOfSolutions + sum(Rrank == pf);
        % If there isn't enugh space, sort by crowding distances
        else
            rest = N - numberOfSolutions;
            lastPF = R(Rrank == pf,:);
            lastPFdist = Rcrowd(Rrank == pf);
            [¬,idx] = sort(lastPFdist,'descend');
            lastPF = lastPF(idx,:);
            try
            newParent(numberOfSolutions+1:numberOfSolutions+rest,:)
            = lastPF(1:rest,:);
            catch
                display('');
            end
```

```
263             numberOfSolutions = numberOfSolutions + rest;
264         end
265         pf = pf + 1;
266     end
267 end
268 
269 % Function that computes the crowding distances of every single ParetoFront
270 function [sortCrowd,sortRank,sortFit,sortPop]=crowdingDistances(rank,fitness,pop)
271 
272     % Initialize
273     sortPop = [];
274     sortFit = [];
275     sortRank = [];
276     sortCrowd = [];
277 
278     Npf = length(unique(rank));
279     for pf = 1:1:Npf
280         index = find(rank==pf);
281         temp_fit = fitness(index,:);
282         temp_rank = rank(index,:);
283         temp_pop = pop(index,:);
284 
285         % Sort by first dimension
286         [temp_fit,sort_idx] = sortrows(temp_fit,1);
287         temp_rank = temp_rank(sort_idx);
288         sortFit = [sortFit; temp_fit];
289         sortRank = [sortRank; temp_rank];
290         sortPop = [sortPop; temp_pop(sort_idx,:)];
291 
292         % Crowded distances
293         temp_crowd = zeros(size(temp_rank));
294         for m = 1:1:size(fitness,2)
295             temp_max = max(temp_fit(:,m));
296             temp_min = min(temp_fit(:,m));
297             for l = 2:1:length(temp_crowd)-1
298                 temp_crowd(l) = temp_crowd(l) + (abs(temp_fit(l-1,m)
299                 -temp_fit(l+1,m)))./(temp_max-temp_min);
300             end
301         end
302         temp_crowd(1) = Inf;
303         temp_crowd(length(temp_crowd)) = Inf;
304         sortCrowd = [sortCrowd; temp_crowd];
305     end
306 end
```

```
307
308 % Function that calculates a child population by applying crossover and mutation
309 function Q = applyCrossoverAndMutation(parent,pc,pm,var_max,var_min,tresh)
310     % Params
311     N = size(parent,1);
312     nVar = size(parent,2);
313     % Child initialization
314     Q = parent;
315     % Crossover
316     cross_idx = rand(N,1) < pc;%Random elements with probability of
317     non zeros < Crossover probability
318     cross_idx = find(cross_idx);%Find non zero
319     for c = 1:1:length(cross_idx)
320         selected = randi(N,1,1);
321         while selected == c
322             selected = randi(N,1,1);
323         end
324         cut = randi(nVar,1,1);
325         Q(c,:) = [parent(c,1:cut), parent(selected,cut+1:nVar)];
326         while  (constr_funct(Q(c,1),Q(c,2),Q(c,3))>tresh)
327             selected = randi(N,1,1);
328         while selected == c
329             selected = randi(N,1,1);
330         end
331         cut = randi(nVar,1,1);
332         Q(c,:) = [parent(c,1:cut), parent(selected,cut+1:nVar)];
333         end
334     end
335
336     % Mutation
337     mutatedPop = repmat((var_max-var_min)',N,1).*rand(N,nVar)
338     + repmat(var_min',N,1);
339       mut_idx = rand(N,nVar) < pm;
340       POSm=zeros(N,nVar);
341       [r,c]=find(mut_idx);
342      for i=1:length(r)
343          ii=r(i);
344         POSmut=(var_max-var_min)'.*rand(1,nVar)+var_min';
345         POSm(ii,:)=POSmut;
346         mutatedPop=repmat(POSm,1);
347          Q(mut_idx) = mutatedPop(mut_idx);
348         while  (constr_funct(Q(ii,1),Q(ii,2),Q(ii,3))>tresh)
349        POSmut=(var_max-var_min)'.*rand(1,nVar)+var_min';
350         POSm(ii,:)=POSmut;
```

```
351          mutatedPop=repmat(POSm,1);
352           Q(mut_idx) = mutatedPop(mut_idx);
353          end
354      end
355
356  %       mut_idx = rand(N,nVar) < pm;
357  %
358  %       for i=1:N
359  %          POSmut=(var_max-var_min)'.*rand(1,nVar)+var_min';
360  %          POSm(i,:)=POSmut;
361  %      end
362  %       mutatedPop=repmat(POSm,1);
363  %      Q(mut_idx) = mutatedPop(mut_idx);
364  %       for k=1:N
365  % while  (constr_funct(Q(k,1),Q(k,2),Q(k,3))>tresh)
366  %                         for i=1:N
367  %          POSmut=(var_max-var_min)'.*rand(1,nVar)+var_min';
368  %
369  %          POSm(i,:)=POSmut;
370  %      end
371  %       mutatedPop=repmat(POSm,1);
372  %       Q(mut_idx) = mutatedPop(mut_idx);
373  %
374  %                 end
375  %       end
376  %
377  end
378  % Function that performs a binary tournament selection and extracts one
379  % parent from the initial population based on their ranks.
380  function [P1,P1rank]   = selectParentByRank(P, Prank)
381      % Take the couples
382      N = length(Prank);
383      left_idx  = randi(N,N,1);
384      right_idx = randi(N,N,1);
385      while sum(left_idx==right_idx)>0
386          right_idx(left_idx==right_idx) = randi(N,sum(left_idx==right_idx),1);
387      end
388
389      % Make the tournament
390      winners = zeros(N,1);
391      winners(Prank(left_idx)≤Prank(right_idx))
392      = left_idx(Prank(left_idx)≤Prank(right_idx));
393      winners(Prank(right_idx)<Prank(left_idx))
394      = right_idx(Prank(right_idx)<Prank(left_idx));
```

```
395
396         % Select both populations
397     P1 = P(winners,:);
398     P1rank = Prank(winners,:);
399 end
400 % Funtion that performs a Fast Non Dominated Sorting algorithm of the input
401 % fitnesses. Note: the code is not vectorized, its programming is just
402 % based on Deb2002.
403 function [RANK] = FastNonDominatedSorting_Loop(fitness)
404     % Initialization
405     Np = size(fitness,1);
406     N = zeros(Np,1);
407     S{Np,1} = [];
408     PF{Np,1} = [];
409     RANK = NaN(Np,1);
410         % Main algorithm
411     for p_idx = 1:1:Np
412         p = fitness(p_idx,:);
413         for q_idx = 1:1:Np
414             q = fitness(q_idx,:);
415             if dominates(p,q)
416                 S{p_idx,1} = [S{p_idx,1}; q_idx];
417             elseif dominates(q,p)
418                 N(p_idx) = N(p_idx) + 1;
419             end
420         end
421         if N(p_idx) == 0
422             RANK(p_idx) = 1;
423             PF{1,1} = [PF{1,1}; p_idx];
424         end
425     end
426     i = 1;
427     while ¬isempty(PF{i,1})
428         Q = [];
429         currPF = PF{i,1};
430         for p_idx = 1:1:length(currPF)
431             Sp = S{currPF(p_idx),1};
432             for q_idx = 1:1:length(Sp)
433                 N(Sp(q_idx)) = N(Sp(q_idx))−1;
434                 if(N(Sp(q_idx)) == 0)
435                     RANK(Sp(q_idx)) = i + 1;
436                     Q = [Q; Sp(q_idx)];
437                 end
438             end
```

```
439         end
440         i = i + 1;
441         PF{i,1} = Q;
442     end
443 end
444 % Function that performs a vectorized version of the Fast Non Dominated Sorting
445 % algorithm which speeds up the computation time
446 function [RANK] = FastNonDominatedSorting_Vectorized(fitness)
447     % Initialization
448     Np = size(fitness,1);
449     RANK = zeros(Np,1);
450     current_vector = [1:1:Np]';
451     current_pf = 1;
452     all_perm = [repmat([1:1:Np]',Np',1), reshape(repmat([1:1:Np],Np,1),Np^2,1)];
453     all_perm(all_perm(:,1)==all_perm(:,2),:) = [];
454         % Computing each Pareto Front
455     while ¬isempty(current_vector)
456 
457         % Check if there is only a single particle
458         if length(current_vector) == 1
459             RANK(current_vector) = current_pf;
460             break;
461         end
462                 % Non-dominated particles
463             % Note: nchoosek has an exponential grow in computation time, so
464             % it's better to take all the combinations including repetitions using
465             % a loops (quasi-linear grow) or repmats (linear grow)
466             %all_perm = nchoosek(current_vector,2);
467             %all_perm = [all_perm; [all_perm(:,2) all_perm(:,1)]];
468         d = dominates(fitness(all_perm(:,1),:),fitness(all_perm(:,2),:));
469         dominated_particles = unique(all_perm(d==1,2));
470 
471         % Check if there is no room for more Pareto Fronts
472         if sum(¬ismember(current_vector,dominated_particles)) == 0
473             break;
474         end
475         % Update ranks and current_vector
476         non_dom_idx = ¬ismember(current_vector,dominated_particles);
477         RANK(current_vector(non_dom_idx)) = current_pf;
478         all_perm(ismember(all_perm(:,1),current_vector(non_dom_idx)),:) = [];
479         all_perm(ismember(all_perm(:,2),current_vector(non_dom_idx)),:) = [];
480         current_vector(non_dom_idx) = [];
481         current_pf = current_pf + 1;
482     end
```

```
483 end
484 % Function that returns true if x dominates y and false otherwise
485 function d = dominates(x,y)
486     d = (all(x≤y,2) & any(x<y,2));
487 end
```

Annexe B

Code MATLAB implémenté pour le traitement des signaux - Article 4

```
% ------------------------------------------------------------------------ %
% Signal processing                                                        %
% ------------------------------------------------------------------------ %
%   Author:  Bleriot Feujofack                                             %
%   Date:    18/11/2018                                                    %
%   E-mail:  f.bleriotvincent (at) yahoo (dot) fr                          %
% ------------------------------------------------------------------------ %
function [] = trait1(a)
IndirIV=':\curten\';
as=num2str(a);
current=strcat('I',as);
voltage=strcat('V',as);
A=xlsread(current);
I=A(2:end,[2]);
B=xlsread(voltage);
V=2*B(2:end,[2]);

if strcmpi(as,'5200')
    V=V(325:end);
    elseif strcmpi(as,'6400')
    V=V(17:end);
    elseif strcmpi(as,'7000')
     I=I(10:end);
     elseif strcmpi(as,'7200')
    I=I(21:end);
elseif strcmpi(as,'7400')
    V=V(38:end);
    elseif strcmpi(as,'7600')
    V=V(29:end);
    elseif strcmpi(as,'7800')
    V=V(32:end);
    elseif strcmpi(as,'8000')
```

```
    V=V(28:end);
elseif strcmpi(as,'dust')
     I=I(13:end);
     elseif  strcmpi(as,'doubling')
    V=V(27:end);
    elseif  strcmpi(as,'one-sheet')
    V=V(16:end);
end
figure (1)
set(gca,'FontSize',12)
ax1=subplot(1,2,1)
plot(I,'linewidth',1);
pbaspect(ax1,[2 1 1]);
xlabel('Time - ms','Fontsize',12);
ylabel('Current - A','Fontsize',12);
Titleri=strcat({'Raw current signal || '},as,{' '}, {'A'});
title(Titleri, 'Fontsize',14);
grid on

ax2=subplot(1,2,2)
plot(V,'r','linewidth',1);
pbaspect(ax2,[2 1 1]);
grid on
xlabel('Time - ms','Fontsize',12);
ylabel('Voltage - V','Fontsize',12);
Titlerv=strcat({'Raw voltage signal || '},as,{' '}, {'A'});
title(Titlerv, 'Fontsize',14);
movegui(figure(1),'northwest');
fig=gcf;
fig.Units='normalized';
fig.OuterPosition=[0 0 1 1];
rawIV=strcat('Data\',as,'\rawIV_',as);
IV=fullfile(IndirIV,rawIV);
print(rawIV,'-dpng','-r600');
print(rawIV,'-dmeta');
h = figure(1);
set(h,'Units','Inches');
pos = get(h,'Position');
set(h,'PaperPositionMode','Auto','PaperUnits','Inches','PaperSize',
[pos(3), pos(4)])
% print(h,'filename','-dpdf','-r0')
xlswrite(rawIV,I,1,'A1');
xlswrite(rawIV,V,1,'B1');
print(h,rawIV,'-dpdf');
```

```
77  set(findobj(gcf,'type','axes'),'FontName','Arial','FontSize',12);
78
79
80  Fsi = 10000;
81  Foi=20;
82  Cfi=1;
83  Hd = designfilt('lowpassfir','FilterOrder',Foi,'CutoffFrequency',Cfi, ...
84  'DesignMethod','window','Window',{@kaiser,3},'SampleRate',Fsi);
85  If = filter(Hd,I);
86  I=I(100:end);
87  If=If(100:end);
88  V=V(100:end);
89  n=size(If);
90  k=0;
91
92
93  for i=1:n-20
94      if abs(If(i)-If(i+10))>500
95          k=k+1;
96        b(k)=i-50;
97
98      end
99
100 end
101 deb=50;
102 I=I(b(1):end);
103 If=If(b(1):end);
104 V=V(b(1):end);
105 b=0;
106 k=0;
107 n=size(If);
108 for i=n-20:-1:50
109     if abs(If(i)-If(i-20))>1500
110         k=k+1;
111       b(k)=i+50;
112
113     end
114
115 end
116 fn=b(1)-50;
117 b(1);
118 Iloc=I(1:fn);
119 If=If(1:b(1));
120 V=V(1:b(1));
```

```
Vl=V(1:fn);

figure (2)
set(gca,'FontSize',8)
ax1=subplot(1,2,1)
plot(Iloc,'linewidth',1.2);
pbaspect(ax1,[2 1 1]);
xlabel('Time - ms','Fontsize',12);
ylabel('Current - A','Fontsize',12);
Titleri=strcat({'Localized current signal || '},as,{' '}, {'A'});
title(Titleri, 'Fontsize',14);
grid on

ax2=subplot(1,2,2)
plot(Vl,'r','linewidth',1.2);
pbaspect(ax2,[2 1 1]);
grid on
xlabel('Time - ms','Fontsize',12);
ylabel('Voltage - V','Fontsize',12);
Titlerv=strcat({'Localized voltage signal || '},as,{' '}, {'A'});
title(Titlerv, 'Fontsize',14);
movegui(figure(2),'northwest');

fig=gcf;
fig.Units='normalized';
fig.OuterPosition=[0 0 1 1];
locrawIV=strcat('Data\',as,'\locrawIV_',as);
IV=fullfile(IndirIV,locrawIV);
print(locrawIV,'-dpng','-r600');
print(locrawIV,'-dmeta');
h = figure(2);
set(h,'Units','Inches');
pos = get(h,'Position');
set(h,'PaperPositionMode','Auto','PaperUnits','Inches','PaperSize',
[pos(3), pos(4)])
% print(h,'filename','-dpdf','-r0')
xlswrite(locrawIV,Iloc,1,'A1');
xlswrite(locrawIV,Vl,1,'B1');
print(h,locrawIV,'-dpdf');
set(findobj(gcf,'type','axes'),'FontName','Arial','FontSize',12);

Fsv = 10000;
Fov=20;
Cfv=1;
```

```
Hd1 = designfilt('lowpassfir','FilterOrder',Fov,'CutoffFrequency',Cfv, ...
'DesignMethod','window','Window',{@kaiser,3},'SampleRate',Fsv);
Vf = filter(Hd1,V);

figure (3)
set(gca,'FontSize',8)
ax1=subplot(1,2,1)
plot(If,'linewidth',1.2);
pbaspect(ax1,[2 1 1]);
xlabel('Time - ms','Fontsize',12);
ylabel('Current - A','Fontsize',12);
Titleri=strcat({'Filtered current signal || '},as,{' '}, {'A'});
Lit=strcat({'Filter type - Low pass '});
Fsi=num2str(Fsi/1000);
Foi=num2str(Foi);
Cfi=num2str(Cfi);

Lis=strcat({'Sampling Frequency -  '},Fsi,{' '}, {'kHz'});
Lic=strcat({'Cutoff Frequency -  '},Cfi,{' '}, {'Hz'});
Lio=strcat({'Filter Order -  '},Foi,{' '});

title(Titleri, 'Fontsize',14);
grid on

ax2=subplot(1,2,2)
plot(Vf,'r','linewidth',1.2);
pbaspect(ax2,[2 1 1]);
grid on
xlabel('Time - ms','Fontsize',12);
ylabel('Voltage - V','Fontsize',12);
Titlerv=strcat({'Filtered voltage signal || '},as,{' '}, {'A'});

Lvt=strcat('Filter type - Low pass ');
Fsv=num2str(Fsv/1000);
Fov=num2str(Fov);
Cfv=num2str(Cfv);

Lvs=strcat('Sampling Frequency -  ',Fsv,' ', 'kHz');
Lvc=strcat('Cutoff Frequency -  ',Cfv,' ', 'Hz');
Lvo=strcat('Filter Order -  ',Fov);
title(Titlerv, 'Fontsize',14);
movegui(figure(3),'northwest');

fig=gcf;
```

```
fig.Units='normalized';
fig.OuterPosition=[0 0 1 1];
fIV=strcat('Data\',as,'\fIV_',as);
IV=fullfile(IndirIV,fIV);
print(fIV,'-dpng','-r600');
print(fIV,'-dmeta');
h = figure(3);
set(h,'Units','Inches');
pos = get(h,'Position');
set(h,'PaperPositionMode','Auto','PaperUnits','Inches','PaperSize',
[pos(3), pos(4)])
% print(h,'filename','-dpdf','-r0')
xlswrite(fIV,If,1,'A1');
xlswrite(fIV,Vf,1,'B1');
print(h,fIV,'-dpdf');
set(findobj(gcf,'type','axes'),'FontName','Arial','FontSize',12);

Istore1=If;

for i= 1: size(If)
    if If(i)<0
        If(i)=0;
    end
end

Istore=If;

x=1:size(If);
V=Vf;
for i=1:size(V)
    if V(i)<0.5
        V(i)=0;
    end
end

if strcmpi(as,'paper')
    for ii=1:2
if ii==1
    If=Istore(1:550);
    x1=x(1:550);
    [Peaks,locs]=findpeaks(If,x1);
[Peaksv,locsv]=findpeaks(V,x);

figure(16)
```

```
plot(locsv,Peaksv);

locsvi=locsv(1):1:locsv(end);
Peaksvi=pchip(locsv,Peaksv,locsvi);
Vf(locsv(1):locsv(end))=Peaksvi;

[t sl]=size(locs);
for z=1:sl
    diffdeb(z)=abs(locs(z)-55);
    difffn(z)=abs(locs(z)-445);
end

[Iddeb,Id1]=min(diffdeb);
[Idfn,Id2]=min(difffn);
    locs1=locs(Id1:Id2)
    Peaks1=Peaks(Id1:Id2);

    p=0;
    [t1 sl1]=size(locs1);

    locs1=locs1'

    [sl1 t]=size(locs1);
     Vff=ones(size(locs1));
    for i=1:sl1
        Vff(i)=Vf(locs1(i));
    end

locs1i=locs1(1):1:locs1(end);
Peaks1i=pchip(locs1,Peaks1,locs1i);
If(locs1(1):locs1(end))=Peaks1i;
If1=If;

size(If1)

elseif ii==2
    If=Istore(551:end);
    x2=x(551:end);
    [Peaks,locs]=findpeaks(If,x2)
[Peaksv,locsv]=findpeaks(V,x);

figure(16)
plot(locsv,Peaksv);

```

```
297 locsvi=locsv(1):1:locsv(end);
298 Peaksvi=pchip(locsv,Peaksv,locsvi);
299
300
301 Vf(locsv(1):locsv(end))=Peaksvi;
302
303
304 [t sl]=size(locs);
305 for z=1:sl
306     diffdeb(z)=abs(locs(z)-968);
307     difffn(z)=abs(locs(z)-1359);
308
309 end
310 [Iddeb,Id1]=min(diffdeb);
311 [Idfn,Id2]=min(difffn);
312     locs1=locs(Id1:Id2);
313     Peaks1=Peaks(Id1:Id2);
314
315 locs1=locs1'
316
317     [sl1 t]=size(locs1);
318      Vff=ones(size(locs1));
319
320     for i=1:sl1
321         Vff(i)=Vf(locs1(i));
322     end
323
324 locs1i=locs1(1):1:locs1(end);
325 Peaks1i=pchip(locs1,Peaks1,locs1i);
326 If(locs1(1)-550:locs1(end)-550)=Peaks1i;
327
328 size(If)
329 If2=If;
330
331 end
332     end
333 If1=If1';
334 If2=If2';
335 If=[If1, If2];
336 If=If';
337
338 else
339
340 [Peaks,locs]=findpeaks(If,x);
```

```
[Peaksv,locsv]=findpeaks(V,x)

figure(16)
plot(locsv,Peaksv);
del=input('Enter matrix of noisy points :\n');
[t sd]=size(del)
for i=1:sd
      Peaksv(del(i))=(Peaksv(del(i)-1)+Peaksv(del(i)+1))/2
  locsvi=locsv(1):1:locsv(end);
Peaksvi=pchip(locsv,Peaksv,locsvi);

Vf(locsv(1):locsv(end))=Peaksvi;

[t sl]=size(locs);
for z=1:sl
    diffdeb(z)=abs(locs(z)-deb);
    difffn(z)=abs(locs(z)-fn);

end
[Iddeb,Id1]=min(diffdeb);
[Idfn,Id2]=min(difffn);
    locs1=locs(Id1:Id2)
    Peaks1=Peaks(Id1:Id2);
    p=0;
    [t1 sl1]=size(locs1);
for i=2:sl1

    if locs1(i)-locs1(i-1)<60 && abs(If(locs1(i))-If(locs1(i-1)))<1500
        if i<sl1-1
        rep(p+1)=i;
        p=p+1;
    end
    end
end
rep;
[t sr]=size(rep);
for i=1:sr

    locs1(rep(i)-i+1)=[];
    Peaks1(rep(i)-i+1)=[];

end
    locs1=locs1'

```

```
385      [sl1 t]=size(locs1);
386       Vff=ones(size(locs1));
387      for i=1:sl1
388          Vff(i)=Vf(locs1(i));
389      end
390   locs1i=locs1(1):1:locs1(end);
391  Peaks1i=pchip(locs1,Peaks1,locs1i);
392  If(locs1(1):locs1(end))=Peaks1i;
393      end
394
395  figure (4)
396  set(gca,'FontSize',12)
397  ax1=subplot(1,2,1)
398  plot(If,'linewidth',1.2);
399  pbaspect(ax1,[2 1 1]);
400  xlabel('Time - ms','Fontsize',12);
401  ylabel('Current - A','Fontsize',12);
402  Titleri=strcat({'Final current signal || '},as,{' '}, {'A'});
403  title(Titleri, 'Fontsize',14);
404  grid on
405
406  ax2=subplot(1,2,2)
407  plot(Vf,'r','linewidth',1.2);
408  pbaspect(ax2,[2 1 1]);
409  grid on
410  xlabel('Time - ms','Fontsize',12);
411  ylabel('Voltage - V','Fontsize',12);
412  Titlerv=strcat({'Final voltage signal || '},as,{' '}, {'A'});
413  title(Titlerv, 'Fontsize',14);
414  movegui(figure(4),'northwest');
415
416  fig=gcf;
417  fig.Units='normalized';
418  fig.OuterPosition=[0 0 1 1];
419  finalIV=strcat('Data\',as,'\finalIV_',as);
420  % IV=fullfile(IndirIV,fIV);
421  print(finalIV,'-dpng','-r600');
422  print(finalIV,'-dmeta');
423  h = figure(4);
424  set(h,'Units','Inches');
425  pos = get(h,'Position');
426  set(h,'PaperPositionMode','Auto','PaperUnits','Inches','PaperSize',
427  [pos(3), pos(4)])
428  % print(h,'filename','-dpdf','-r0')
```

```
xlswrite(finalIV,If,1,'A1');
xlswrite(finalIV,Vf,1,'B1');
print(h,finalIV,'-dpdf');
set(findobj(gcf,'type','axes'),'FontName','Arial','FontSize',12);

R=Vf./If;

figure (5)
plot(R,'linewidth',1.2);
grid on
Range=input('Enter welding time range :\n');
% x=x(Range(1):Range(2));
R=10^(6)*R(Range(1):Range(2));
figure (6)
plot(R,'linewidth',1.2);
xlabel('Time - ms','Fontsize',8);
ylabel('Dynamic resistance - \mu\Omega','Fontsize',8);
Titlerv=strcat({'Dynamic resistance signal || '},as,{' '});
title(Titlerv, 'Fontsize',10);
grid on
dynre=strcat('Data\',as,'\dynre_',as);
print(dynre,'-dpng','-r600');
print(dynre,'-dmeta');
xlswrite(dynre,R,1,'A1');
print(dynre,'-dpdf');
set(findobj(gcf,'type','axes'),'FontName','Arial','FontSize',10);

end
```

Annexe C

Signaux de courant, tension et résistance dynamique de toutes les soudures effectuées - Article 4

C.1 Signaux de bonnes soudures

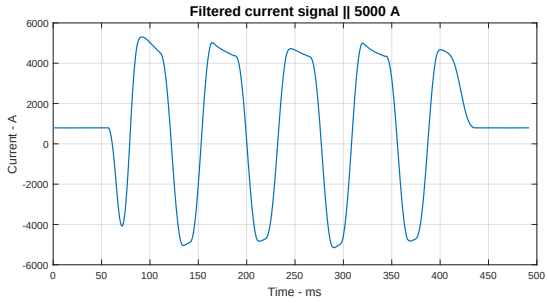

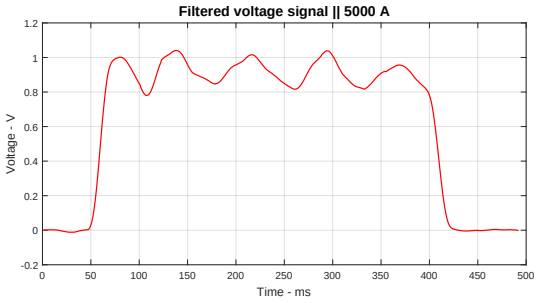

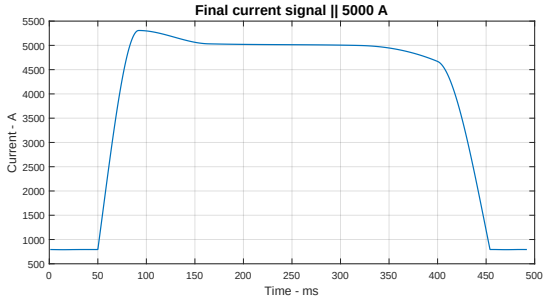

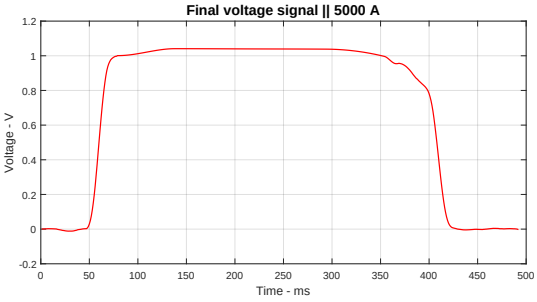

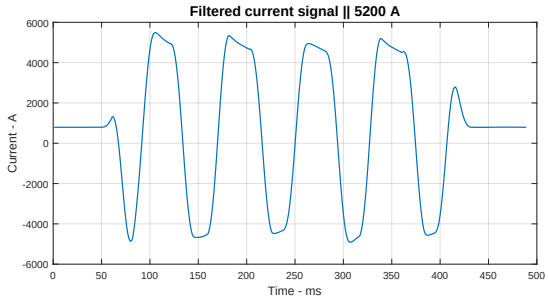
Filtered current signal || 5200 A
Current - A
Time - ms

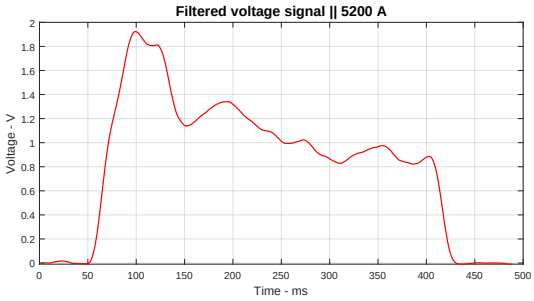
Filtered voltage signal || 5200 A
Voltage - V
Time - ms

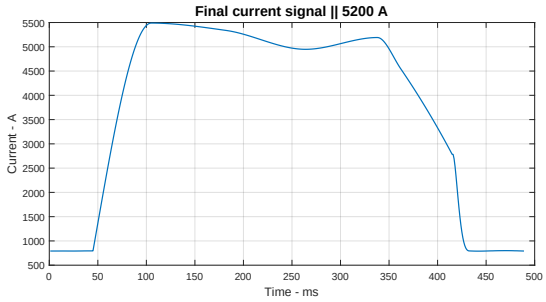
Final current signal || 5200 A
Current - A
Time - ms

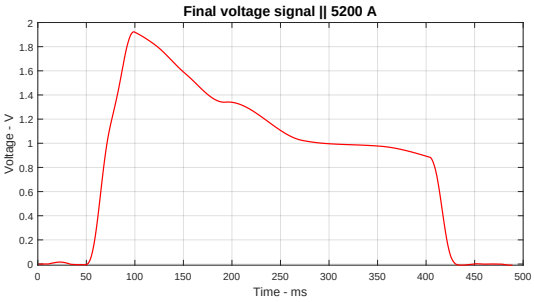
Final voltage signal || 5200 A
Voltage - V
Time - ms

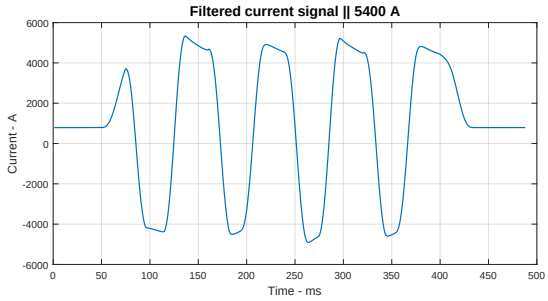
Filtered current signal || 5400 A
Current - A
Time - ms

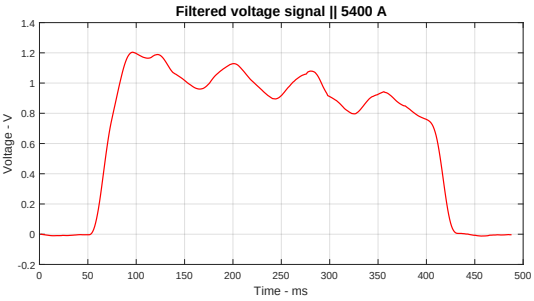
Filtered voltage signal || 5400 A
Voltage - V
Time - ms

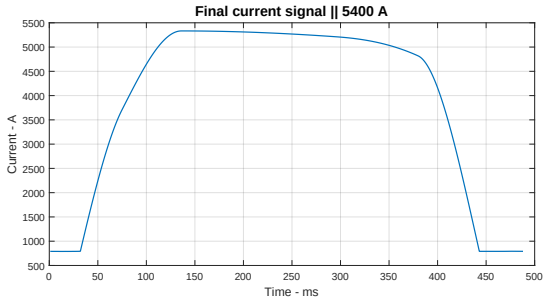
Final current signal || 5400 A
Current - A
Time - ms

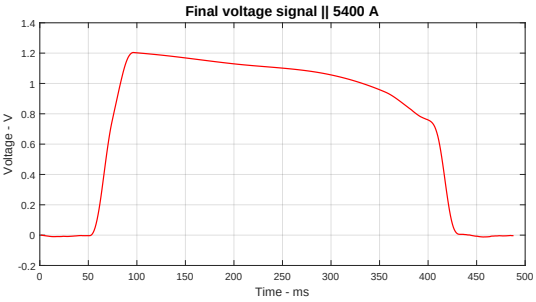
Final voltage signal || 5400 A
Voltage - V
Time - ms

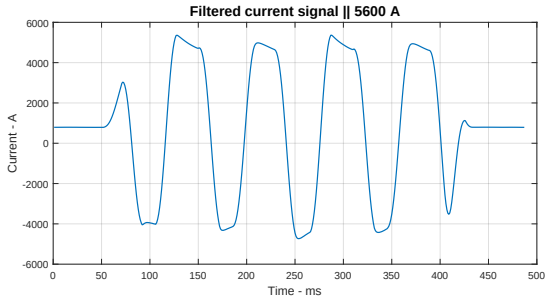
Filtered current signal || 5600 A
Current - A
Time - ms

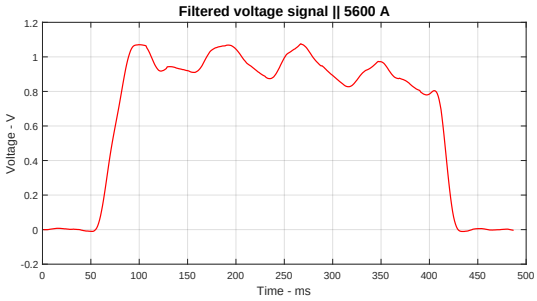
Filtered voltage signal || 5600 A
Voltage - V
Time - ms

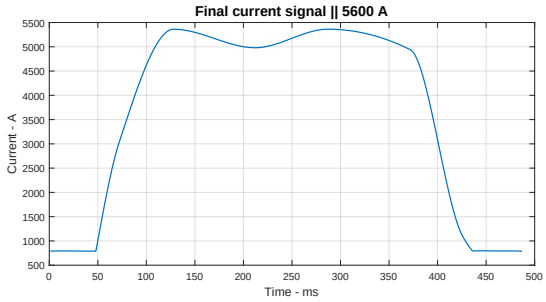
Final current signal || 5600 A
Current - A
Time - ms

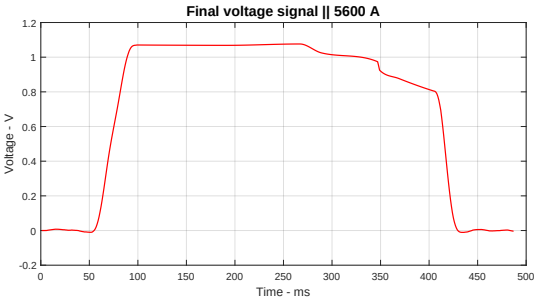
Final voltage signal || 5600 A
Voltage - V
Time - ms

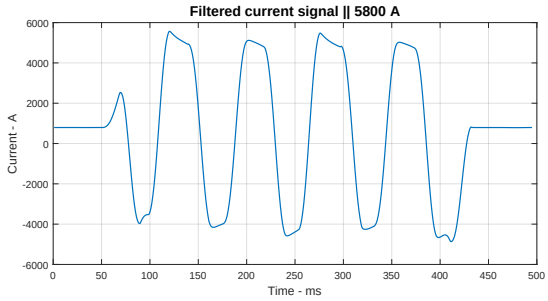
Filtered current signal || 5800 A
Current - A
Time - ms

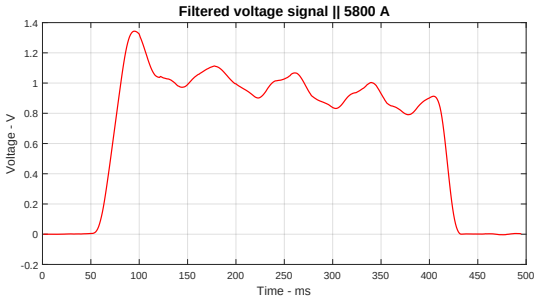
Filtered voltage signal || 5800 A
Voltage - V
Time - ms

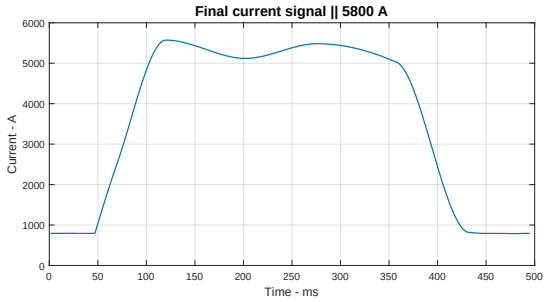
Final current signal || 5800 A
Current - A
Time - ms

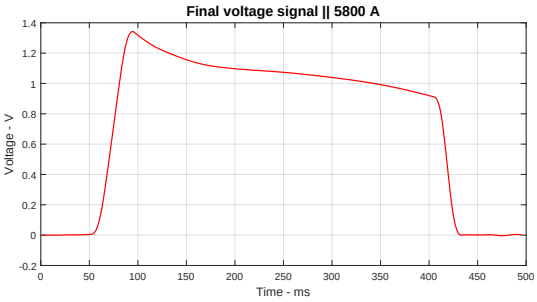
Final voltage signal || 5800 A
Voltage - V
Time - ms

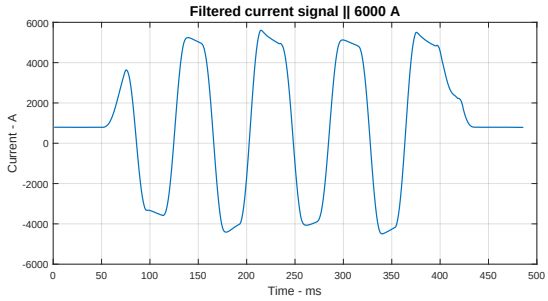
Filtered current signal || 6000 A
Current - A
Time - ms

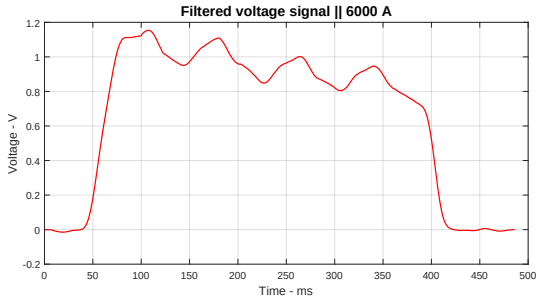
Filtered voltage signal || 6000 A
Voltage - V
Time - ms

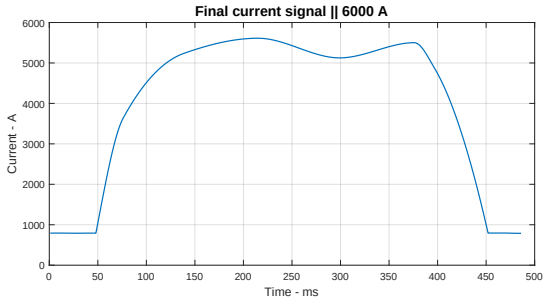
Final current signal || 6000 A
Current - A
Time - ms

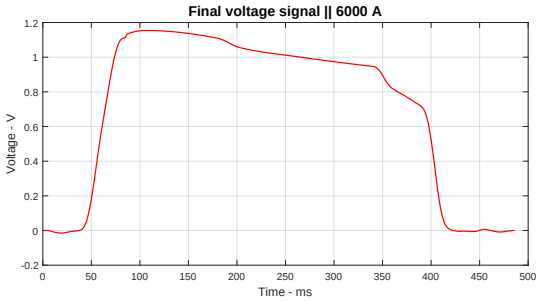
Final voltage signal || 6000 A
Voltage - V
Time - ms

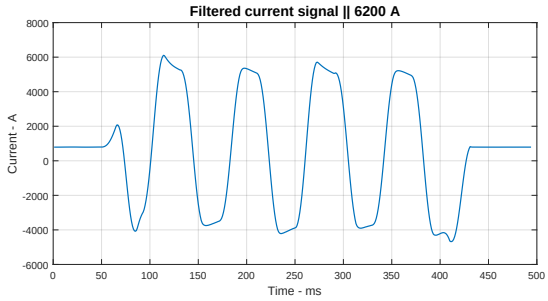
Filtered current signal || 6200 A
Current - A
Time - ms

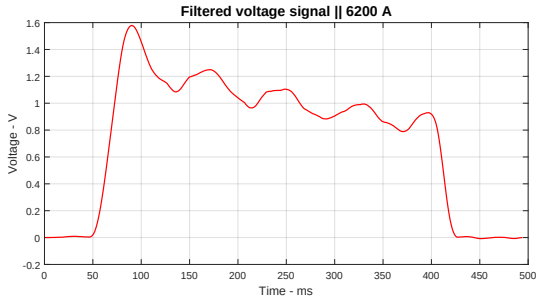
Filtered voltage signal || 6200 A
Voltage - V
Time - ms

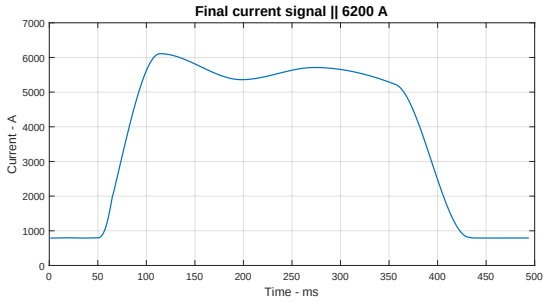
Final current signal || 6200 A
Current - A
Time - ms

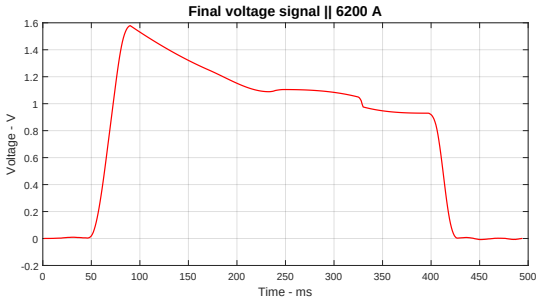
Final voltage signal || 6200 A
Voltage - V
Time - ms

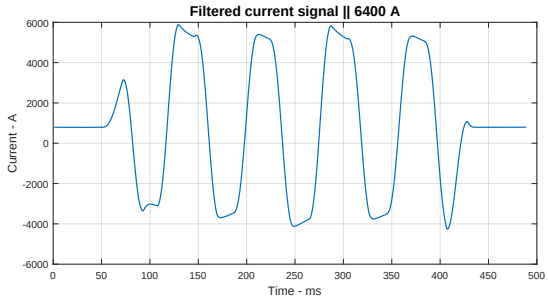
Filtered current signal || 6400 A
Current - A
Time - ms

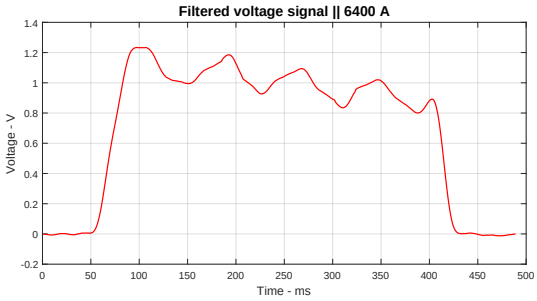
Filtered voltage signal || 6400 A
Voltage - V
Time - ms

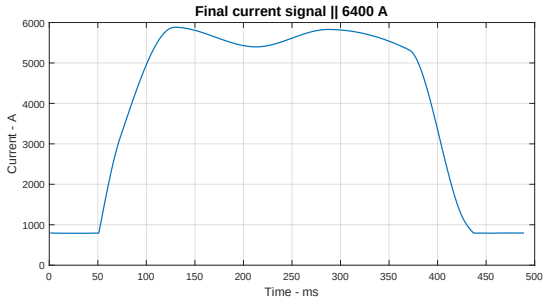
Final current signal || 6400 A
Current - A
Time - ms

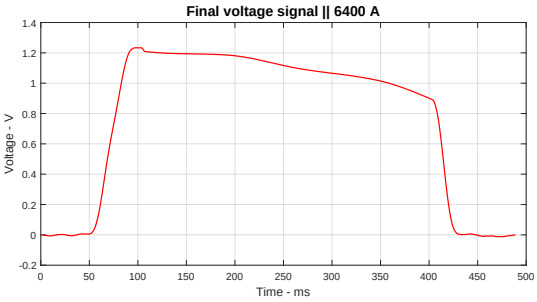
Final voltage signal || 6400 A
Voltage - V
Time - ms

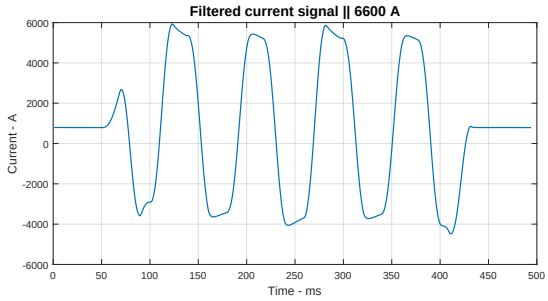
Filtered current signal || 6600 A
Current - A
Time - ms

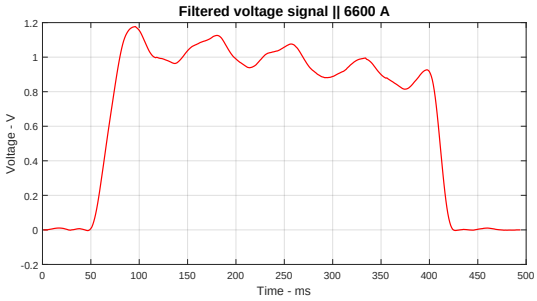
Filtered voltage signal || 6600 A
Voltage - V
Time - ms

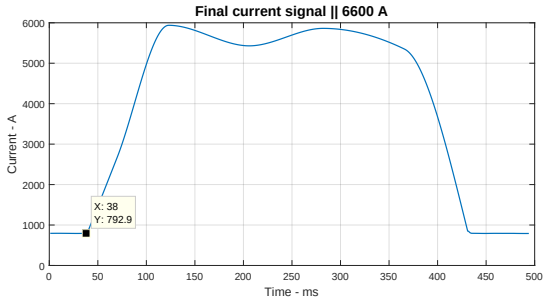
Final current signal || 6600 A
Current - A
X: 38
Y: 792.9
Time - ms

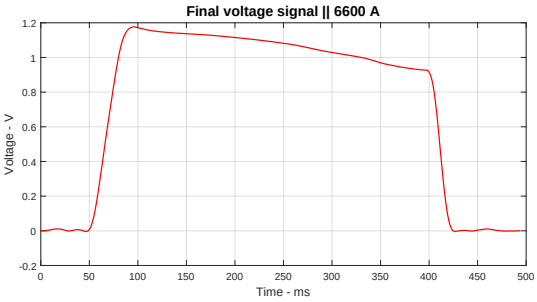
Final voltage signal || 6600 A
Voltage - V
Time - ms

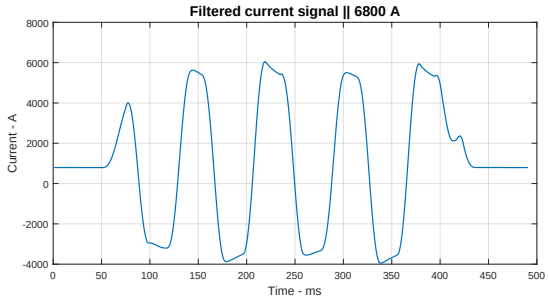
Filtered current signal || 6800 A
Current - A
Time - ms

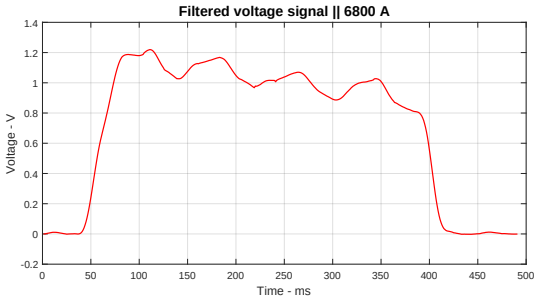
Filtered voltage signal || 6800 A
Voltage - V
Time - ms

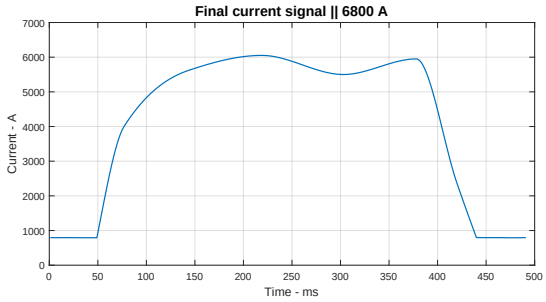
Final current signal || 6800 A
Current - A
Time - ms

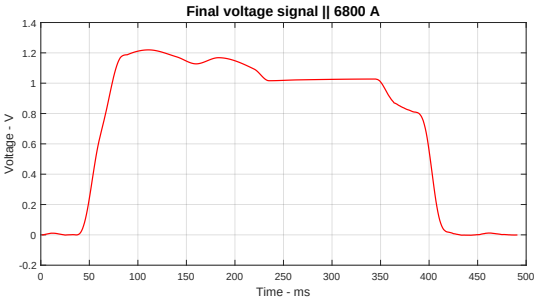
Final voltage signal || 6800 A
Voltage - V
Time - ms

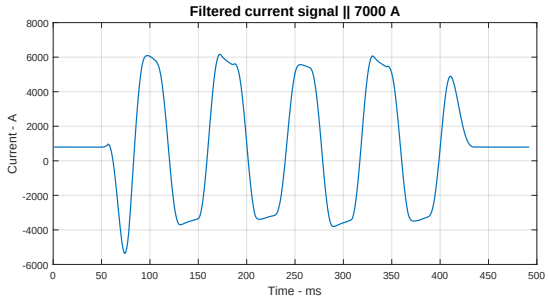
Filtered current signal || 7000 A
Current - A
Time - ms

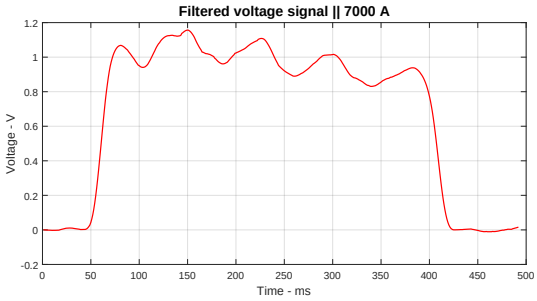
Filtered voltage signal || 7000 A
Voltage - V
Time - ms

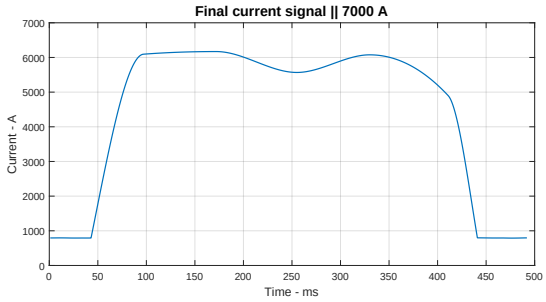
Final current signal || 7000 A
Current - A
Time - ms

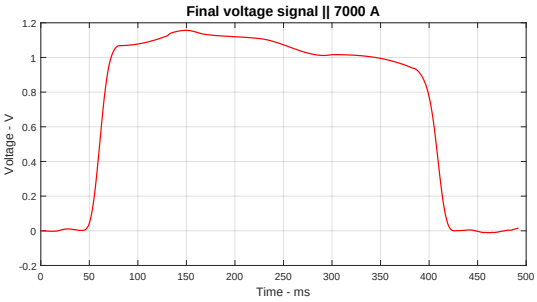
Final voltage signal || 7000 A
Voltage - V
Time - ms

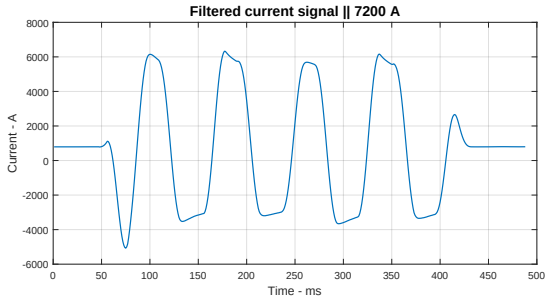
Filtered current signal || 7200 A
Current - A
Time - ms

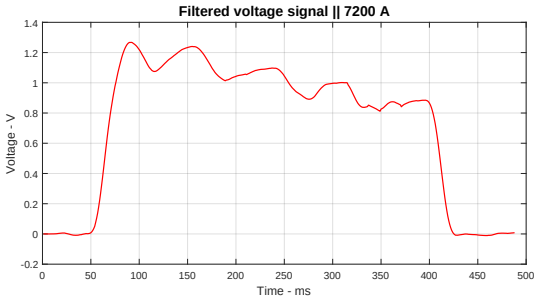
Filtered voltage signal || 7200 A
Voltage - V
Time - ms

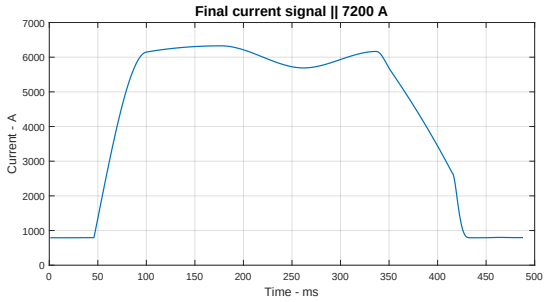
Final current signal || 7200 A
Current - A
Time - ms

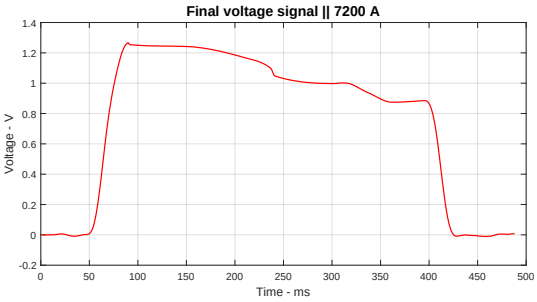
Final voltage signal || 7200 A
Voltage - V
Time - ms

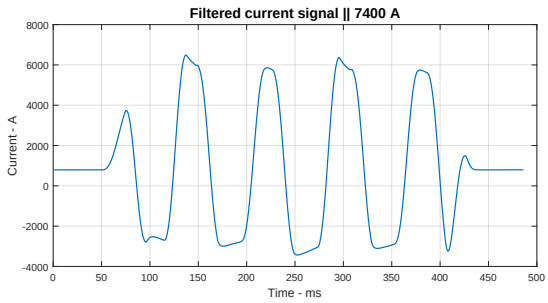
Filtered current signal || 7400 A
Current - A
Time - ms

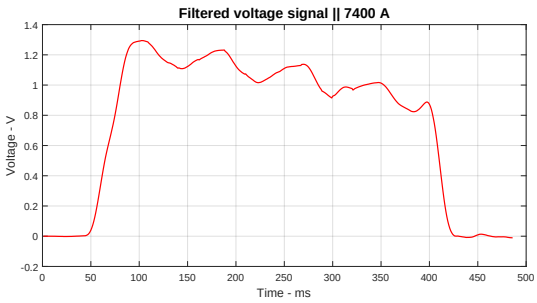
Filtered voltage signal || 7400 A
Voltage - V
Time - ms

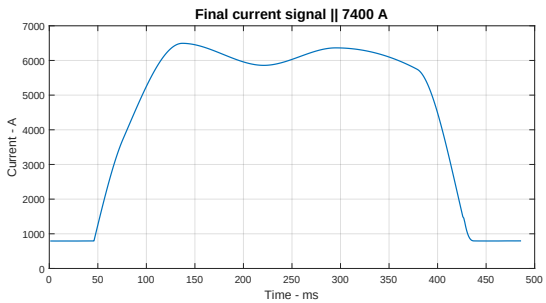
Final current signal || 7400 A
Current - A
Time - ms

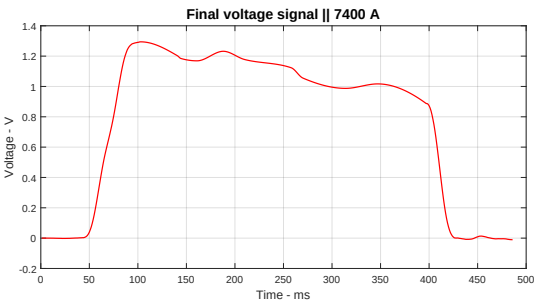
Final voltage signal || 7400 A
Voltage - V
Time - ms

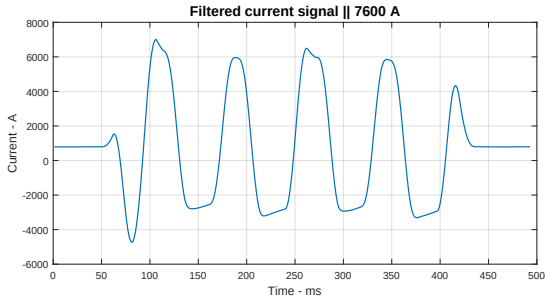
Filtered current signal || 7600 A
Current - A
Time - ms

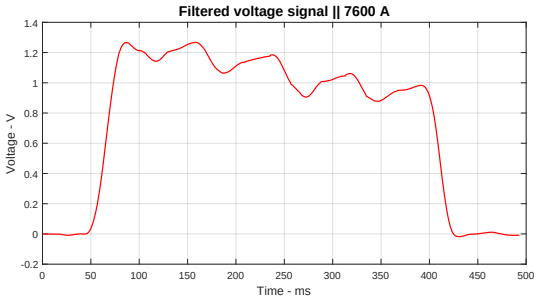
Filtered voltage signal || 7600 A
Voltage - V
Time - ms

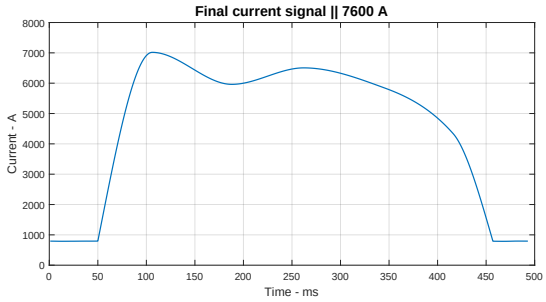
Final current signal || 7600 A
Current - A
Time - ms

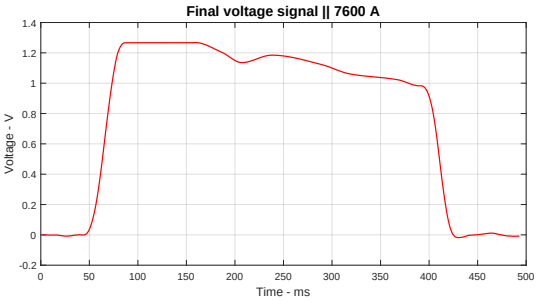
Final voltage signal || 7600 A
Voltage - V
Time - ms

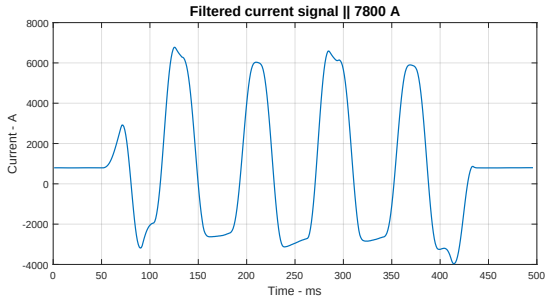
Filtered current signal || 7800 A
Current - A
Time - ms

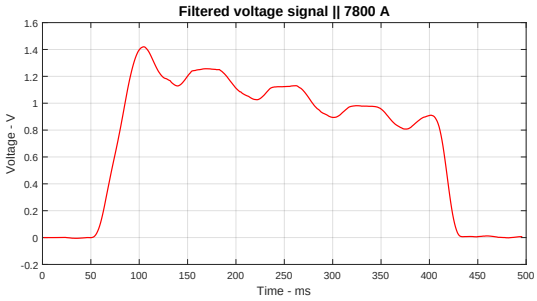
Filtered voltage signal || 7800 A
Voltage - V
Time - ms

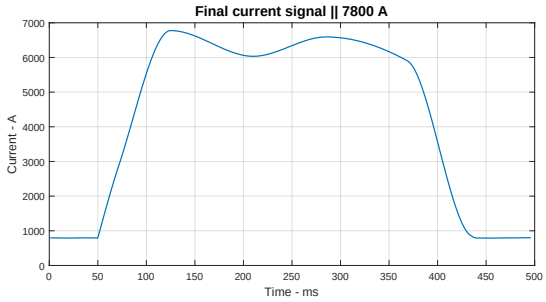
Final current signal || 7800 A
Current - A
Time - ms

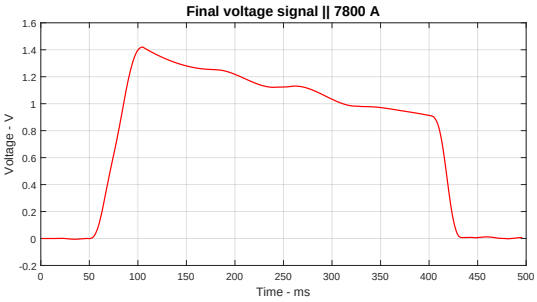
Final voltage signal || 7800 A
Voltage - V
Time - ms

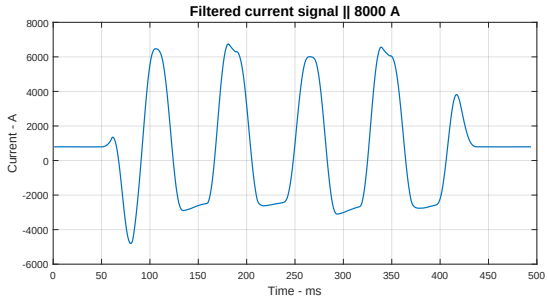

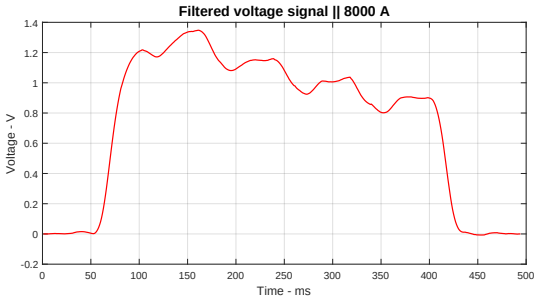

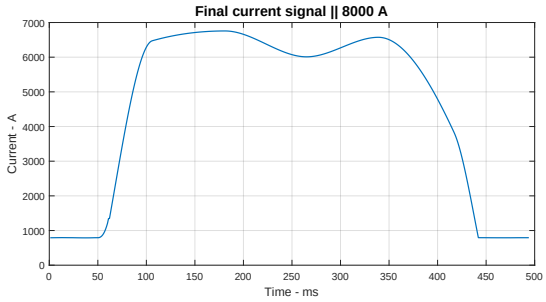

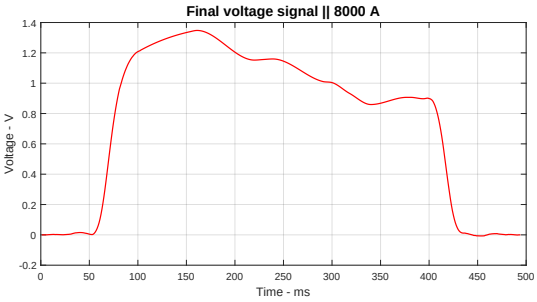

C.2 Soudures défectueuses

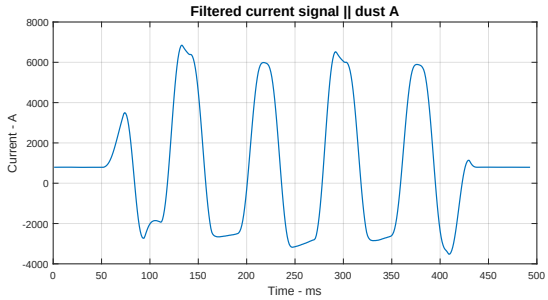

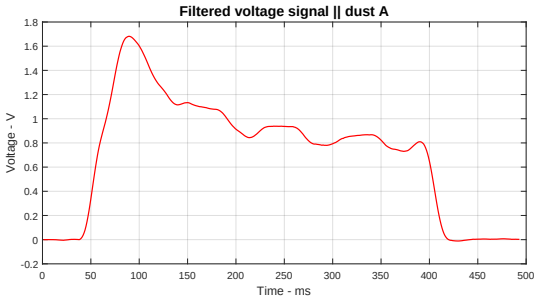

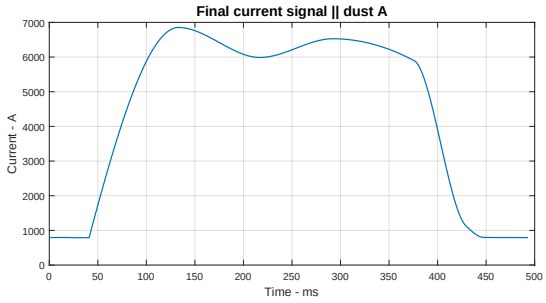
Final current signal || dust A
Current - A
Time - ms

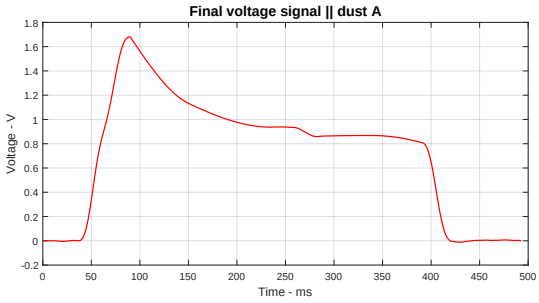
Final voltage signal || dust A
Voltage - V
Time - ms

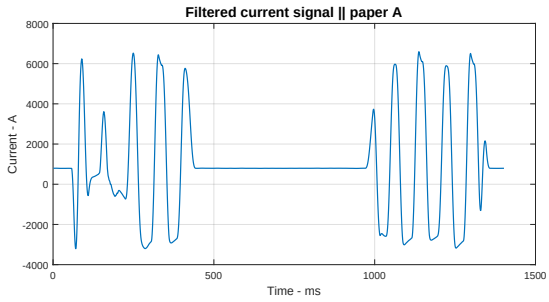
Filtered current signal || paper A
Current - A
Time - ms

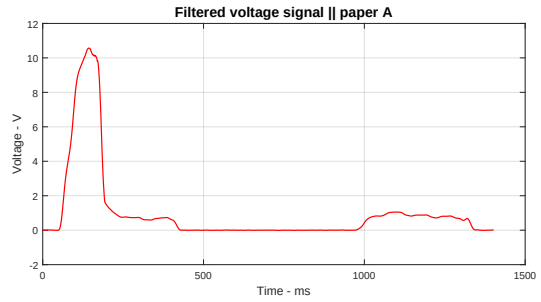
Filtered voltage signal || paper A
Voltage - V
Time - ms

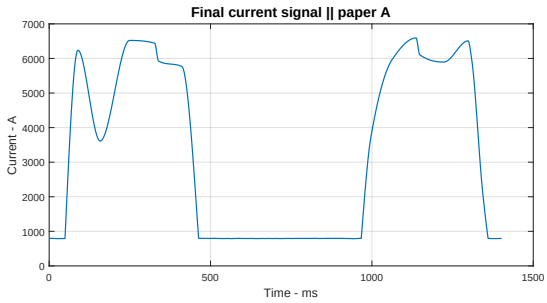
Final current signal || paper A
Current - A
Time - ms

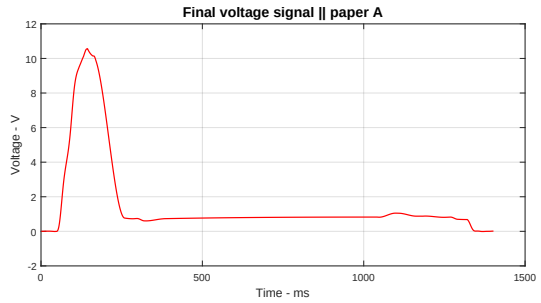
Final voltage signal || paper A
Voltage - V
Time - ms

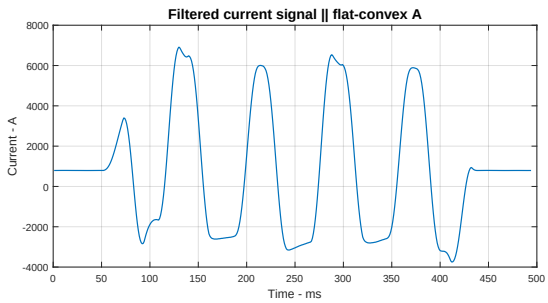
Filtered current signal || flat-convex A
Current - A
Time - ms

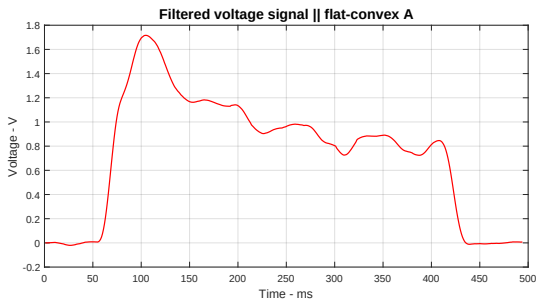
Filtered voltage signal || flat-convex A
Voltage - V
Time - ms

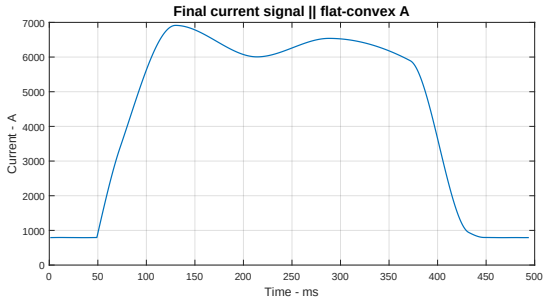
Final current signal || flat-convex A
Current - A
Time - ms

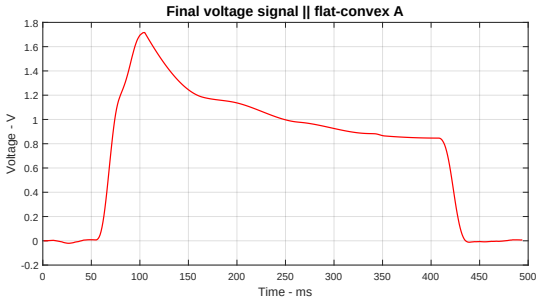
Final voltage signal || flat-convex A
Voltage - V
Time - ms

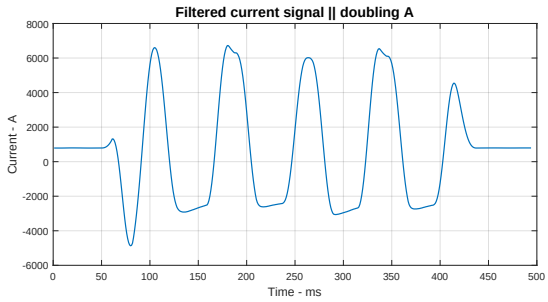
Filtered current signal || doubling A
Current - A
Time - ms

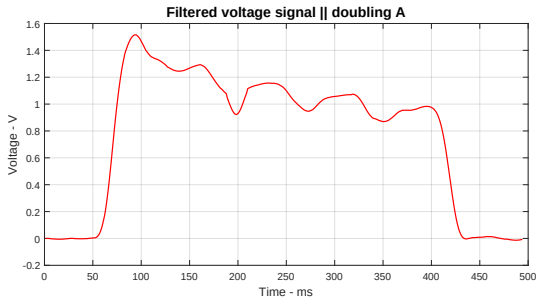
Filtered voltage signal || doubling A
Voltage - V
Time - ms

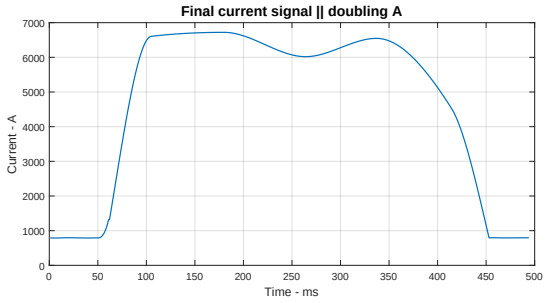
Final current signal || doubling A
Current - A
Time - ms

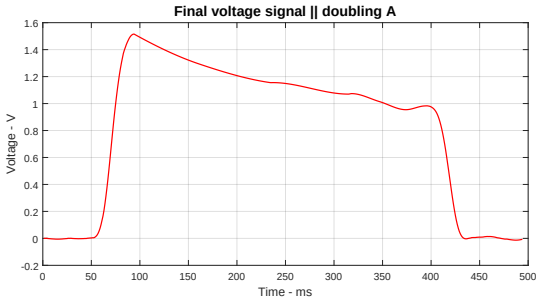
Final voltage signal || doubling A
Voltage - V
Time - ms

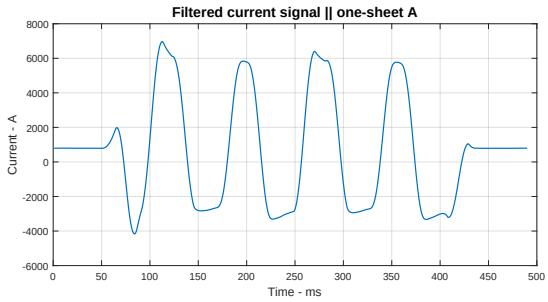
Filtered current signal || one-sheet A
Current - A
Time - ms

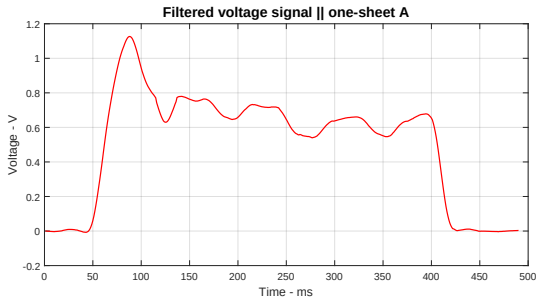
Filtered voltage signal || one-sheet A
Voltage - V
Time - ms

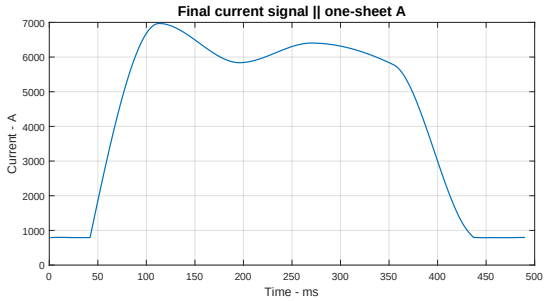
Final current signal || one-sheet A
Current - A
Time - ms

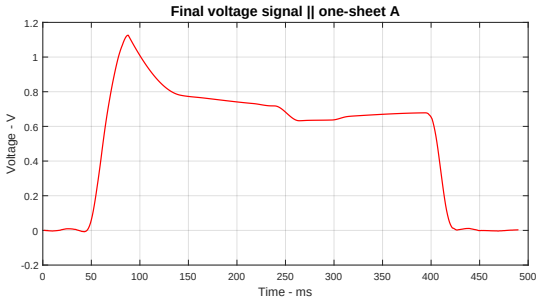
Final voltage signal || one-sheet A
Voltage - V
Time - ms

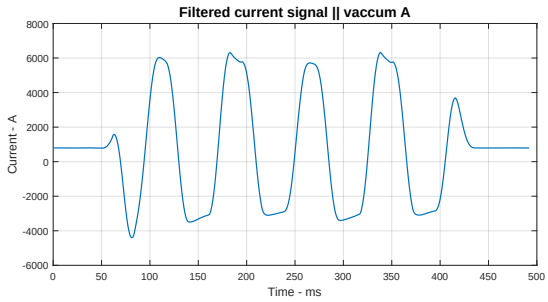
Filtered current signal || vaccum A
Current - A
Time - ms

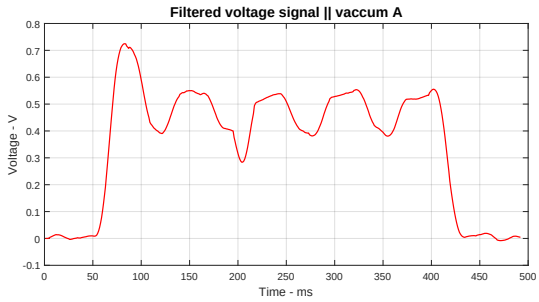
Filtered voltage signal || vaccum A
Voltage - V
Time - ms

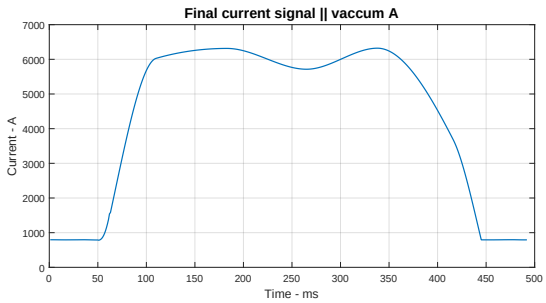
Final current signal || vaccum A
Current - A
Time - ms

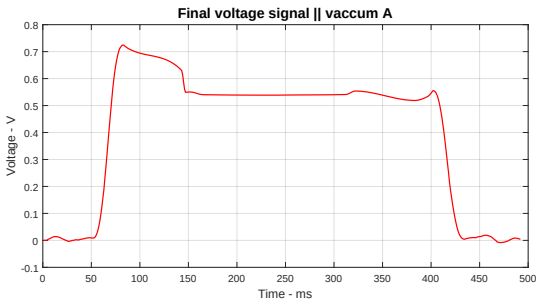
Final voltage signal || vaccum A
Voltage - V
Time - ms